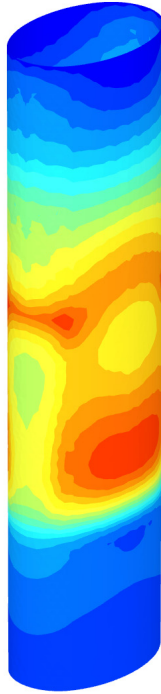**VERTICAL ELLIPTICAL ACCESS-SHAFTS**
Geometrical optimisation through
FE-modelling

ARON SANDSTRÖM and BJÖRN ELFVING

Geotechnical
Engineering

Master's Dissertation

VERTICAL ELLIPTICAL ACCESS-SHAFTS
Geometrical optimisation through
FE-modelling

ARON SANDSTRÖM and BJÖRN ELFVING

Abstract

Urbanisation is causing densification of cities and more and more facilities are being placed in the underground to utilise the urban space as efficiently as possible. Access to the underground is obtained by constructing vertical access shafts. By constructing the shaft with a circular plan geometry, an effective construction is obtained which can carry large earth pressure loads by utilising the arching effect in the construction. In this way, the walls do not need to be supported with struts and the shaft is given a free opening from above. In tunneling projects, tunnel boring machines may need to be lowered into the shaft, which requires a large radius of the circular shaft. By instead constructing the shaft with an elliptical plan geometry, the ground surface can be utilised more efficiently, while long objects can still be transported up and down from the shaft.

The purpose of this thesis is to investigate the behavior of elliptical retaining structures and to seek an optimised elliptical shape where the arching effect can be utilised as far as possible in the structure. The study is linked to a tunneling project between Lund and Malmö, where a new sewage tunnel will be built to transport wastewater from Lund to an expanded sewage treatment plant at Sjölunda in Malmö. In addition to the shape of the shaft, the foundation depth of the retaining structure is also assessed on the basis of predetermined water inflow requirements in the shaft. The study is based on drilling data from a previous project where geotechnical surveys were carried out at Sjölunda.

From the given survey data, a geo-model with known geotechnical parameters is defined. The tunnel will connect to Sjölunda at a depth of 30 m, meaning that the shaft bottom will be at a depth of 30 m. Also a requirement for a free opening of 11 m was predefined for the shaft. Groundwater related problems, such as the foundation depth of the retaining structure, are investigated in the finite element software SEEP/W. The soil-structure interaction is modelled by using the finite element software PLAXIS. A simplified method, which does not take into account the soil-structure interaction, is also used and modelled in the FE-software Robot.

With a requirement to allow a maximum groundwater inflow in the shaft of 0.5 l/s, the foundation depth of the retaining structure is determined to 10 m below the shaft bottom, i.e. 40 m below ground surface. The shape of the shaft is investigated by starting from a circular shaft that was modeled in both PLAXIS 2D and PLAXIS 3D. The models are verified by analytical calculations of the soil pressure and the corresponding horizontal normal forces from the arching effect in the structure. After verifying the model in PLAXIS 3D, a parameter study is performed in which three elliptical geometries, with increasing elongation, are investigated. For one of these geometries, a model is also built in Robot, where the load is applied as a uniformly distributed radial load corresponding to the soil pressure at different depths taken from PLAXIS. By comparing the obtained forces in the structure from both PLAXIS and Robot, it is found that PLAXIS is better at simulating the real behaviour, where the retaining structure's interaction with the ground generates lower load effects in the wall. Based on the results, PLAXIS is considered to give a more realistic result and these models are further on used to define an optimised geometry.

The resulting forces in the structure, obtained for three different geometries in PLAXIS, are compared with the capacity of a predefined cross-section of a diaphragm wall. The comparison showed that the optimum elliptical geometry, given the predetermined requirements of the shaft and the geological conditions in the area, was obtained as a relation between the short and long diameters of an ellipse of 0.45.

Sammanfattning

Urbaniseringen i samhället leder till att städerna förtätas och allt fler anläggningar förläggs till underjorden för att utnyttja den urbana ytan så effektivt som möjligt. Åtkomst till underjorden erhålls genom att konstruera vertikala åtkomstschakt. Genom att anlägga schakten med en cirkulär plangeometri erhålls en effektiv konstruktion som kan bära stora jordtrycklaster genom att utnyttja valvverkan i kontruktionen. På så sätt behöver väggarna inte stöttas upp med strävor och schaktet ges en fri öppning ovanifrån. För t.ex. tunnelprojekt kan långa tunnelborrmaskiner behöva sänkas ned i schaktet, vilket medför att det krävs en mycket stor radie hos det cirkulära schaktet. Genom att istället konstruera schaktet med en elliptisk plangeometri kan ytan utnyttjas mer effektivt, samtidigt som avlånga objekt fortfarande kan forslas upp och ned ur schaktet.

Syftet med detta examensarbete är att undersöka beteendet hos elliptiska stödkonstruktioner samt att söka finna en optimerad elliptisk form där valvverkan kan utnyttjas så långt som möjligt i konstruktionen. Undersökningen är kopplad till ett tunnelprojekt mellan Lund och Malmö där en ny avloppstunnel ska byggas för att forsla avloppsvatten från Lund till ett utbyggt avloppsreningsverk vid Sjölunda i Malmö. Utöver schaktens form kommer även stödkonstruktionens grundläggningsdjup under schaktbotten att bedömas utifrån förutbestämda krav på vatteninflöde i schaktet. Undersökningen baseras på borrdata från ett tidigare projekt där geotekniska undersökningar utförts vid Sjölunda.

Utifrån den givna undersökningsdatan kan en geomodell med kända geotekniska parametrar definieras. Tunneln ska ansluta till Sjölunda på ett djup av 30 m, vilket kräver att djupet ned till schaktbotten är 30 m. Även ett krav på en fri öppning av 11 m var fördefinierat för schaktet. Grundvattenrelaterade problem, såsom stödkonstruktionens grundläggningsdjup, undersöks i finita element programmet SEEP/W. Interaktionen mellan jord och konstruktion modelleras med hjälp av finita element programmet PLAXIS. En förenklad metod, som inte tar hänsyn till interaktionen mellan konstruktionen och jorden, används också och modelleras i finita element programmet Robot.

Med ett krav på att tillåta ett maximalt grundvatteninflöde i schaktet av 0.5 l/s kunde grundläggningsdjupet bestämmas till 10 m under schaktbotten, dvs 40 m under markytan. Schaktets form undersöks genom att utgå från ett cirkulärt schakt som modelleras både i PLAXIS 2D och PLAXIS 3D. Modellerna verifieras med handberäkningar av jordtrycket och de korresponderande horisontella normalkrafterna från valvverkan i konstruktionen. Efter att ha verifierat modellen i PLAXIS 3D utförs en parameterstudie där tre olika elliptiska geometrier, med minskande lillaxel, undersöks. För en av dessa geometrier uppförs även en modell i Robot, där lasten ansätts som en jämnt utbredd radiell last som motsvarar jordtrycket på olika djup tagna från PLAXIS. Genom att jämföra de erhållna krafterna i konstruktionen från både PLAXIS och Robot kan det konstateras att PLAXIS ger en bättre bild av verkligheten, där stödkonstruktionens interaktion med jorden genererar lägre lasteffekter i konstruktion. Utifrån resultaten anses PLAXIS ge ett mer verkligt resultat och dessa används vidare för att utreda en optimerad geometri.

De uppstådda krafterna i konstruktionen, erhållna för tre olika geometrier i PLAXIS, jämförs sedan med kapaciteten hos ett fördefinierat tvärsnitt av en slitsmur. Jämförelsen visar att den optimala elliptiska geometrin, givet de förutbestämda kraven på schaktet och de geologiska förutsättningarna i området, erhålls som ett förhållande mellan ellipsens storaxel och lillaxel till 0.45.

Preface

This master's thesis comprises 30 credits and forms the final part of our Civil Engineering degree at Lunds Tekniska Högskola. The study was performed during spring 2020 as a collaboration between Lund University and Tyréns AB in Malmö.

Malmö, May 2020
Aron Sandström and Björn Elfving

Notations and symbols

Greek letters

α	Angle of a slope
δ_{ij}	Kronecker delta
ϵ	Strain
γ	Unsaturated unit weight of the material
γ_d	Partial coefficient for safety class in design
γ_s	Saturated unit weight of the material
γ_W	Unit weight of water
$\gamma_{R,d}$	Pressure gradient factor
μ	Friction coefficient
ν	Poisson's ratio
ν'	Effective poisson's ratio
ϕ	Angle of internal friction
ϕ'	Effective angle of internal friction
$\phi(\infty, t_0)$	Creep coefficient
ϕ_x	Rotational degree of freedom (rotation in the yz-plane)
ϕ_y	Rotational degree of freedom (rotation in the xz-plane)
ϕ_z	Rotational degree of freedom (rotation in the xy-plane)
ψ	Angle of dilatancy
ρ_m	Density of saturated soil
ρ_W	Density of water
σ	Normal stress
σ'	Effective normal stress

σ_1'	Effective principal stress in the vertical direction
σ_3'	Effective principal stress in the horizontal direction
σ_H'	Effective horizontal stress
σ_0'	Effective average stress
σ_a	Longitudinal stress
σ_c	Compression stress
σ_f'	Effective normal stress associated with failure
σ_H	Horizontal stress/Lateral earth pressure
σ_r	Radial stress
σ_s	Stress in the lower reinforcement
σ_s'	Stress in the upper reinforcement
σ_t	Tension stress
σ_V	Vertical stress
σ_V'	Effective vertical stress
$\sigma_{hoop,max}$	Maximum hoop stress
σ_{hoop}	Hoop stress
σ_{ij}	Stress tensor
$\sigma_{r,max}$	Maximum radial stress
τ	Shear stress
τ_f	Shear strength
τ_{max}	Maximum shear stress
θ	Theoretical angle between the plane of failure and the principal plan
ζ	Reduction factor due to cracks

Latin letters

$|u|$	Total deformation
A	Minor diameter of an ellipse
A_s	Cross section area of lower reinforcement
A_s'	Cross section area of upper reinforcement
B	Major diameter of an ellipse
c	Cohesion

c'	Effective cohesion
d_{eq}	Equivalent thickness of a plate element
E	Young's modulus
E'	Effective young's modulus
E_s	Young's modulus of reinforcing steel
$E_{c,\infty}$	Young's modulus after long time
$E_{c,ef}$	Effective Young's modulus due to creep and shrinkage
E_{cm}	Young's modulus of concrete
E_{oed}	Oedometer modulus
EA	Axial stiffness
EI	Bending stiffness
F	Function of failure
F_c	Force in the concrete
F_N	Normal force
F_s'	Force in the upper reinforcement
f_{cm}	Compressive strength
F_{hoop}	Hoop force
f_{yk}	Tensile strength
G	Shear modulus
H	Height of a triangular soil wedge
I_1, I_2, I_3	Invariants of the stress tensor
i_{cr}	Critical upward water pressure gradient
i_{exit}	Upward water pressure gradient in the exit point
J_1, J_2, J_3	Invariants of the deviatoric stress tensor
K	Lateral earth pressure coefficient
k	Hydraulic conductivity
K_0	At-rest pressure coefficient
K_a	Coefficient of active earth pressure
K_p	Coefficient of passive earth pressure
$K_{0,NC}$	At-rest pressure coefficient for a normally consolidated soil

$K_{0,OC}$	At-rest pressure coefficient for a overconsolidated soil
M	Weight of a soil body
M_{11}	Torsion moment
M_{11}	Vertical bending moment
M_{22}	Horizontal bending moment
$M_{R,V}$	Vertical bending capacity
N	Normal force from a soil body
N_R	Normal force capacity
OCR	Overconsolidation ratio
P	Radial external pressure
p'_c	Highest experienced pressure
p'_0	Current experiencing pressure
p_0	At-rest pressure
P_a	Active total lateral earth pressure
p_a	Active lateral earth pressure
P_p	Passive total lateral earth pressure
p_p	Passive lateral earth pressure
q	Stress contribution from a surcharge
r_i	Inner radius
r_o	Outer radius
r_{inf}	radius of influence
R_{inter}	Interface strength
s_u	Undrained shear strength
s_{ij}	Deviatoric stress tensor
t	Thickness of a cylinder wall
u_W	Pore pressure
u_W	Pore water pressure
u_x	Translational degree of freedom along the x-axis
u_y	Translational degree of freedom along the y-axis
u_z	Translational degree of freedom along the z-axis

V	Shear force from a soil body
W	Line load along the wall from the weight of the soil
x	Radius of where the stress in the wall is calculated
z	Depth from the ground surface

Contents

1 Introduction

1.1 Background

A new sewage tunnel will be built between Lund and Malmö. Along the stretching of this tunnel, vertical shafts need to be constructed. Several aspects of this construction need to be analysed carefully and the problems are generally applicable on other projects as well. Space requirements on construction sites can often be a big problem in this type of projects. As cities are growing, the need for space in urban environments is increasing. This makes it more and more necessary to find alternative solutions for the infrastructure. One solution is to build more under ground. To be able to build subsurface structures in general, one needs to access the subsurface via vertical excavation shafts. As shafts often are required to be rather big, in order to transport equipment up and down, there is a collision between the need of more urban space and the need of more subsurface building. Construction of a shaft induces a risk of affecting nearby buildings, which means that careful design considerations of the retaining structure needs to be evaluated beforehand.

There are many ways to construct the retaining structure for a vertical shaft. A frequently used shape is the circular shaft. This shape enables efficient use of material due to utilisation of the arching effect in the structure, which gives almost only compression. However, in areas with limited space, the circular shape is not necessarily the optimal shape, especially in shafts for tunnelling where long pipes and tunnelling machines need to be transported down into the shaft. In these cases an elliptical shape could be more effective. An elliptical shape of the shaft could, to some extent, utilise the arching effect and simultaneously give a more effective use of ground space. This means that an optimised elliptical shape could be found where the arching effect is utilised in such extent that the stability of the structure is ensured, and at the same time the required space needed for the structure is less than for a circular shaft.

Apart from ensuring the stability of the structure, the retaining wall needs to deal with groundwater related problems as well. If the formation level of the excavation is located below the groundwater surface, there will be seepage of groundwater into the excavation. By constructing a retaining structure which is impervious to water, e.g. diaphragm wall, the retaining wall will prevent lateral water inflow. By combining the retaining walls with dewatering wells inside the excavation, the groundwater level can be lowered inside the shaft, and thereby allowing excavating in dry conditions. Proper design of the retaining walls and dewatering system will reduce the water pressure in the bottom of the excavation and thereby preventing the water pressure from exceeding the soil weight, which could lead to liquefaction and bottom uplift.

The upward inflow of groundwater can however be reduced by increasing the foundation depth of the retaining walls. This solution is often advantageous as it decreases the amount of groundwater which needs be pumped out. In many projects there are limits in how much groundwater can be pumped and the groundwater surface therefore cannot be lowered. By analysing and modelling the interaction between groundwater and excavation, the foundation depth of the retaining structure can be appropriately designed to ensure that the limits of groundwater pumping, in a specific project, are fulfilled.

1.2   Aim and objective

The aim of this master thesis is to analyse the soil-structure interaction in circular and elliptical vertical shafts. By analysing how the plan shape of the shaft affects the earth pressure and the resulting forces in the wall, this work seeks to define an estimation of how elliptical a shaft can be without requiring excessive reinforcing. The scope is not to provide a final design of the retaining structure, but to examine the interaction and give a rough estimate of the optimised ratio A/B in an elliptical shaft, see Figure 1.1.
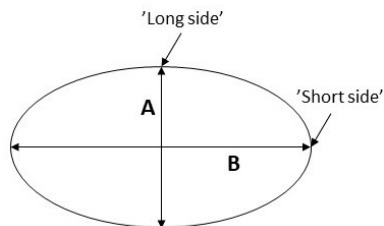
Figure 1.1: Geometry of ellipse.

Furthermore, the interaction between the structure and the groundwater is to be analysed. The aim is here to determine a suitable penetration depth of the walls below excavation bottom, but also to investigate how the penetration depth affects the groundwater situation around the shaft and the stability of the excavation bottom.

The following formulated questions are to be answered in this report:

- How does the geometry of the shaft affect the soil pressure and forces in the structure?

- Could an 'optimised' elliptical geometry be estimated through analysing the stress situation?

- How much can the elliptical shape be elongated without needing any reinforcing ring beams?

- How will the shaft affect the groundwater situation in the surroundings?

- How does the foundation depth of the retaining structure beneath the excavation bottom affect the groundwater flow into the the shaft?

1.3   Method

The report starts with a literature study. This study seeks to find valuable information on the soil mechanics involved and what techniques could be used to construct shafts with special shapes.

The soil-structure interaction is analysed in a design example using the commercial FE-software PLAXIS (Bentley Systems 2020). Geotechnical data for the design example is evaluated from a recent tunnelling project in Malmö. The study starts out from a circular shaft which can be modelled in both PLAXIS 2D and PLAXIS 3D. The results will be compared to both analytical calculations and simplified numerical calculations, where the numerical calculations are made in another FE-software called Robot (Autodesk 2020). If the results are conforming, the analysis will proceed by gradually elongating the shaft into a more elliptical shape. Through a parameter

study on the geometry, conclusions are hoped to be found on how the shape affects the interaction between soil and structure.

Groundwater-related problems, such as inflow of water into the shaft and groundwater-lowering, is modelled and analysed in the FE-software SEEP/W (GEOSLOPE 2020).

1.4   Limitations

Limitations of this thesis has been set due to constraints of time and to increase the focus on the main objectives.

- The study will not consider the effect of tunnel openings in the shaft.

- Only the completed shaft is studied, not different construction stages.

- The shapes of the shafts are assumed to be perfectly elliptical and circular.

- The study is based on the situation after long time.

- Second-order effects regarding the loading effects on the structure are not taken into account.

- The load distribution around the shaft is assumed to only vary with the depth of the shaft, surcharge is not considered.

- Only one representative geo-model for the southern part of Skåne is to be used.

2 Soil mechanics background

Soils are the supporting material for every structure located on land. As an engineer it is very important to be able to understand the interaction between soils and structures. Soil is a complex material and its behavior is influenced by many different factors. This chapter seeks to enlighten the mechanic behavior of soils and describe some affecting factors.

2.1 Drained and undrained conditions

Soils consist of grains in different sizes packed upon each other. The shape of the grains creates voids in the soil structure between the grains, so called pore space. The pore space can be filled with water if the soil is located under the groundwater level or by capillary rise of water. When soils are subjected to an external load, the pressure on the pore space increases. The water in the pore space with increased pressure will leave the pore spaces relatively quickly if the voids are connected to each other, and thereby flow to voids with lower pressure. This process is called drainage (Verruijt 2018). How fast a soil is drained correlates with the permeability of the soil. For coarse-grained soils such as gravels and sands, with high permeability, fast drainage is possible. The loading condition for these types of soils are thereby considered drained even when the load is applied over a short period of time.

If the pore spaces in the soil are sealed of from each other, the draining takes place over a very long time. This is the case for cohesive soils which are fine-grained soils such as clay and silts with low permeability. If the condition is considered to be drained or undrained in cohesive soils depends on the load-time ratio. If the cohesive soil is subjected to an external load over a short period of time and the drainage of the pore water is not complete, the condition is considered undrained (Verruijt 2018). If the load instead is applied over a long period of time and the drainage of the pore water is complete, the condition is considered drained even for cohesive soils.

The condition being drained or undrained affects how the load is carried by the soil. The drained and undrained shear strength of the soil is discussed further in Section 2.3.

2.2 Stress history

When a saturated soil is exposed to a load, the pressure is initially carried by the pore water with higher stiffness than the soil skeleton and only small deformations takes place. If the load is retained during a long period of time, drainage of the pore water occurs and the pressure is instead carried by the soil skeleton. This pressure is referred to as the effective pressure. Due to the lower stiffness of the soil, the deformations increase as the volume of the soil decreases because of compression of the pore space. This process is called consolidation of the soil and is common for cohesive soils. When the soil is unloaded, the majority of the volume decrease will remain and if the soil is reloaded by a load with lower magnitude, only small deformations will take place.

A soil currently subjected to the highest pressure ever experienced, is considered to be 'normally consolidated'. If the pressure decreases from the highest experienced pressure, the soil is considered 'overconsolidated'. The ratio between the highest experienced pressure and the current pressure is called 'overconsolidation ratio', shortened with OCR, this ratio is calculated according to (Barnes 2000)

$$OCR = \frac{p'_c}{p'_0} \tag{2.1}$$

where:

p'_c = highest experienced pressure   [kPa]
p'_0 = currently experienced pressure   [kPa]

The stress history of a soil is important to evaluate to be able to predict the behaviour of the soil. The OCR e.g., affects the horizontal in-situ stresses in the soil. Erosion is a common factor causing overconsolidation. Erosion of superimposed soil layers lowers the pressure carried by the soil skeleton and increase the overconsolidation ratio (Barnes 2000).

2.3   Shear strength

The definition for failure of soils differs from the typical mechanical failure. Failure of soils is defined to appear when the shear stress exceeds the shear strength of the material. When this occurs, large shear deformations takes place in the soil and the soil mass will slide over the soil below it (Verruijt 2018). The shear strength of a material specifies the load bearing capacity and is therefore of great importance to determine in the field of geotechnical engineering. The shear strength of a soil is dependent on the interaction between the particles, the shear strength of a single particle has less influence. Failure can occur at every contact surface between particles.

The shear strength of soils depends on the condition being drained or undrained. The stiffness of pore water is much larger then the stiffness of the soil skeleton, this means that for the undrained condition, the shear strength is constant for the material. For the drained condition, the shear strength is dependent on effective normal stress (Verruijt 2018).
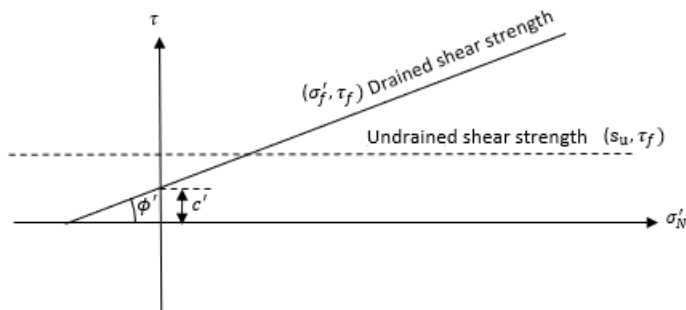
Figure 2.1: Drained and undrained shear strength.

2.3.1   Drained shear strength

When the condition is undrained and the shear stress is too large compared to the normal stress acting on a certain plane, the soil will slide and fail. This can better be understood by studying a rigid body placed on a slope. The rigid body symbolises the soil mass that can slide and the slope symbolises the soil underneath, see Figure 2.2.
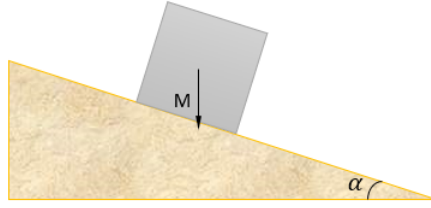
Figure 2.2: Rigid body on a slope.

The force from the weight of the body, M, is transformed to a normal force, N, and a shear force, V, acting on the slope by using the angle of the slope, α.
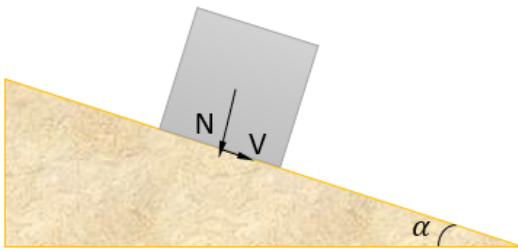
$$N = M \cos \alpha \tag{2.2}$$

$$V = M \sin \alpha \tag{2.3}$$

$$\frac{V}{N} = \frac{\sin \alpha}{\cos \alpha} = \tan \alpha \tag{2.4}$$

$$V = N \tan \alpha \tag{2.5}$$

Figure 2.3: Forces from a soil body acting on the slope underneath.

The force that keeps the body from sliding is the friction and when the ratio of shear force to normal force, $\tan \alpha$, gets greater than the friction coefficient μ, the body starts to slide down the slope due to disequilibrium of forces. The angle of the slope is decisive if equilibrium of forces can be reached or not. The friction force f is expressed as

$$f = \mu N \tag{2.6}$$

The force equilibrium along the slope is then

$$\mu N = N \tan \alpha \tag{2.7}$$

This analogy can be used with stresses as well as forces, the forces can be assumed to be evenly distributed over the entire contact surface. Equation (2.5) is rewritten

$$\tau = \sigma \tan \alpha \tag{2.8}$$

describing the relation between the shear stress τ and normal stress σ.

When the shear stress exceeds the shear strength, failure occurs and the soil slides along a plane with an angle to the horizontal plane coinciding with the angle of friction ϕ for the material. The angle of friction can therefore be used in Equation (2.8) to express the shear strength of the material, i.e.

$$\tau = \sigma \tan \phi \tag{2.9}$$

This is a simplification of how the shear resistance in reality works for soils. For none-cohesive soils, the shear resistance occurs by friction between the grains developed when the grains slide or roll over each other. For cohesive soils, the molecular attractions plays a bigger role which contributes with some shear resistance independent of the normal stress. The shear resistance contribution from the molecular attraction is called the cohesion (Verruijt 2018).

There are different mathematical methods that can be used to model the failure state of soils. The most used and widely accepted failure criterion is the Mohr-Coulomb (MC) shear strength criterion. This criterion is treated as a kind of standard due to the fact that there are several well established experimental methods to determine its parameters, angle of friction ϕ and cohesion c, and its estimations fits well to experimental measurements.

2.3.2 Mohr-Coulomb's yield criterion

Mohr-Coulomb's failure criterion describes a linear relationship between the principal stress space and the failure of an isotropic material. According to the model, the stress-strain behaviour is linear until failure, then perfectly plastic deformations occur and the stress level can not increase further, illustrated in Figure 2.4.
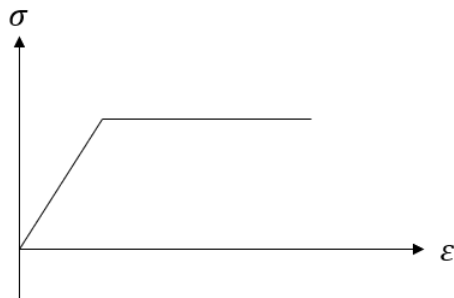
Figure 2.4: Stress-strain curve.

Mohr-Coulomb's failure equation is a function of the major and minor principal stresses. The failure criterion is a combination of Mohr's stress circle and Coulomb's failure criterion.

In 1776, Coulomb used the analogy with a sliding body, explained in Section 2.3, and proposed a criterion for failure of soils (Verruijt 2018). Coulomb's failure criterion

$$|\tau_f| = c' + \sigma' \tan \phi' \tag{2.10}$$

defines failure on a plane as a function of the critical combination of shear stress τ_f and effective normal stress σ'. The relationship between the critical shear stress and normal stress is related to drained loading conditions and is dependent on the two material constants, c' (effective cohesion) and ϕ' (effective angle of internal friction) (Augarde 2012). The effective cohesion contributes with some shear resistance even when the normal stress is zero.

For undrained loading, the normal stress does not affect the shear strength, only the water content matters. For this case, the Mohr-Coulomb yield criterion is reduced to Tresca's criterion

$$|\tau_f| = s_u \tag{2.11}$$

where:

s_u = undrained shear strength, further discussed in Section 2.3.3

Mohr's stress circle is a two-dimensional graphical representation of the stress state at a particular material point. Compression stress is often defined as positive in soil mechanics. It can be used to determine the magnitude of the shear stress and normal stress on an arbitrary plane in the material by transforming the principal stresses. If the orientation and magnitude of the shear stress and normal stress is known, the Mohr's stress circle can be constructed. Figure 2.5(a) shows the shear and normal stress with known orientation for a particular material point and Figure 2.5(b) represents the corresponding Mohr's circle.

((a)) Stress state.   ((b)) Mohr's stress circle.
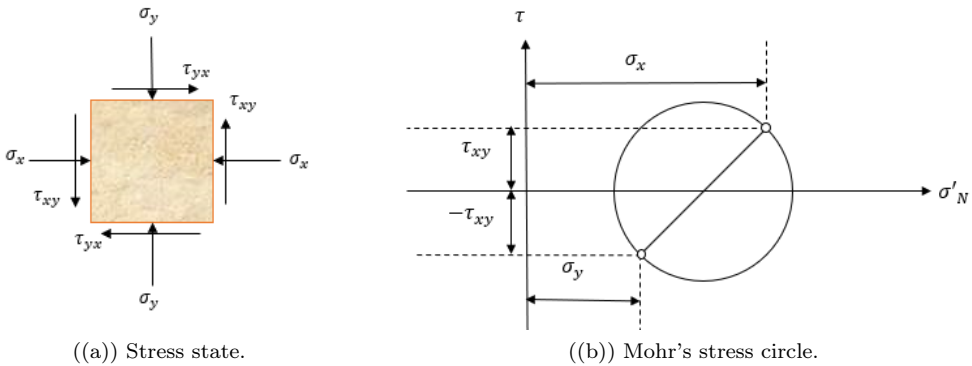
Figure 2.5: Construction of Mohr's stress circle.

By inserting Coulomb's failure criterion, Equation (2.10), into Mohr's diagram, the combination of shear and normal stress associated with failure is defined by a yield line. When Mohr's stress circle tangents the yield line the principal stress state related to failure is found. The major (σ_1') and minor (σ_3') principal stresses are found at the intersection of the circle and the normal stress-axis (Labuz and Zang 2012), see Figure 2.6.
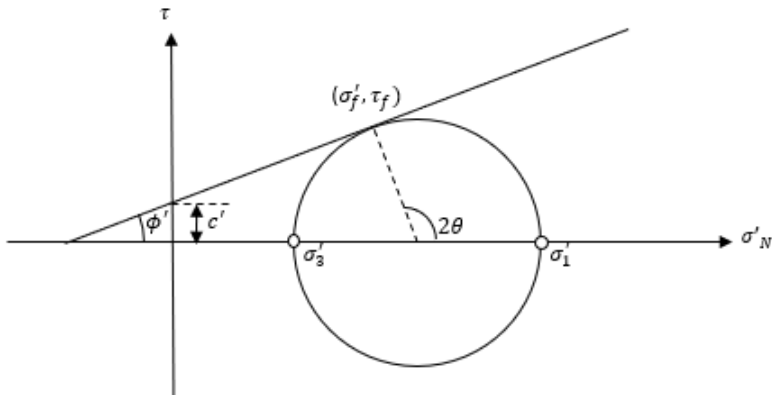
Figure 2.6: Mohr-Coulomb failure criterion.

For a particular material point with known principal stresses, the shear stress, τ_f, and effective normal stress, σ'_f, located where the circle tangents the yield line can be found by using Mohr's transformation formula (Craig and Knappett 2012)
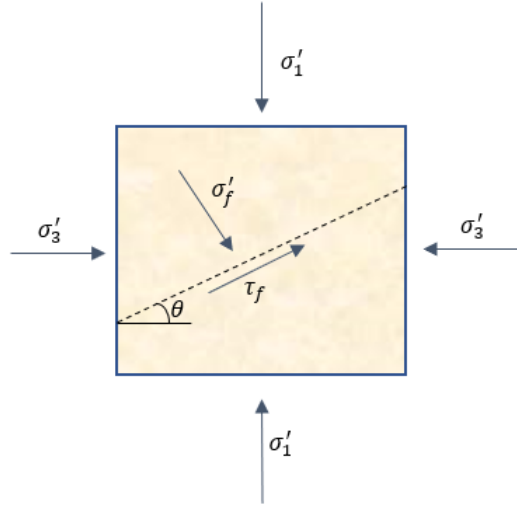
Figure 2.7: Failure for a triaxial compression test.

$$\tau_f = \frac{1}{2}(\sigma'_1 - \sigma'_3)\sin 2\theta \qquad (2.12)$$

$$\sigma'_f = \frac{1}{2}(\sigma'_1 + \sigma'_3) + \frac{1}{2}(\sigma'_1 - \sigma'_3)\cos 2\theta \qquad (2.13)$$

where:
θ = theoretical angle between the plane of failure and the principal plan

The failure angle, θ, can be expressed as

$$\theta = 45° + \frac{\phi'}{2} \qquad (2.14)$$

with the effective angle of internal friction. Figure 2.7 shows failure for a triaxial compression test.

2.3.3 Undrained shear strength

When the condition is considered undrained, the shear strength behaviour of the soil differs in comparison with the shear strength at drained condition. The undrained shear strength, s_u, can be determined as the radius of Mohr's circle as (Verruijt 2018)

$$s_u = \frac{\sigma_1 - \sigma_3}{2} \qquad (2.15)$$

The undrained shear strength can also be estimated from the basic drained parameters, the cohesion c and the angle of friction ϕ. The expression for s_u can be derived by assuming that the volume practically remains constant after loading when the soil is saturated. This causes the isotropic effective stress of the soil to remain unchanged and constraining the location of the stress circle in Mohr's diagram. When the effective vertical stress, σ'_V, and the effective horizontal stress, σ'_H, are known in the soil, the derivation can be carried out. The average effective stress, σ'_0, is constant and expressed as

$$\sigma'_0 = \frac{1}{3}(\sigma'_V + 2\sigma'_H) = constant \tag{2.16}$$

based on the assumption that the two effective horizontal stresses are of equal magnitude. The Mohr-Coulomb failure criterion can be expressed with the major σ'_1 and minor σ'_3 principal stresses as

$$\left(\frac{\sigma'_1 - \sigma'_3}{2}\right) - \left(\frac{\sigma'_1 + \sigma'_3}{2}\right)\sin\phi - c\cos\phi = 0 \tag{2.17}$$

This equation can be expressed with the average effective stress by using the extension of the expression

$$\sigma'_1 + \sigma'_3 = \frac{2}{3}(\sigma'_1 + 2\sigma'_3) + \frac{1}{3}(\sigma'_1 - \sigma'_3) \tag{2.18}$$

By inserting Equation (2.18) into Equation (2.17) the expression

$$(1 - \frac{1}{3}\sin\phi)\left(\frac{\sigma'_1 - \sigma'_3}{2}\right) - \left(\frac{\sigma'_1 + 2\sigma'_3}{3}\right)\sin\phi - c\cos\phi = 0 \tag{2.19}$$

is obtained. If the horizontal and vertical stresses coincides with the principal stresses, Equation (2.16) can be identified in the equation above and is inserted. The failure criterion is now expressed with the average effective stress which is equal to the given average effective stress σ'_0 i.e

$$s_u = \frac{\sigma'_1 - \sigma'_3}{2} = c\frac{\cos\phi}{1 - \frac{1}{3}\sin\phi} + \sigma'_0\frac{\sin\phi}{1 - \frac{1}{3}\sin\phi} \tag{2.20}$$

For pure cohesive soils, $\phi = 0$, and Equation (2.20) thereby reduces to $s_u = c$ as expected. For friction soils, $\phi > 0$, the shear strength according to Equation (2.20) increases with the average effective stress state σ'_0.

It is important to notice that this is just an approximation of the undrained shear strength. The assumption that the volume of the soil is unchanged after loading means that the effects of anisotropy, dilatancy and contractancy have been neglected (Verruijt 2018).

2.4 Stresses in soil

Estimations of the stresses in soils are of interest when dealing with geotechnical engineering problems. The weight of the material above a certain level in the ground acts as a load on the soil underneath, the stress level consequently increases with depth. The principal stresses at a horizontally oriented surface in the ground are of great importance to determine. The principal stresses consist of a vertical stress, which often is the greatest, and two horizontal stresses that often are of equal magnitude, see Figure 2.8. The effective stresses are the stresses carried by

the soil skeleton and are usually used in stress analyses. This is the case when calculating the in-situ stresses which are the stresses in an unloaded soil at its original position (Terzaghi 1944).
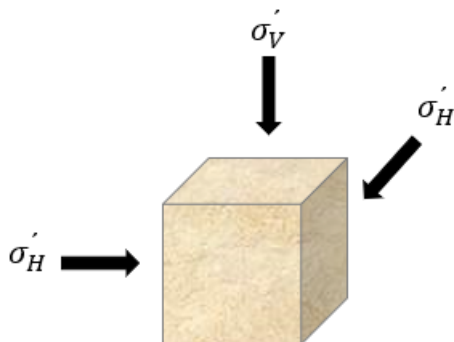
Figure 2.8: Principal stresses on an arbitrary material point.

2.4.1 Vertical stress

For a soil profile with constant unit weight along the depth, the vertical stress, σ_V, is a function of the depth in the ground and is given by the relationship

$$\sigma_V(z) = \gamma z \tag{2.21}$$

where:

$\gamma =$ unsaturated unit weight of the material $\quad [\text{kN/m}^3]$
$z =$ depth from the ground surface $\quad [\text{m}]$

If water is present in the soil, the soil is saturated and the saturated unit weight of the soil γ_s is instead used to calculate the vertical stress.

When the soil is subjected to an external load at the ground surface, called surcharge, from e.g. buildings or machines, the vertical stress in the soil increases. When the surcharge is extensively wide, the distribution of the stress in the horizontal plane can be neglected and the stress increase q is constant with the depth.

The vertical stress including the surcharge is called the total vertical stress i.e.

$$\sigma_V(z) = \gamma z + q \tag{2.22}$$
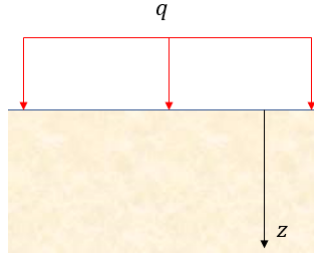
Figure 2.9: Surcharge on soil.

In reality, the unit weight of a soil profile often varies with the depth. The general equation

$$\sigma_V(z) = \sum_{i=1}^{n} \gamma_i z_i + q \tag{2.23}$$

where:

n = total number of layers

γ_i = unit weight of each layer $\quad$ [kN/m^3]

z_i = depth of each layer $\quad$ [m]

considers the variation of the unit weight in the soil profile. When the soil is located under the ground water level, the water in the soil will cause a pressure in the pore space, so called pore pressure u_W, calculated as

$$u_W(z) = \gamma_W z \tag{2.24}$$

where:

γ_W = unit weight of water $\quad$ [kN/m^3]

z = depth from the water surface in the soil $\quad$ [m]

and according to Archimede's Principle give rise to an upward buoyant force on the material in the soil (Barnes 2000). In finer soils, such as clays and silts, the water may rise above the groundwater level due to the effect of capillarity. When water is present in the pores above the groundwater level, z is negative and defines the distance from the groundwater level. According to Terzaghi (1944), the total vertical stress is the sum of the the effective vertical stress σ_V' and the pore pressure defined as

$$\sigma_V(z) = \sigma_V' + u_W(z) \tag{2.25}$$

Equation (2.25) is referred to as Terzaghi's principle and is used to express the effective vertical stress as a function of the depth in the ground

$$\sigma_V'(z) = \sigma_V(z) - u_W(z) \tag{2.26}$$

Figure 2.10 shows the effective vertical stress variation along the depth of the soil for a homogeneous soil with no capillary rise.
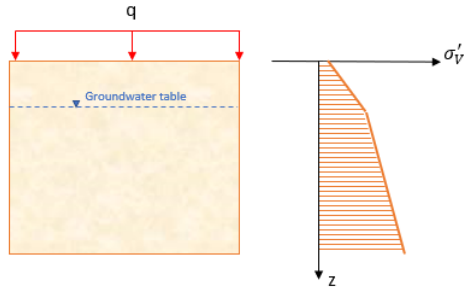
Figure 2.10: Variation of effective vertical stress along the depth.

2.4.2 Horizontal stress

The stresses in soils are not equal in all directions, meaning the horizontal stress is not equal to the vertical stress. A relation between the vertical stress and horizontal stress has been found experimentally and is defined as (Rajapakse 2008)

$$\sigma'_H(z) = K\sigma'_V(z) \tag{2.27}$$

where:

σ'_H = effective horizontal stress   [kPa]

K = lateral earth pressure coefficient   [-]

σ'_V = effective vertical stress   [kPa]

It is important to accurately determine K along the soil profile, estimations can be done by in-situ tests, laboratory measurements on undisturbed soil specimens or indirect field measurements (Pegah et al. 2017). The lateral stress is dependent on the current stress state of the soil, this is further discussed in Chapter 3.

3 Lateral pressure

The main purpose of retaining structures is to resist the lateral earth pressure. The lateral earth pressure, also called the total horizontal stress, σ_H, is expressed with Terzaghi's Principle as

$$\sigma_H(z) = \sigma_H'(z) + u_W(z) \tag{3.1}$$

which is the combination of effective horizontal stress, σ_H', described in Section 2.4.2 and the pore water pressure, u_W described in Section 2.4.1. Insertion of Equation (2.27) gives

$$\sigma_H(z) = K\sigma_V'(z) + u_W(z) \tag{3.2}$$

where:

K = lateral earth pressure coefficient   [-]

σ_V' = effective vertical pressure   [kPa]

u_W = pore water pressure   [kPa]

The lateral earth pressure is consequently a function of the depth in the soil z. The lateral earth pressure coefficient can be calculated with different methods, depending on if the soil is drained or undrained. In this report, only the theories considering drained conditions are described.

Figure 3.1 describes the pressure on a retaining wall from the lateral earth pressure, including the pressure from surcharge and hydrostatic pressure.
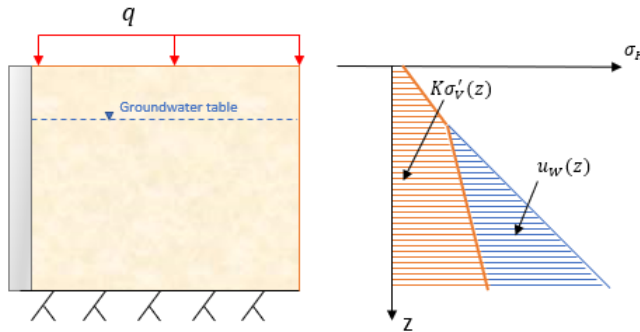
Figure 3.1: Lateral pressure on retaining wall.

The lateral earth pressure coefficient depends on the movement of the retaining structure in relation to the position of the soil (Terzaghi 1944).

3.1 States of lateral earth pressure

The different states of lateral earth pressure are related to the change of the soils structure due to the movement of the retaining wall. If the soil is allowed to expand, the horizontal earth pressure from the soil decreases, this is referred to as active failure of the soil. If the soil instead is compressed, the horizontal earth pressure increases, this is referred to as passive failure of the

soil. If the structure of the soil remains unchanged after installation of the retaining wall, the at-rest pressure is preserved.

The deformation required of the soil in order to generate the different types of lateral earth pressure is not very clearly described in the literature. The deformation needed to fully mobilise an active failure is much less than what is required for the passive failure. For retaining structures that could be considered to yield sufficiently, an active failure of the soil should be assumed. If the required deformation for reaching a certain pressure is not completely developed, the lateral pressure will be somewhere between the active/passive and at-rest pressure. The different states of pressure should thereby be considered as limits of the actual lateral pressure (Craig and Knappett 2012).

The magnitude of soil movement needed to change the pressure state from at-rest pressure is related to the stiffness of the soil. Less stiffness requires more deformations. The minimum lateral deformation required to develop an active failure in a dense sand is 0.25% of the total height of the wall and 1.0% in loose sands. Respectively, the limits for reaching passive failure are $2 - 4\%$ and $10 - 15\%$ (Craig and Knappett 2012).

The lateral earth pressure coefficient, K, is modified depending on what type of pressure is present, and is used to configure the pressure on the wall. If the wall movement is zero, the at-rest pressure will remain unchanged.

3.1.1 Active earth pressure

When a retaining structure moves away due to soil pressure, the soil expands and an active failure develops, shown in Figure 3.2. The expansion of the soil reduces the magnitude of the earth pressure, the active lateral pressure is therefore the lowest state of earth pressure (Rajapakse 2008).
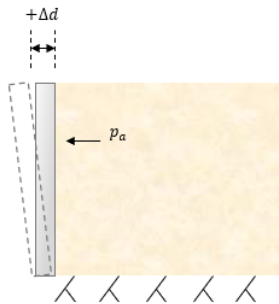
Figure 3.2: Active failure.

3.1.2 Passive earth pressure

When a retaining structure moves towards the soil due to external load, the soil is compacted into a denser structure and a passive failure develops, shown in Figure 3.3. The lateral earth pressure increases because of soil compaction, the passive state is therefore the highest state of lateral pressure (Rajapakse 2008).
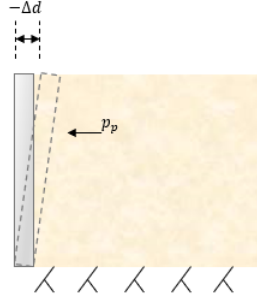
Figure 3.3: Passive failure.

3.1.3 Neutral earth pressure

Before the construction-process of a retaining structure can begin the initial stress state of the soil needs to be known. If the retaining structure is stiff enough so that almost no deformations in the structure takes place, the soil will remain undeformed and the stress state unchanged from the initial state, shown in Figure 3.4.
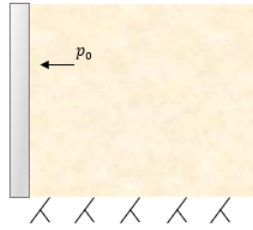
Figure 3.4: At-rest pressure.

The at-rest earth pressure p_0 can be determined by using the neutral earth pressure coefficient K_0.

$$p_0 = K_0 \sigma'_V + u_W \tag{3.3}$$

The neutral earth pressure coefficient is widely accepted as the ratio between the effective vertical and horizontal stress in normally consolidated clays and loose deposits (Michalowski 2005), i.e.

$$K_0 = \frac{\sigma'_H}{\sigma'_V} \tag{3.4}$$

For a normally consolidated soil, the analytical expression

$$K_{0,NC} = 1 - \sin \phi' \tag{3.5}$$

has been derived, regarding the coefficient $K_{0,NC}$ as a function of the effective angle of friction, ϕ', (Verruijt 2018). If the soil is overconsolidated, the at-rest pressure coefficient is affected and calculated as (Mayne and Kulhawy 1982)

$$K_{0,OC} = K_{0,NC}OCR^{\sin \phi'} \tag{3.6}$$

where:

OCR = overconsolidation ratio

3.2 Coulomb's earth pressure

In 1776, the French scientist Coulomb presented his theory considering the state of the lateral earth pressure acting on a retaining structure. Coulomb used the analogy, described in Section 2.3, with the failing soil as a free rigid body and the failure surface as a slope of which the body slides on, to determine the limiting total horizontal force on the wall. The method, based on the assumption of a planar failure surface, analyses a number of potential failure surfaces and the crucial failure surface is identified. Coulomb's model is based on the assumptions that the soil is drained and neglects frictional forces between the retaining wall and the soil (Verruijt 2018).

3.2.1 Active earth pressure

The active earth pressure is assumed to arise from the self weight of a triangular wedge of failing soil which slides along a straight slip plane against the retaining structure. Equilibrium between the retaining structure and the pressure from the failing soil must be reached for all possible slip planes. By identifying the slip plane that leads to the largest load on the structure, the crucial slip plane is found. Figure 3.5 describes the case of active failure of the soil and the forces that must reach equilibrium (Verruijt 2018).
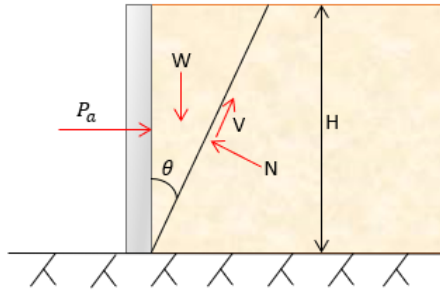
Figure 3.5: Active failure of the soil.

The soil is assumed to be homogeneous, groundwater table at great depth and no surcharge present. The total vertical load from the soil is calculated with the equation

$$W = \frac{1}{2}\gamma H^2 \tan \theta \tag{3.7}$$

where:

W = line load along the wall from the weight of the soil   [kN/m]

γ = unit weight of the soil   [kN/m^3]

H = height of the triangular soil wedge   [kN/m^3]

θ = theoretical angle between the plane of failure and the principal plane

The shear resistance force V can be derived from the expression of the shear strength of the soil, Equation (2.10), by multiplying the cohesion with the length of the slip plane and replacing the normal stress with the normal force N

$$V = \frac{cH}{\cos\theta} + N\tan\phi \tag{3.8}$$

The equations of equilibrium can now be set up and an expression for the active total lateral earth pressure P_a derived

$$(\rightarrow) \quad P_a + V\sin\theta - N\cos\theta = 0 \tag{3.9}$$

$$(\downarrow) \quad W - N\sin\theta - V\cos\theta = 0 \tag{3.10}$$

Equation (3.8) is inserted into the two equations and the shear force V is eliminated

$$P_a = \frac{N}{\cos\phi}\cos(\theta+\phi) - cH\tan\theta \tag{3.11}$$

$$W = \frac{N}{\cos\phi\sin(\theta+\phi) + cH} \tag{3.12}$$

The normal force N is expressed with the load from the soil W in Equation (3.12) and is used to eliminate the normal force in Equation (3.11)

$$P_a = W\frac{\sin\theta\cos(\theta+\phi)}{\cos\theta\sin(\theta+\phi)} - cH\frac{\cos\phi}{\cos\theta\sin(\theta+\phi)} \tag{3.13}$$

The resulting active force, P_a, is now expressed as a function of the angle of the slip plane θ. Equation (3.7) is inserted and various trigonometric relations are used to simplify the expression

$$P_a = \frac{1}{2}\gamma H^2 - \frac{\frac{1}{2}\gamma H^2\sin\phi + cH\cos\phi}{\cos(\theta)\sin(\theta+\phi)} \tag{3.14}$$

The angle of the slip plane corresponding with the largest value on P_a can be determined by identifying the maximum value of the function

$$f(\theta) = \cos\theta\sin(\theta+\phi). \tag{3.15}$$

By taking the derivative of this function and setting it to zero

$$\frac{df}{d\theta} = \cos(2\theta+\phi) \tag{3.16}$$

$$\frac{df}{d\theta} = 0 \quad if \quad 2\theta+\phi = \frac{1}{2}\pi \quad \Rightarrow \quad \theta = \frac{1}{4}\pi - \frac{1}{2}\phi \tag{3.17}$$

the value of θ corresponding to the largest value of P_a is found. By inserting the expression of θ into the second derivative of Equation (3.15)

$$\frac{d^2f}{d\theta^2} = -2\sin(2\theta+\phi) \quad \theta = \frac{1}{4}\pi - \frac{1}{2}\phi \quad \Rightarrow \quad \frac{d^2f}{d\theta^2} = -2 \tag{3.18}$$

the result can be used to determine if the expression of θ is a min or max point. A negative result indicates that it is a max point and a positive result indicates that it is a min point. The result is -2 which indicates that the expression of θ indeed is a max point of the function. The expression

of θ from Equation (3.17) is inserted into Equation (3.14) which, after some elaboration, gives the equation

$$P_a = \frac{1}{2}\gamma H^2 K_a - 2cH\sqrt{K_a} \tag{3.19}$$

where:

K_a = coefficient of active earth pressure, defined as

$$K_a = \frac{1 - \sin\phi}{1 + \sin\phi} = \tan^2\left(\frac{\pi}{4} - \frac{\phi}{2}\right) \tag{3.20}$$

For the cases where groundwater is present and the ground surface is submitted to an external load at the retaining wall, the hydrostatic pressure on the wall and the surcharge must be considered to obtain the total lateral force.

3.2.2 Passive earth pressure

The passive earth pressure is assumed to arise from the self weight of a triangular wedge of failing soil which is pushed aside by the retaining structure. The only difference from the case of active earth pressure is the direction of the shear force, which is now acting in the downward direction as the wedge of soil is being pushed away from the retaining wall. The passive earth pressure is favorable for the stability of the retaining structure and the slip plane that leads to the lowest pressure on the wall therefore needs to be determined to be on the safe-side. Figure 3.6 describes the case of passive failure in the soil and the forces that must reach equilibrium (Verruijt 2018).
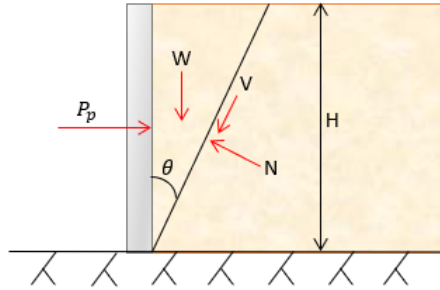
Figure 3.6: Passive failure of the soil.

For homogeneous soils with groundwater table at great depth and no surcharge present, the vertical load from the wedge is calculated as for the active case

$$W = \frac{1}{2}\gamma H^2 \tan\theta \tag{3.21}$$

The equations of equilibrium can now be set up and an expression for the total lateral passive earth pressure P_p is derived in the same manner as for the active case

$$(\rightarrow) \quad P_p - T\sin\theta - N\cos\theta = 0 \tag{3.22}$$

$$(\downarrow) \quad W + qH\tan\theta - N\sin\theta + V\cos\theta = 0 \tag{3.23}$$

After following the same procedure as for the active case, V and N are eliminated. By applying some trigonometric manipulations, the expression of P_p is found as

$$P_p = \frac{1}{2}\gamma H^2 + \frac{\frac{1}{2}\gamma H^2 \sin\phi + cH\cos\phi}{\cos\theta\sin(\theta - \phi)} \tag{3.24}$$

When the denominator in Equation (3.24) has its largest value, the minimum value of P_p occurs

$$f(\theta) = \cos\theta\sin(\theta - \phi) \tag{3.25}$$

The largest value of Equation (3.25) is found through the procedure

$$\frac{df}{d\theta} = \cos(2\theta - \phi) \tag{3.26}$$

$$\frac{d^2 f}{d\theta^2} = -2\sin(2\theta - \phi) \tag{3.27}$$

$$\frac{df}{d\theta} = 0 \quad if \quad 2\theta - \phi = \frac{1}{2}\pi \quad \Rightarrow \quad \theta = \frac{1}{4}\pi + \frac{1}{2}\phi \tag{3.28}$$

By inserting the expression of θ into Equation (3.27), $d^2 f/d\theta^2 = -2$, it is proven that the value of θ indeed corresponds to the maximum value of the function in Equation (3.25). The expression of the minimum passive total earth pressure can now be presented as below

$$P_p = \frac{1}{2}\gamma H^2 K_p + 2cH\sqrt{K_p} \tag{3.29}$$

Where K_p is the coefficient for passive pressure, defined as

$$K_p = \frac{1 + \sin\phi}{1 - \sin\phi} = \tan^2\left(\frac{\pi}{4} + \frac{\phi}{2}\right) \tag{3.30}$$

For the cases where groundwater is present and the ground surface is submitted to an external load at the retaining wall, the hydrostatic pressure on the wall and the surcharge must also be considered to obtain the total lateral force.

3.3 Rankine's earth pressure including Bell's extension for cohesive soils

W.J.M. Rankine was a Scottish engineer who, like Coulomb, studied the lateral earth pressure in the soil. The main difference between their theories is that Rankine studied the variation of the lateral earth pressure along the depth instead of the total lateral force. He used, in 1857, the Mohr-Coulomb failure criterion to establish limiting values for the stresses between the particles in the soil. Rankine's theory is about limits for the coefficient of lateral earth pressure K and is based on the assumptions that the soil is cohesionless and that the retaining wall is completely vertical and frictionless. The backfill is horizontal and the failing soil moves along a planar surface (Verruijt 2018).

Rankine's theory was modified by Bell to cover both friction and cohesive soils. For cohesive soils, the effect of cohesion is considered and a general relation for the lateral earth pressure has been derived (Jumikis 1962).

Rankine's active and passive lateral earth pressure is often denoted as the Rankine states and indicates the upper and lower limit of the actual horizontal stresses, the actual stress will be somewhere in between.

3.3.1 Active earth pressure

For the active case, an expression for the limiting lateral earth pressure is derived by studying Mohr's stress circle. Figure 3.7 shows the stresses in the soil and the corresponding stress circle. The effective horizontal pressure σ'_H corresponds to the minor principal stress σ_3, and the major principal stress σ_1 corresponds to the effective vertical stress σ'_V.
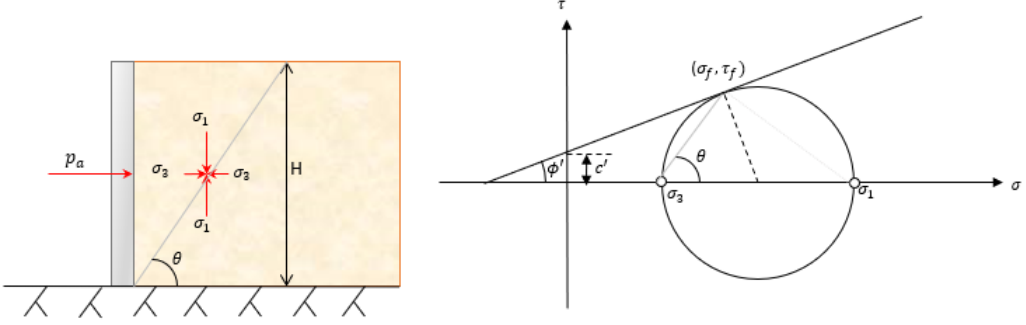
Figure 3.7: Active failure and corresponding stress state.

Rankine presented a general expression of the active lateral earth pressure p_a regarding cohesionless soils by implementing Mohr's relation between the major and minor principal stress, the general equation is written as (Verruijt 2018)

$$p_a(z) = \sigma_H(z) = \sigma'_V(z)K_a + u_W(z) \tag{3.31}$$

Where the active lateral earth pressure coefficient K_a is given by the relation

$$K_a = \tan^2\left(45° - \frac{\phi'}{2}\right) \tag{3.32}$$

Bell modified Rankine's equation by adding a factor including the effective cohesion c' of the soil which resulted in the equation

$$p_a(z) = K_a\sigma'_V(z) - 2c'\sqrt{K_a} + u_W(z) \tag{3.33}$$

The total active lateral earth pressure P_a can be obtained by integrating the lateral earth pressure over the depth

$$P_a = \int_0^z p_a(z)dz = \int_0^z (K_a\sigma'_V(z) - 2c'\sqrt{K_a} + u_W(z))dz \tag{3.34}$$

3.3.2 Passive earth pressure

When the structure is compressing the soil, the lateral earth pressure has its maximum value. The stresses for the passive case is similar to the active, the difference is that the horizontal pressure σ'_H now corresponds to the major principal stress σ_3, and the minor principal stress σ_1 corresponds to the vertical stress σ'_V. Figure 3.8 illustrates the stress state for the passive case.
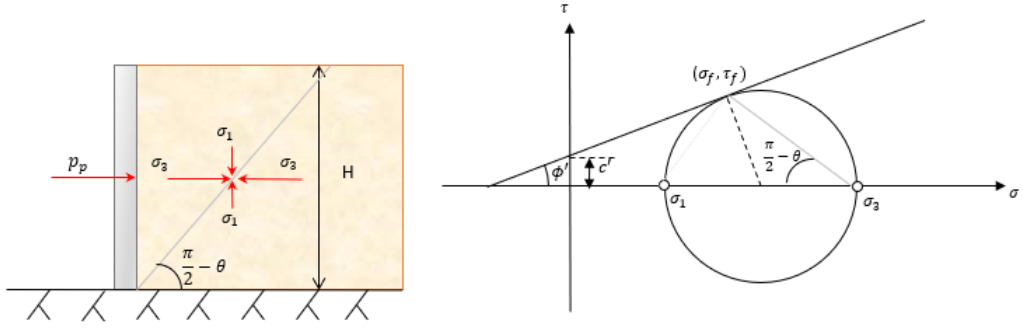
Figure 3.8: Passive failure and corresponding stress state.

Rankine's equation for the passive earth pressure is the same as for the active case. However, Bell's modification takes the effective cohesion c' into account, which increases the lateral earth pressure. Bell's equations for the passive earth pressure is presented as

$$p_p(z) = \sigma_H(z) = K_p \sigma'_V(z) + 2c'\sqrt{K_p} + u_W(z) \tag{3.35}$$

Where the passive lateral earth pressure coefficient K_p is given by the relation

$$K_p = \tan^2\left(45° + \frac{\phi'}{2}\right) \tag{3.36}$$

The horizontal earth pressure, when no groundwater is present, is a linear function of the depth from the surface, the increase of the pressure along the depth for a homogeneous soil is shown in Figure 3.9.
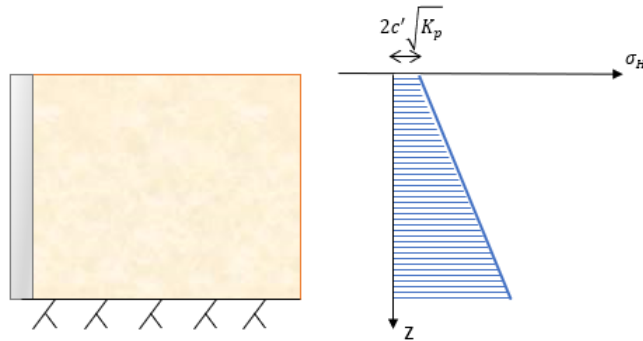
Figure 3.9: Lateral earth pressure along the depth of the soil.

The horizontal pressure, for cohesive soils, has an initial value at the surface and then increases with depth. The total passive lateral earth pressure P_p can be obtained by integrating the lateral earth pressure over the depth

$$P_p = \int_0^z p_p(z)dz = \int_0^z (K_p \sigma'_V(z) + 2c'\sqrt{K_p} + u_W(z))dz \tag{3.37}$$

23

3.4 Wall friction and adhesion

Rankine's and Coulomb's methods to determine the lateral earth pressure give reasonable results for a frictionless wall. In reality, shear forces occur at the interface between the retaining wall and the soil, it is hence advantageous to consider these forces to obtain a more accurate estimation of the lateral earth pressure. The shear force between the wall and the soil arises by frictional forces for friction soils and adhesive forces for cohesive soils. The effects of including the shear force are that the total horizontal force on the wall is reduced and inclined instead of normal to the wall. These effects increase the stability of the wall in most cases.

For the case of active failure, the soil moves downward relative to the wall. For the case of passive failure, the soil is being pushed upwards by the wall. The shear force between the soil and the wall acts in the opposite direction to the soil movement, this is shown in Figure 3.10.

((a)) Shear force on soil for active case.　　　　((b)) Shear force on soil for the passive case.
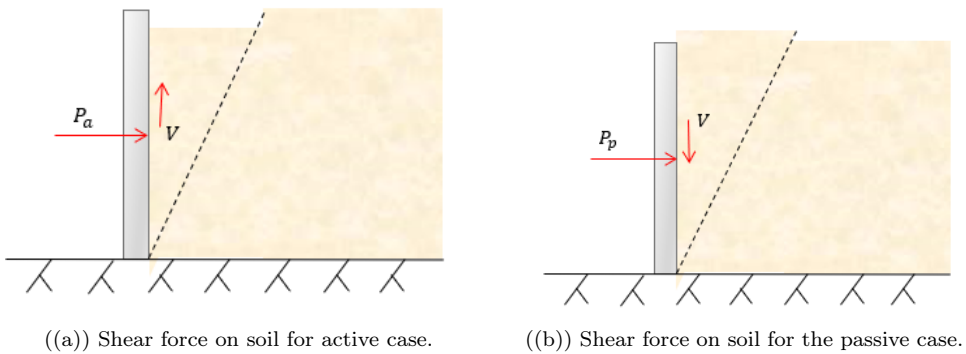
Figure 3.10: Shear force interaction between the soil and the wall.

By taking the shear force between the wall and the soil into account in the equilibrium of forces, the total horizontal force on the wall is reduced for the active case and increased for the passive case. This is implemented by reducing the lateral earth pressure coefficient K_a and increasing K_p (Barnes 2000).

4 Shafts and retaining structures

When constructing underground structures, it is necessary to somehow get access to the subsurface. This is normally done by constructing vertical shafts. When space is limited and slopes is not an option, the walls of the shaft needs to be reinforced by some sort of retaining structure. The retaining structure withstands the lateral soil and water pressure and prevents the excavation from collapsing.

4.1 Retaining structures

The main purpose of retaining structures is to prevent the shaft from collapsing. For this purpose there are many different alternative solutions and the most suitable solution is dependant on the specific project. There is no clear classification of the different frequently used retaining structures, and the classification could either be done from the installation method or from the used material (Fredriksson et al. 2018).

Fredriksson et al. (2018) defines the different failure modes for shafts and retaining structures. There are two main failure categories which has to be considered in design in ultimate limit state - failure of the ground and failure of the structure.

Ground failure includes:

- Total stability

- Rotational stability of the retaining wall

- Stability of of the excavation bottom

- Vertical stability of the retaining wall

- Failure in the anchoring zone (if anchors are used)

Structural failure includes:

- Failure in retaining wall

- Failure in props or anchors

- Failure in waling

The failure modes which must be checked for a specific project is dependent on the chosen structure and the geological conditions in the area. Structural members made from steel or concrete should be designed according to their respective design code.

Fredriksson et al. (2018) also states ultimate limit states for designing retaining structures, namely: STR, GEO, UPL and HYD.

Two frequently used types of retaining structures for deep circular excavations are secant pile walls and diaphragm walls. Both methods build on the principle of dividing the walls into smaller piles/panels which interacts to create a wall. This principle allows for constructing deep shafts with different plan shapes. s

4.1.1 Secant pile walls

Secant pile walls are cast-in-situ piles used to create both permanent and temporary retaining walls in shafts, at a relatively low cost (Åhnberg 2004). The walls are formed by constructing intersecting reinforced concrete piles. Primary (female) piles are installed first, with a spacing in which the secondary (male) piles are installed with an overlap over the primary piles.

The piles are installed prior to excavation of the shaft by drilling and casting the piles in-situ. Different drilling methods can be used depending on the required pile dimensions, pile stiffness and geological conditions. Before the drilling starts, guide walls are installed at the top 0.5-0.8 m of the drilling depth in order to set out the position of the wall (Åhnberg 2004).

By varying the stiffness of the primary and secondary piles, three different types of secant pile walls are achieved, namely: Hard/soft (H/S), Hard/firm (H/F) and Hard/hard (H/H). H/S and H/F secant piles are rather similar in how they are constructed. The difference is the concrete mixture in the primary piles. In the primary piles of the H/S wall, the concrete strength is normally about 1-3 MPa, and in the H/F wall the strength is about 10-20 MPa (Fredriksson et al. 2018). These configurations are in general not used as permanent structures, but can provide an efficient short term waterproof retaining structure. For permanent work applications a reinforced concrete lining is usually required (Skanska 2017). Figure 4.1 shows the typical configuration for H/S and H/F secant pile walls.

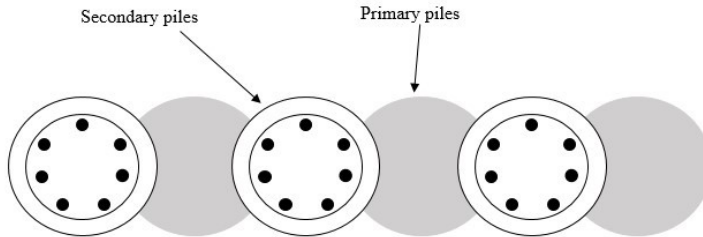Figure 4.1: Schematic figure of H/S and H/F secant pile walls.

The third type of frequently used secant pile wall is the H/H configuration. Here, both the primary and secondary piles are reinforced and constructed by using high strength concrete (Fredriksson et al. 2018). Figure 4.2 shows the typical configuration for a H/H secant pile wall.
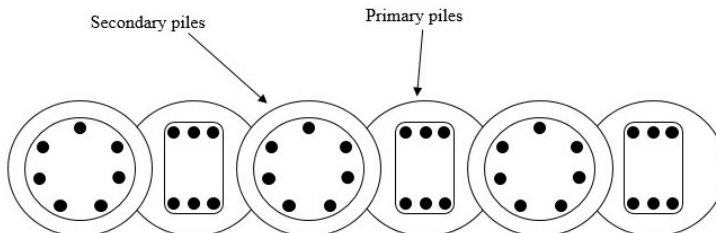

Figure 4.2: Schematic figure of H/H secant pile walls.

A H/H secant pile wall provides a permanent groundwater-controlling retaining structure which could be used at depths spanning around 4-25 m. For deeper excavations it is not recommended to use secant piles as it gets problematic to ensure verticality of the piles (Fredriksson et al. 2018).

In a secant pile wall, the piles normally have a diameter between 0.3 and 2 m. It is possible to vary the dimensions of each pile in a wall, but normally all the piles have the same diameter. The overlapping of the piles creates a dense structure. For adjacent piles, sufficient overlapping is normally achieved with 10-20 % of the pile diameter, or 1/3 of the diameter if soft primary piles are used (Åhnberg 2004). As the wall is built up by piles, the piles can be placed with different geometries, meaning the wall does not need to be formed in a straight line. As secant pile walls can be used for different geometries to form a dense permanent structure, the method could be used to create a circular or elliptical shaft.

4.1.2 Diaphragm walls

A diaphragm wall is a type of retaining structure which has much in common with a secant pile wall. The excavation walls are supported by reinforced cast-in-situ concrete walls, where the walls are built up by several concrete panels (Alén et al. 2006).

The process of constructing a diaphragm wall starts with building guide walls on each side of the intended wall to set out the position, just as is done for the secant pile wall. After the guide walls are installed, the excavation of panels starts. During the excavation, the walls are stabilised by filling the excavation with bentonite slurry. Between each excavated panel a space of one panel-length is left for later. When the first set of panels are excavated, rebar cages are installed and thereafter concrete is poured into the panel to form the wall. Then the process starts over by excavating the soil between the recently formed panels and casting the remaining panels (LTA 2004).

For a permanent wall, it is of great importance to achieve a watertight structure which will not cause any lowering of the groundwater table through seepage into the shaft. The most sensitive areas for seepage in a diaphragm wall are the vertical joints between adjacent panels. This area is extra sensitive as the reinforcement normally does not span between panels, which gives a higher risk of the concrete cracking. The most common method to ensure watertightness is to use sealing tape, which is installed during concreting of the panels. The tape is installed by using a temporary steel casing, a 'stop end', which is removed when the adjacent panel has been excavated, leaving only the tape in the wall. Then the next panel is cast in the same way (Alén et al. 2006). The process is shown in Figure 4.3.
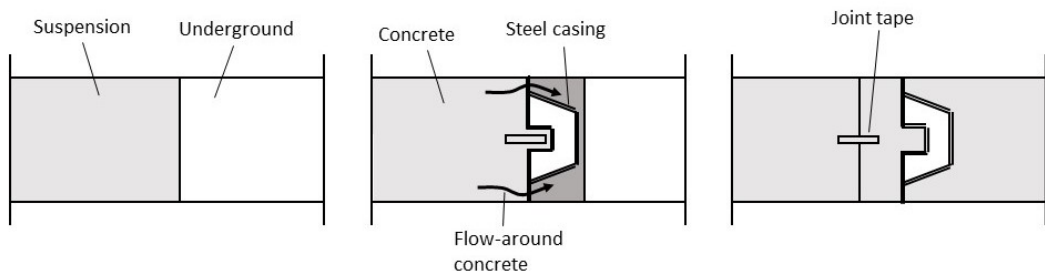
Figure 4.3: Installing of sealing tape with steel casing (Inspired by: Alén et al. (2006)).

It is possible to use more than one tape in a joint, see Figure 4.4, but it is found that one tape is the best solution (Alén et al. 2006).

((a)) One sealing tape ((b)) Two sealing tapes
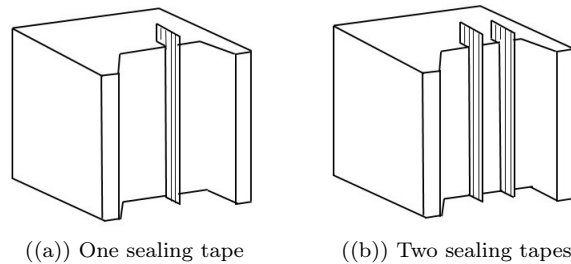
Figure 4.4: Sealing tapes in diaphragm wall panels (Inspired by: Alén et al. (2006)).

When there is an angle between two adjacent panels, a wedge can be used to get the 'stop end' in place, and thereby making it possible to install the sealing in the joint (Vidil 2018).

Depending on the geological conditions and the desired depth, different machines are used for excavating the panels. Either buckets or cutters are used to penetrate the earth. Buckets are more suitable for soft soils and cutters are used for harder formations but not very suitable for clay (Alén et al. 2006). With cutters, the typical excavation depth is in the interval of 5-50 m. With buckets the interval is 5-30 m (Fredriksson et al. 2018). According to Fredriksson et al. (2018), the thickness of the wall can vary between 600-1500 mm and Alén et al. (2006) states that the horizontal length of each panel is normally about 3-6 m.

4.2 Arching effect and line of thrust

In 1675 Robert Hooke formulated the phrase: "As hangs the flexible line, so but inverted will stand the rigid arch". The phrase describes the relationship between a hanging chain, which works in tension, and a standing arch, which works in compression (Block et al. 2006). The idea is simple, stating that by inverting the shape a string takes when exposed to a set of loads, the shape of a rigid arch exposed to the same set of loads is obtained. Figure 4.5 shows the principle of the relationship where the inverted shape gives the shape of an arch working only in compression.

((a)) Only tension
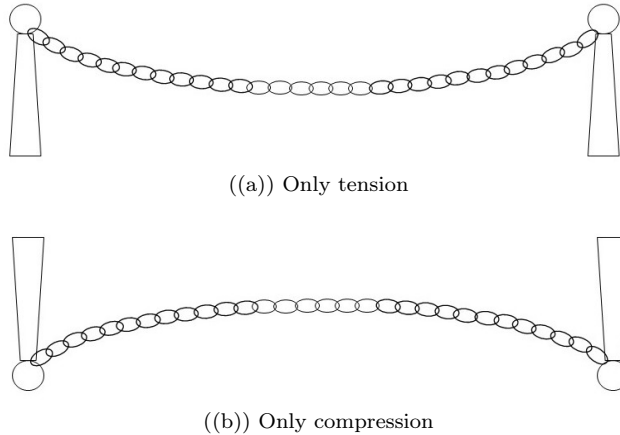
((b)) Only compression

Figure 4.5: A chain in tension and the inverted shape for an arch in compression.

The shape of the chain in Figure 4.5 illustrates the line of thrust. To utilise the arching effect in a structure, meaning that the structure is in equilibrium and only taking compression, the thrust line needs to be entirely within the section of the structure. The thrust line is a theoretical line which represents the path of the resultants of the compressive forces through the arch (Block et al. 2006). The thrust line shows the equilibrium line where only compression appears, which means that different sets of loads give different thrust lines. Figure 4.5 shows a case where only the self-weight of the chain is acting, but by adding a point load somewhere along the chain, a different thrust line can be achieved. For an evenly distributed load along the horizontal direction, however, the thrust line will always be given the form of a parabola (Svenskt Trä 2016).

The concept of the thrust line and arching effect in structures can be utilised to achieve effective use of materials and more slender dimensions. For excavations, the arching effect is of large interest as it can provide effective and simple solutions for retaining structures. The soil and water pressure acting on the retaining wall could in theory be modelled as a uniformly distributed load, which increases with depth, and would thereby give rise to a parabolic line of thrust. For a circular or elliptical shaft, the retaining wall can follow the thrust line and accommodate the benefits of the arching effects by only being exposed to compression.

4.3 Earth pressure on circular and elliptical shafts

When designing a circular retaining wall, the approach is normally to represent the earth, water and surcharge loads acting on the structure as a uniformly distributed external pressure, which varies with the depth. According to Chehadeh (2014), the construction process of a diaphragm/secant pile wall allows the surrounding soil to remain more or less in it's original in-situ stress state as the panels are cast and hardened before excavation of the shaft starts. Also, a circular shape gives a stiff and statically efficient retaining structure which will exhibit only small movements. Due to the small movements, the earth pressure normally remains in at-rest pressure state and not reducing into active pressure state (Chehadeh 2014). An elliptical shaft is not as statically efficient as the circular shape, providing larger deformations of the walls. With larger movements, the possibility of alternating stress states in the soil increases and thereby making it harder to analytically investigate the behaviour of the retaining structure.

The lateral earth pressure acting on a circular shaft can be estimated by using both Rankine's and Coulomb's theories (presented in chapter 3.2 and 3.3). These theories both assume the distribution of earth pressure on a retaining wall to be triangular. From experimental results it is however known that the earth pressure is non-linear and the non-linearity comes from arching effects in the soil (Paik and Solgado 2003). Also, both Coulomb and Rankine developed their theories from the assumption of a plane long-stretched retaining wall. Several authors have tried to extend these theories to study the state of pressure around a vertical circular excavation. Tobar and Meguid (2009) made a comparative evaluation of the different methods, finding that the results from these extended theories are considerably incoherent. It was also concluded that the theoretical solutions gave approximate estimates of the earth pressure valid only for shallow shafts (Tobar and Meguid 2009). Considering arching effects in the soil when evaluating earth pressure would give a reduced pressure from the soil (Jeong et al. 2014). The magnitude of soil arching is also dependant on the stiffness of the retaining wall, where a wall with high stiffness gives less arching in the soil (Jeong et al. 2014). It is therefore recommended to not consider soil arching in design.

4.4 Circular shaft

With circular shafts, the retaining structure will exploit the arching effect and thereby minimising the development of shear forces and bending moments. The applied lateral pressure will generate hoop forces as internal reactions in the support, acting around the entire wall. The hoop stresses are resisted by the concrete strength through the wall thickness and thereby no need for external supports are required (Chehadeh 2014).

4.4.1 Wall stresses

The plan shape of the structure being circular entails effective material use by pressure taken up as hoop forces through the wall thickness. With a perfect circle and strictly controlled verticality of the wall panels, there would only be compression in the structure when exposed to uniformly distributed radial pressure. Hoop stresses occur in circular cross-sections when exposed to uniformly distributed radial pressure. The stresses occurring in the retaining wall can be illustrated by a cylinder exposed to radial pressure, see Figure 4.6.
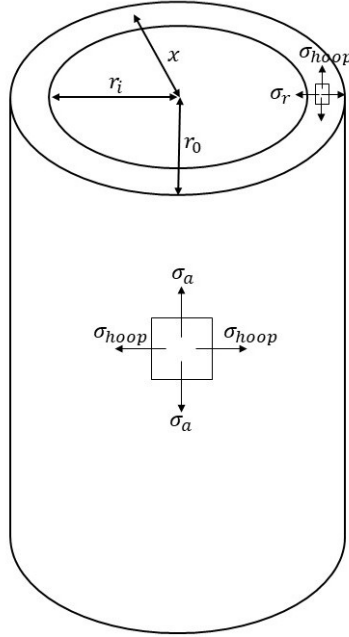
Figure 4.6: Stresses in cylinder exposed to uniformly distributed radial external pressure P.

The three stresses acting in the cylinder, when exposed to external radial pressure P and zero longitudinal pressure, can be obtained as:

$$\sigma_a = 0 \qquad \text{(Longitudinal stress)} \tag{4.1}$$

$$\sigma_{hoop} = \frac{-Pr_0^2(r_i^2 + x^2)}{x^2(r_0^2 - r_i^2)} \quad \text{(Hoop stress)} \tag{4.2}$$

$$\sigma_r = \frac{-Pr_0^2(x^2 - r_i^2)}{x^2(r_0^2 - r_i^2)} \quad \text{(Radial stress)} \tag{4.3}$$

where:

P = external pressure
r_0 = outer radius of cylinder
r_i = inner radius of cylinder
x = radial position in cross-section

Depending on the thickness, t, of the cylinder wall, it is either considered as a thick walled cylinder or a thin walled cylinder. If the thickness is more than $1/10$ of the radius, the cylinder is considered as thick walled, meaning the hoop stresses cannot be assumed to be uniform throughout the wall. For thin walled cylinders, where the thickness is less than $1/10$ of the radius, the hoop stresses are assumed to be uniform and the radial stresses can be disregarded (Chehadeh

2014). The maximum hoop, radial and shear stresses in a thick walled cylinder is obtained as:

$$\sigma_{hoop,max} = \frac{-2Pr_0^2}{(r_0^2 - r_i^2)} \quad \text{at} \quad x = r_i \tag{4.4}$$

$$\sigma_{r,max} = -P \qquad \text{at} \quad x = r_0 \tag{4.5}$$

$$\tau_{max} = \frac{\sigma_{H,max}}{2} \tag{4.6}$$

To fully utilise the arching effect, in the form of hoop forces in the structure, the pressure line/line of thrust needs to be within the thickness of the walls. Both diaphragm walls and secant pile walls are built up by several panels/piles, which complicates the construction of a truly circular shape. If constructed with care and strict control of verticality, the panels can transfer the hoop compression efficiently and thereby giving no bending in the structure. This allows for a structure where no walings, in the form of ring beams, are needed (Puller 2003). Effective stress transfer from one panel to the next is obtained when the line of thrust is located in the middle of the wall thickness throughout the whole circle, see Figure 4.7.
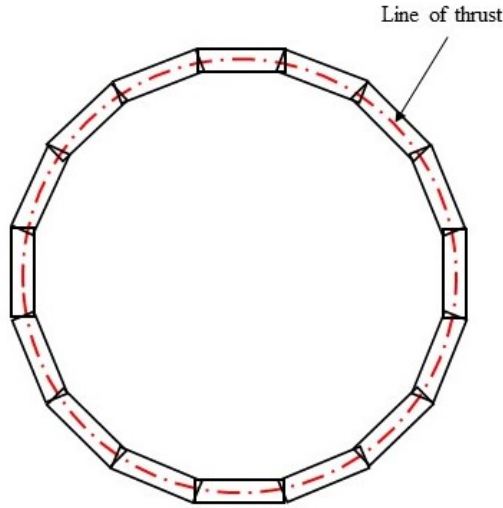
Figure 4.7: Line of thrust in middle of a diaphragm wall thickness.

A panel which is out of plane in verticality will cause problems as the compressive stresses needs to be taken up by a smaller area of concrete. This sort of issues can cause the structure to be unbalanced and bending moments can occur. Puller (2003) puts forward a solution where ring beams are used to manage horizontal bending (bending around a vertical axis) in the wall and vertical bending is taken by the diaphragm wall itself. The hoop forces will then be transferred through both the diaphragm panels and the ring beams. Waling, in the form of ring beams, is often used to reinforce the structure for unbalanced loading and other imperfections of the structure.

4.5 Elliptical shaft

An elliptical plan shape of a shaft is not as structurally efficient as a circular shape, but it provides other advantages which can be of great importance. In a tunnelling project for instance, the elliptical shape has an obvious advantage when it comes to ground space demands, which in urban areas could be a vital factor for the project. When drilling a tunnel, long tunneling equipment needs to be lowered into the shaft. With long objects, the circular shape entails large radius, meaning a big portion of the excavated area is not really needed. With an elliptical shaped shaft however, the excavated area is more efficiently used, allowing long objects to be transported into the shaft and giving less unnecessary excavation space.

4.5.1 Wall stresses

The stresses occurring in an elliptical retaining wall when exposed the uniformly distributed external pressure differ from the circular shaped case and give in-plane bending of the retaining wall. Faustin et al. (2018) conducted a centrifuge test to investigate the stresses in an elliptical shaft lining and came to some conclusions of how the stresses relate to the circular case. It was found that the arching effect is tangible also for the elliptical shape, giving hoop stresses in the wall, and that the areas with minimal curvature on the original elliptical shaft deform towards the centre of the ellipse, creating in-plane bending, see Figure 4.8.
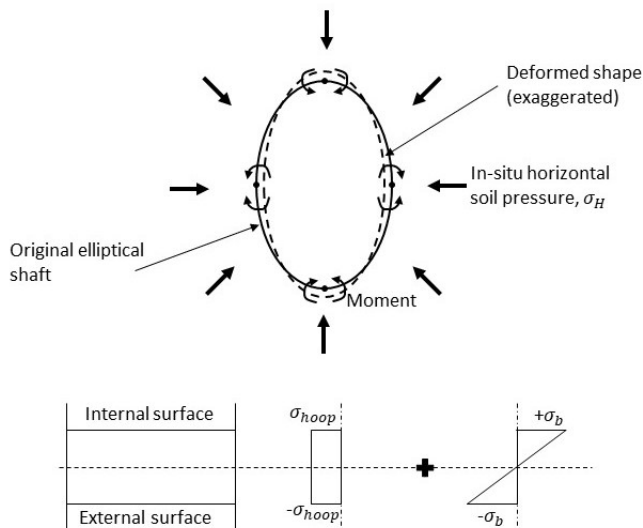
Figure 4.8: Stresses in elliptical shaft lining (Inspired by: Faustin et al. (2018)).

As can be seen in figure 4.8, the shaft elongates during excavation. This elongation can be described from the arching effect. An arch exposed to uniformly distributed load will generate both vertical and horizontal reaction forces in the supports, see Figure 4.9.
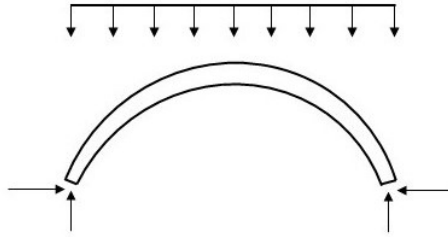
Figure 4.9: Reaction forces in supports.

Bending of the arch is resisted by the horizontal reaction forces, meaning that the arch will elongate and bend if the soil material cannot hold back the horizontal forces from arching. Depending on the magnitude of elongation and subsequent inward movement along the major axis, different states of earth pressure can occur around the shaft. Along the minor axis, the pressure could move to passive state and along the major axis the pressure could move to active state. However, this change of pressure state is helpful for the stability of the structure as the passive state allows for higher earth pressure and the active state allows for lower earth pressure, meaning the soil actually stabilises the structure.

The obtained vertical bending (bending around a horizontal axis) generated in the wall should be small. The hoop stresses can be effectively resisted by the diaphragm panels, if the joints allow for effective load transfer, and the dominant in-plane horizontal bending (bending around a vertical axis) could be resisted by the wall itself or by reinforcing the structure with ring beams (Faustin et al. 2018). According to Ribeiro e Sousa et al. (2012), the practical limit of how elliptic a shaft can be made is given by a relation between the minor and major axis of around 0.5. The limit comes from the fact that when elongating the shaft geometry, the mobilisation of arching along the major axis decreases (Ribeiro e Sousa et al. 2012).

5 Groundwater

The occurrence of groundwater highly influences the construction and design of vertical shafts. Excavations below the water table will encounter inflow of groundwater and the rate of inflow is directly dependent on the hydrogeological conditions of the soil and the size and depth of the shaft. The potential governing the rate of groundwater flow is the hydraulic head. In formations with high hydraulic conductivity, the inflow can be rather high and consequently making the dewatering of the excavation become a significant aspect of engineering construction and design (Freeze and Cherry 1979). Reducing the groundwater level within the shaft is often necessary to allow access for workers and machines and sometimes it is also necessary to lower the groundwater level below formation level and in the surrounding soil. Lowering of the groundwater, and thereby the piezometric head, gives progressive excavation in the dry, reduced pressure on the retaining wall, reduced risk of base uplift at formation level and increased soil strength as effective stress conditions apply to a fully drained soil condition (Puller 2003). However, lowering the groundwater table by pumping will affect the surroundings and is therefore often restricted when it comes to the quantity of abstracted water. Discharge of the pumped water is normally also restricted by legislation with regards to the quality of the water (Puller 2003).

5.1 Groundwater problems

When there is a difference in hydraulic head between the excavation and the surrounding soil, seepage of groundwater into the excavation will occur. With an impermeable wall, the water cannot flow directly into the excavation. This will cause the water to flow downwards in the permeable strata. If the wall does not reach an impermeable layer, the water will continue under the wall and then upwards to formation level (Puller 2003). The upward flow of water in the excavation can cause problems with instability and needs to be analysed carefully. Fredriksson et al. (2018) describes two critical failure modes induced from groundwater which must be checked in design:

- Bottom uplift

- Hydraulic ground failure

Bottom uplift is a failure mode which can occur when there is an impermeable soil layer in the excavation bottom which is underlain with a permeable friction soil, as in Figure 5.1. This allows the upward ingress of water to build up a pressure against the impermeable layer and thereby lifting the bottom of the excavation when the water pressure becomes larger than the weight of the overlaying strata (Fredriksson et al. 2018).
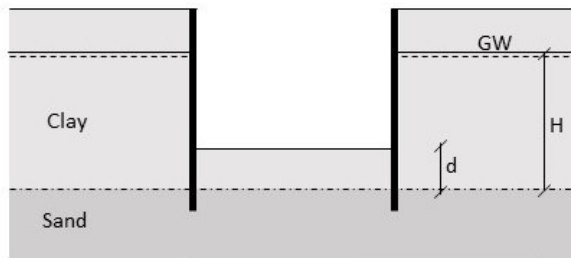

Figure 5.1: Uplift (Inspired by: Fredriksson et al. (2018)).

The criterion for avoiding uplift of the bottom is given by Fredriksson et al. (2018) as:

$$\rho_W g H \leq 0.9 \rho_m g d / (\gamma_d 1.1) \tag{5.1}$$

where:

ρ_W = density of water

ρ_m = density of saturated soil

γ_d = partial coefficient for safety class in design

H = height from groundwater level to permeable layer, see figure 5.1

d = thickness of confining layer in excavation, see figure 5.1

Hydraulic ground failure at formation level, sometimes called liquefaction, is a group of failure modes which reduces the shear strength of the soil. The risk of failure increases in proportion with the head difference inside and outside of the excavation and appears when the upward water pressure gradient in the exit point, i_{exit}, exceeds a critical value, i_{cr} (Puller 2003). Liquefaction appears in mainly two different ways, namely piping and boiling. Piping is a type of inner erosion where the finer grains are removed by the flowing water and thereby creating a weakened soil structure which could collapse when an external load is applied. Boiling is a hydraulic failure type where the soil behaves like a heavy fluid without any shear capacity. This type of liquefaction mainly appears in saturated loose friction soils (Fredriksson et al. 2018). The critical gradient is given by Fredriksson et al. (2018) as:

$$i_{cr} = \frac{\rho_m - \rho_W}{\rho_W \gamma_{R,d}} \tag{5.2}$$

where $\gamma_{R,d}$ is taken as 1.5 for coarse soils and 2.5 for silty soils.

5.2   Methods of groundwater control

To avoid bottom uplift and hydraulic ground failure in the excavation bottom, the inflow of groundwater to formation level needs to be controlled. There are many available techniques for controlling groundwater in excavations. Puller (2003) defines four main methods used to deal with groundwater from deep excavations:

- Stopping surface water from entering the excavation by using, for example, cut-off ditches

- Allowing water to flow into the excavation and subsequently pumping it from drainage sumps

- Pre-draining the soil by lowering the groundwater level ahead of excavating, for example, by use of wellpoint or deep wells

- Stopping the groundwater from entering the excavation by a cut-off wall within the soil

The methods described in this report are focused on the combination of reducing the inflow of water by extending the retaining structure as a cut-off in the soil and the usage of relief wells. By increasing the penetration depth of the retaining walls, the flow path is increased and thereby both the quantity and velocity of the exit water is reduced proportionally (Puller 2003). This would lower the upward water pressure gradient and consequently reduce the risk for liquefaction (Fredriksson et al. 2018). Also the upheaval force from the water is reduced by increased

penetration depth as the quantity of water is reduced.

To achieve a dry excavation, the extended sheeting is often combined with relief wells. Relief wells, also called pressure relief wells or bleeding wells, are a sort of passive wells used to control excess pore water pressure or artesian pressure below an excavation, without using extraction pumps in the wells (Woodward 2005). Relief wells can mitigate the problem of uplift by an engineered pathway for upward seepage into the excavation and thereby improve the stability by reducing the pore water pressure in the excavation bottom. Figure 5.2 illustrates the principle of how relief wells are used in an excavation.
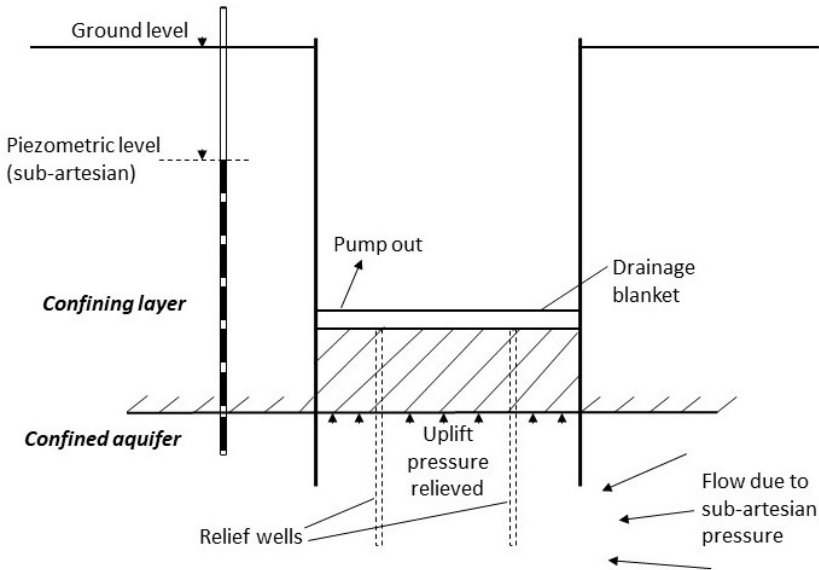
Figure 5.2: Prevention of heave in an excavation by using relief wells (Inspired by: Woodward (2005)).

The use of relief wells will prevent heaving of the excavation bottom if adequate spacing between the well points is used. Woodward (2005) suggests a spacing of 3-10 m in permanent works. Depending on the permeability of the soil beneath the excavation, screens or gravel filling is needed in the wells. Screens are required in high permeability soils and in less permeable soils it is normally sufficient to fill the hole with rounded gravel (Woodward 2005). As there aren't any pumps installed in the wells, the ingress of water is purely due to excess pore water pressure. By using a drainage blanket, the water from the relief wells can be collected in sumps and pumped out with so called sump pumps, see Figure 5.3 (Groundwater Engineering 2015).
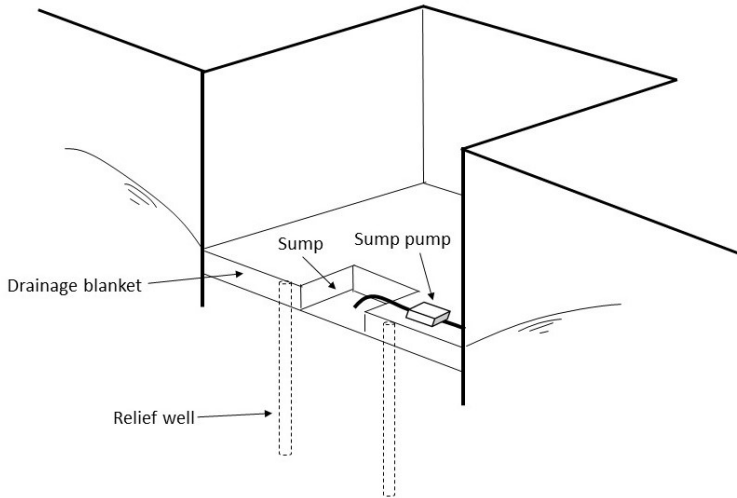
Figure 5.3: Drainage blanket and sumps in excavation (Inspired by: Groundwater Engineering (2015)).

As stated above, there are often restrictions on how much groundwater can be pumped out. It is therefore crucial to be able to model the groundwater situation around the shaft in order to design the dewatering system. Determining the amount of inflowing groundwater can be done graphically by constructing so called 'flow nets', or numerically by using a finite element software.

When pumping out groundwater to obtain a dry excavation, the hydrogeology in the surroundings will be affected with a plausable lowering of the groundwater table. Lowering the groundwater table can damage the surrounding environment by, e.g., decreasing the amount of water in streams and rivers, which could have big effects on the local ecosystem. It can also create settlements in buildings and affect the recharge in nearby wells.

5.3   Water table drawdown

Pumping water from an excavation is rather similar with extraction of water from a well. During well pumping, drawdown of the head in the aquifer around the well will occur. Drawdown around the well creates a pumping cone, also called 'cone of depression' (Fetter 2014). The cone of depression describes how the water table declines around the well. The local drawdown changes with time and the water table declines quicker in the beginning. After some time, the groundwater system will be adjusted to the pumping and the decline stops. This is referred to as 'steady-state drawdown', which means that equilibrium between discharge and recharge is reached. The surrounding area where the drawdown is tangible is called 'zone of influence' (Buddemeier 2000). Figure 5.4 depicts arbitrary cones of depression around a pumping well.
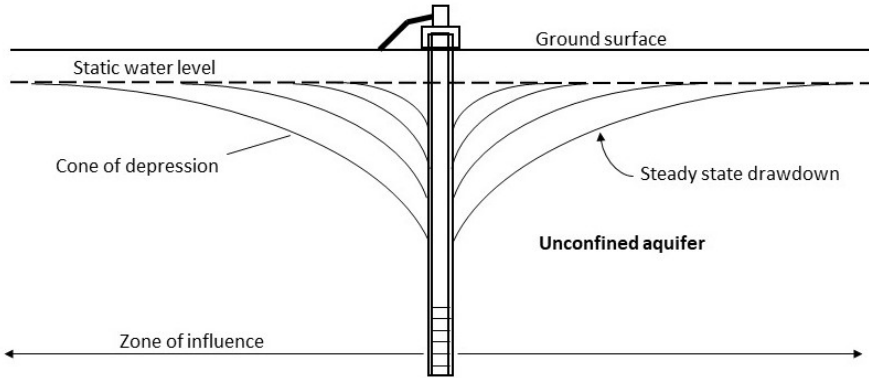
Figure 5.4: Cone of depression and zone of influence (Inspired by: Buddemeier (2000)).

The zone of influence can be evaluated in a finite element software. It can also be roughly evaluated by setting up a water balance equation. However, this requires a known inflow into the excavation (discharge). For a circular excavation, the zone of influence is obtained as a circular area around the shaft. The simplest type of water balance is defined as: $recharge = discharge$. The recharge is often given in mm/year and the discharge is obtained as l/s. With a known discharge, the radius of influence, r_{inf}, can be obtained for different values on the recharge

$$r_{inf} = \sqrt{\frac{discharge \cdot 3600 \cdot 24 \cdot 365}{recharge \cdot \pi}} \tag{5.3}$$

where:

r_{inf} = radius of influence   [m]

$discharge$ = water seepage into excavation   [l/s]

$recharge$ = recharge of groundwater   [mm/year]

6 Finite element modelling

In this project, numerical analyses are performed with finite element softwares. Modelling of soil-structure interaction is made in a commercial finite element software called PLAXIS. A simplified structural analysis is also performed with Autodek's FE-software Robot, this analysis is used to compare the resulting forces in a retaining structure with those obtained in PLAXIS. Finally, a SEEP/W-analysis is performed with GEOSLOPE's FE-software GeoStudio.

This chapter seeks to describe the material model and the constitutive relations used in the soil-structure interaction analysis with PLAXIS. Additional information on the different FE-softwares will also be presented.

6.1 Material model

A characteristic property for soils is that its structure consists of small particles in different shapes and sizes. The structure is often connected to the process that created the soil. Depending on the particulate constituents of the structure, it can be classified as different soil types. Except from particles, soils also consist of gases and water. The mechanical behaviour of the soil depends on the composition of its constituents, another crucial factor is the loading history of the soil. Soils are both an inhomogeneous and anisotropic material and the relation between stress and strain tend to be non-linear (Bujang 2009).

6.1.1 Choice of material model

It is difficult to mathematically simulate the exact behaviour of a specific soil composition due to the complexity of the soil structure and the magnitude of affecting factors. It is therefore more reasonable to simulate the general behaviour for a soil with some idealized properties. A mathematical model with sufficient accuracy to the reality and with safety margins taken into account can be achieved by appropriate simplifications and assumptions. When choosing a suitable material model for the material of interest there is no perfect one, it is more about comparing the advantages against the disadvantages. It is also important to understand the model's limitations when interpreting the result (Bujang 2009).

When choosing a material model there are some basic criteria to evaluate. The material model should be based on basic theoretical principles of continuum mechanics. Secondly, evaluation of the material models to fit experimental tests and the ease to determine required material parameters from standard tests. Finally, the potential of the material model to be implemented numerically into computational calculations also needs to be evaluated (Bujang 2009).

There exists several constitutive models regarding soils, with different levels of sophistication. The number of required material parameters increases with the level of sophistication and in this thesis, only Mohr-Coulombs material model will be used.

6.1.2 Mohr-Coulomb, constitutive relations

When mathematically modelling the behaviour of materials, it is of great importance to define the relation between stresses and strains. Hooke's law

$$\sigma = E\epsilon \tag{6.1}$$

is widely used to describe the linear elastic relation and is suitable for isotropic materials. Hooke's law can not estimate stresses related to failure and is therefore not appropriate for soils, on the other hand it can be used for stiff materials such as concrete. A more suitable stress-strain relation for soils is the linear elastic perfectly-plastic Mohr-Coulomb (MC) model. This model is based on Hooke's law, the stress-strain relation is linear elastic until the stresses becomes high enough for the strains to turn to non-reversible, perfectly plastic. The stress state needed to develop perfectly-plastic strains is utilised to define failure which is desirable for soil models. The stress state is the combination of stresses acting on the material and different combinations of stresses can cause failure. The MC criterion assumes isotropic behaviour and is a function of the largest and smallest principal stresses while it neglects the effect of the intermediate principal stress (Puzrin 2012).

The MC-criterion is based on five input parameters, i.e. Young's modulus, E, Poisson's ratio, ν, internal angle of friction, ϕ, cohesion, c and the angle of dilatancy ψ. These parameters can be determined with ease which contributes to the applicability of the model. One benefit with the MC-criterion is that the computations proceed relatively fast compared to more advanced material models due to the linear elastic relation. The results from the MC-criterion also correlates well with experimental measurements from triaxial compression and extension tests (Puzrin 2012). The model's ability to simulate the failure behaviour in drained conditions is considered generally good. The biggest disadvantage with the MC model is that it uses an average stiffness of each soil layer which entails that the deformations are poorly modelled. The model should therefore be used for a first approximation of the soil deformations (Bujang 2009).

As presented in Section 2.3.2, Mohr-Coulomb's yield criterion can be written as

$$|\tau_f| = c' + \sigma' \tan \phi' \tag{6.2}$$

and Mohr-Coulomb's failure envelope is expressed with principal stresses as

$$\frac{\sigma'_1 - \sigma'_3}{2} = \frac{\sigma'_1 + \sigma'_3}{2} \sin \phi' + c' \cos \phi' \tag{6.3}$$

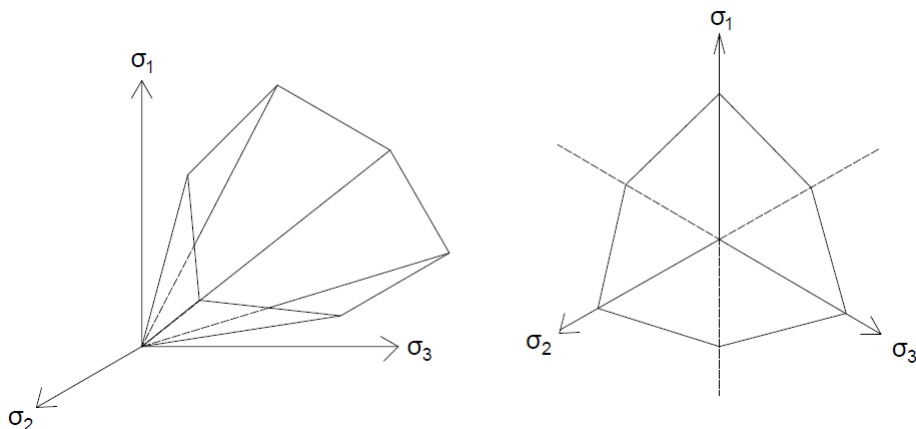Equation (6.3) gives the yield surface in the principal stress space, shown in Figure 6.1.

Figure 6.1: Mohr-Coulomb yield surface in the prinicpal stress space.

The Mohr-Coulomb failure criterion is implemented in finite element calculation methods by expressing the stresses in invariants. The values of the invariants are independent of the direction in the coordinate system. The following equations are used in the finite element method to define Mohr-Coulomb yield equation with the stress tensor invariants. In that way, any stress tensor related to failure can be identified according to Mohr-Coulombs failure criterion (Lagioia and Panteghini 2015).

The stress tensor defines the stresses acting on an arbitrary point in the current configuration of the material and can be presented with the stress matrix

$$\sigma_{ij} = \begin{bmatrix} \sigma_{xx} & \sigma_{xy} & \sigma_{xz} \\ \sigma_{yx} & \sigma_{yy} & \sigma_{yz} \\ \sigma_{zx} & \sigma_{zy} & \sigma_{zz} \end{bmatrix} = \begin{bmatrix} \sigma_{xx} & \tau_{xy} & \tau_{xz} \\ \tau_{yx} & \sigma_{yy} & \tau_{yz} \\ \tau_{zx} & \tau_{zy} & \sigma_{zz} \end{bmatrix} \tag{6.4}$$

The index shows the direction of the stress in relation to the coordinate-system. When the direction of the stress tensor coincides with the direction of the principal stresses, the stress matrix is given by

$$\sigma_{ij} = \begin{bmatrix} \sigma_{xx} & 0 & 0 \\ 0 & \sigma_{yy} & 0 \\ 0 & 0 & \sigma_{zz} \end{bmatrix} \tag{6.5}$$

To visualise the failure surface in the principal stress space, the equation of the failure surface for an isotropic material is given with the stress tensor invariants by

$$F(J_1, J_2, J_3) = 0 \tag{6.6}$$

From the square stress matrix the eigenvalues and their corresponding eigenvectors can be determined to derive the principal stresses and their direction.

$$|\sigma_{ij} - \sigma\delta_{ij}| = \begin{bmatrix} \sigma_{xx} & \tau_{xy} & \tau_{xz} \\ \tau_{yx} & \sigma_{yy} & \tau_{yz} \\ \tau_{zx} & \tau_{zy} & \sigma_{zz} \end{bmatrix} - \sigma \begin{bmatrix} 1 & 0 & 0 \\ 0 & 1 & 0 \\ 0 & 0 & 1 \end{bmatrix} = 0 \tag{6.7}$$

where:

δ_{ij} = Kronecker delta

The eigenvalue problem is solved by finding the value of σ which results in that the determinant of the equation is equal to 0. The determinant of the equation is called the characteristic equation and contains the invariants of the stress tensor. The characteristic equation is given by

$$\det(|\sigma_{ij} - \sigma\delta_{ij}|) = \sigma^3 - I_1\sigma^2 + I_2\sigma - I_3 = 0 \tag{6.8}$$

The invariants of the stress tensor are constant and independent of the orientation in relation to the coordinate system and are given by

$$I_1 = \sigma_{ii} = \sigma_{xx} + \sigma_{yy} + \sigma_{zz} \tag{6.9}$$

$$I_2 = \det\left(\begin{bmatrix} \sigma_{yy} & \sigma_{yz} \\ \sigma_{zy} & \sigma_{zz} \end{bmatrix}\right) + \det\left(\begin{bmatrix} \sigma_{xx} & \sigma_{xz} \\ \sigma_{zx} & \sigma_{zz} \end{bmatrix}\right) + \det\left(\begin{bmatrix} \sigma_{xx} & \sigma_{xy} \\ \sigma_{yx} & \sigma_{yy} \end{bmatrix}\right) =$$
$$= \sigma_{xx}\sigma_{yy} + \sigma_{yy}\sigma_{zz} + \sigma_{xx}\sigma_{zz} - \sigma_{xy}^2 - \sigma_{yz}^2 - \sigma_{xz}^2 = \frac{1}{2}(\sigma_{ii}\sigma_{jj} - \sigma_{ij}\sigma_{ji}) \tag{6.10}$$

$$I_3 = \det \left(\begin{bmatrix} \sigma_{xx} & \sigma_{xy} & \sigma_{xz} \\ \sigma_{yx} & \sigma_{yy} & \sigma_{yz} \\ \sigma_{zx} & \sigma_{zy} & \sigma_{zz} \end{bmatrix} \right) = \sigma_{xx}\sigma_{yy}\sigma_{zz} + 2\sigma_{xy}\sigma_{yz}\sigma_{xz} - \sigma_{xy}^2\sigma_{zz} - \sigma_{yz}^2\sigma_{xx} - \sigma_{xz}^2\sigma_{yy} \quad (6.11)$$

The stress tensor is a sum of the hydrostatic stress tensor $\frac{1}{3}\delta_{ij}I_1$ and the deviatoric stress tensor s_{ij} i.e.

$$\sigma_{ij} = s_{ij} + \frac{1}{3}\delta_{ij}I_1 \quad (6.12)$$

Stresses imposed on a soil will change the volume and the shape of the soil. The hydrostatic stress tensor is the part of the stress that affects the volume change and the deviatoric stress affects the distortion of the soil. The deviatoric stress tensor is obtained by subtracting the hydrostatic stress tensor from the stress tensor i.e.

$$s_{ij} = \sigma_{ij} - \frac{1}{3}\delta_{ij}I_1 = \begin{bmatrix} \sigma_{xx} & \sigma_{xy} & \sigma_{xz} \\ \sigma_{yx} & \sigma_{yy} & \sigma_{yz} \\ \sigma_{zx} & \sigma_{zy} & \sigma_{zz} \end{bmatrix} - \frac{1}{3}\begin{bmatrix} 1 & 0 & 0 \\ 0 & 1 & 0 \\ 0 & 0 & 1 \end{bmatrix}(\sigma_{xx} + \sigma_{yy} + \sigma_{zz}) \quad (6.13)$$

The invariants of the deviatoric stress tensor is obtained by the same procedure as when deriving the principal stresses and stress variants i.e.

$$\det(s_{ij} - s\delta_{ij}) = s^3 - J_1 s^2 - J_2 s - J_3 = 0 \quad (6.14)$$

where J_1, J_2 and J_3 are the invariants of the deviatoric stress tensor which can be expressed with the invariants of the stress tensor as

$$
\begin{aligned}
J_1 &= s_{kk} = 0 \\
J_2 &= \frac{1}{2}s_{ij}s_{ij} = \frac{1}{3}I_1^2 - I_2 \\
J_3 &= \det(s_{ij}) = \frac{2}{27}I_1^3 - \frac{1}{3}I_1 I_2 + I_3
\end{aligned}
\quad (6.15)$$

The expression of Mohr-Coulomb's failure criterion Equation (6.3) is rewritten with the invariants of the stress tensor and the invariants of the deviatoric stress tensor as

$$F = \frac{I_1}{3}\sin\phi' - \sqrt{J_2}\cos\theta - \sqrt{\frac{J_2}{3}}\sin\theta\sin\phi' + c'\cos\phi' = 0 \quad (6.16)$$

where:

$$\frac{\sigma_1' - \sigma_3'}{2} = \sqrt{J_2}\cos\theta, \quad \frac{\sigma_1' + \sigma_3'}{2} = \frac{I_1}{3} - \sqrt{\frac{J_2}{3}}\sin\theta \quad \text{and} \quad \theta = -\frac{1}{3}\sin^{-1}\left(\frac{3\sqrt{3}}{2}\frac{J_3}{J_2^{3/2}}\right) \quad (6.17)$$

The MC-criterion, as all material models, has its limitations. As shown in Figure 6.1, the failure surface has corners and lacks smoothness, leading to the risk of encountering mathematical difficulties during the numerical analysis (Puzrin 2012).

6.2 Description of software

Later in this report, the behaviour of circular and elliptical shafts will be studied in a design example. For this analysis, several different software packages are used. The main focus in the design example lies on the soil-structure interaction, which is analysed in a finite element software called PLAXIS. The analysis in PLAXIS is performed by implementing the Mohr-Coulomb material model.

Two versions of PLAXIS are available, PLAXIS 2D and PLAXIS 3D. A shaft with circular plan shape can be modelled in both versions by using an axisymmetric model in 2D. For the elliptical shape, the two dimensional version is not applicable but requires 3D-modelling. The two versions of PLAXIS are rather similar, but comes with some fundamental differences in e.g. element definitions. A disadvantage with PLAXIS is that it lacks the ability to perform second-order analyses. The level of detail in modelling the structure is relatively low compared to softwares customised for pure structural analyses.

Robot is a 3D professional structural analysis software. The program has the ability to perform simulation of advanced buildings and complex structures. The program offers the possibility to perform second-order effect analyses. However, second-order analyses are not performed in this thesis.

GeoStudio includes an application called SEEP/W. The application offers the ability to perform simulations of the groundwater flow in porous media. SEEP/W can be used for steady state problems and transient analyses. In this thesis, a 2D-version is used which provides the possibility to create axisymmetric models.

6.2.1 2D analysis in PLAXIS

A circular shaft can be built as an axisymmetric model in PLAXIS 2D. Axisymmetry can be defined as a geometry which is symmetric around one axis. The shaft is created by rotation, meaning only half the plane geometry of the shaft is modelled, see axisymmetric example in Figure 6.2. The axisymmetric 2D-model comes with the advantage of being easy to draw and gives a simple overview of the results, aswell as allowing for faster calculations.
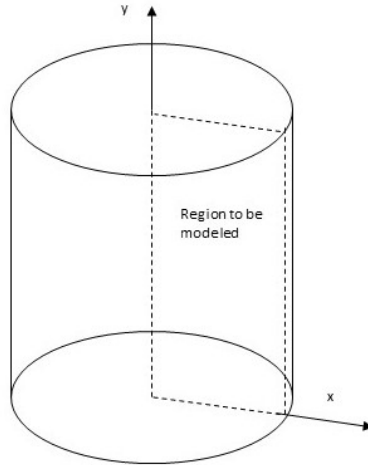
Figure 6.2: Rotational symmetry of a cylinder - axisymmetry.

The finite element method is a numerical calculation method where the model is divided into small elements. For the case of a shaft modelled in PLAXIS 2D there are two main types of elements, namely soil elements and plate elements. In this report, 15-node triangular elements are used for the soil. This is an accurate element which provides a fourth order interpolation for displacements and the numerical integration involves twelve Gauss points - stress points (Plaxis n.d.[a]). The plate elements are composed of 5-node beam elements. Each node in the beam elements has three degrees of freedom:

- Two translational degrees of freedom (u_x, u_y)

- One rotational degree of freedom (rotation in the xy-plane: ϕ_z)

A 5-node plate element contains four pairs of Gaussian stress points where bending moments and axial forces are evaluated, and furthermore extrapolated to the element nodes. The beam elements are based on Mindlin's beam theory, which allows for deflections due to both shearing and bending (Plaxis n.d.[a]). Figure 6.3 shows the position of nodes and stress points in plate elements.
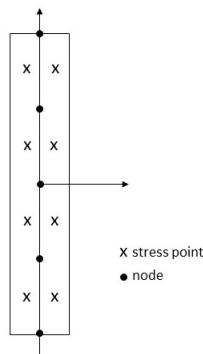

Figure 6.3: Position of nodes and stress points in 5-node beam elements

The most important material properties of plates are the bending stiffness EI and the axial stiffness EA. These input properties determines the equivalent thickness of the plate from the relation

$$d_{eq} = \sqrt{12\frac{EI}{EA}} \tag{6.18}$$

The interaction between soil and structure is controlled by adding interfaces to the plate elements. The interfaces can be used to specify the roughness of the soil-structure contact, R_{inter}, which could be defined as the interface strength. By assigning a strength to the interface, wall friction and adhesion described in Section 3.4, is taken into account in the finite element calculations. In reality, the interface strength is normally weaker and more flexible than the surrounding soil. Therefore the factor should be applied with a value lower than 1, where figures around 2/3 is a reasonable value in absence of detailed information (Plaxis n.d.[a]).

6.2.2 3D analysis in PLAXIS

Using a 3D finite element software, such as PLAXIS 3D, allows for modelling of both circular and elliptical shafts. Conducting a 3D analysis is generally more time consuming and requires more computational power than a 2D analysis. In PLAXIS 3D, the soil elements are 10-node tetrahedral elements, as depicted in Figure 6.4.
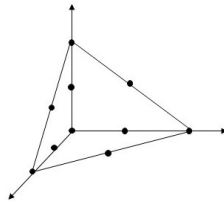
Figure 6.4: 10-node tetrahedral soil element.

Plates in PLAXIS 3D are composed of 6-node plate elements with six degrees of freedom per node:

- Three translational degrees of freedom (u_x, u_y and u_z)

- Three rotational degrees of freedom (ϕ_x, ϕ_y and ϕ_z)

Just as in PLAXIS 2D, plate elements in PLAXIS 3D are based on Mindlin's plate theory. When it comes to specifying the properties of the plate, there are some differences between the two versions. In the 3D-version, the desired thickness of the plate is directly stated in the input program, together with other properties such as Young's modulus and Poisson's ratio. The soil-structure interaction is, just as in PLAXIS 2D, controlled by adding surfaces to structures, which are ascribed with a specific 'strength' (Plaxis n.d.[b]).

7 Design example

To analyse the behaviour of circular and elliptical shafts, a design example is studied. The scope of the design example is not to define a final design of the retaining structure for an elliptical shaft. Instead, it seeks to study the general behaviour of circular and elliptical shafts and to give an estimation of when the elliptical shape reaches it's limit. The elliptical shape needs to utilise the arching effect as far as possible, without being reinforced with ring beams. The foundation depth of the retaining structure is also analysed and a proposal of the required foundation depth will be estimated. This analysis studies the inflow of water into the excavation and how the walls can be used to mitigate this problem. The analyses will only focus on the 'end-product' of the shaft, meaning the long-term effects are of interest and different construction stages will not be analysed.

The example is part of a tunneling project between Malmö and Lund where a new sewage tunnel will be constructed. Vertical access-shafts will be used during construction, and for maintenance and pumping after construction is finished. The tunnel will connect to Sjölunda sewage treatment plant in Malmö, where this particular shaft will be constructed. Another sewage tunnel, extending under central Malmö, was recently constructed and connected to Sjölunda. The investigations from that project are used to build a geo-model and find geotechnical data to be used in the example. Figure 7.1 shows the stretching of the sewage tunnel which will provide data for the design example.
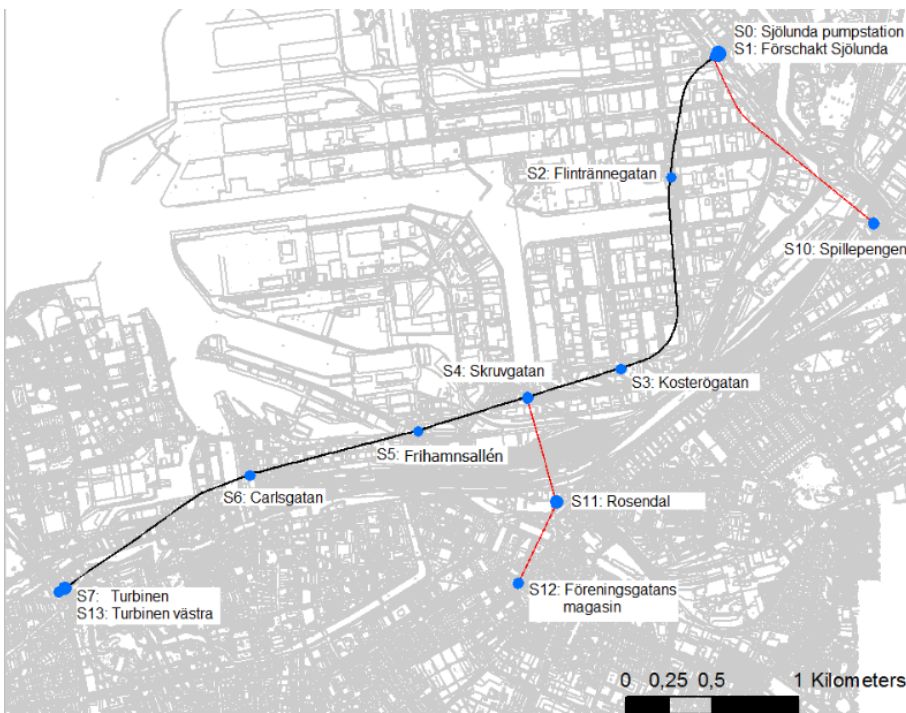

Figure 7.1: Recently constructed sewage tunnel extending under central Malmö (Salomonsson 2017a).

The new tunnel will connect to Sjölunda at a depth of around 30 m, meaning the depth to

excavation bottom in the shaft in this design example will be 30 m. The shaft is also required to have a free opening space of at least 11 m. For a circular shaft this means the inner diameter has to be at least 11 m. For an elliptical shaft it means that the inner diameter on the major axis has to be at least 11 m. The retaining structure will be permanent and has to fulfill the above stated requirements regarding free opening space and depth. As described in Section 4.1, secant pile walls and diaphragm walls are assumed to be able to construct circular and elliptical geometries acting as the retaining structure of the shaft. Secant pile walls are only recommended to be used for excavation depths down to 25 m while diaphragm walls are suitable for excavation depths down to 55 m. Diaphragm walls are therefore selected as the method used to construct the retaining structure for the excavation.

7.1 Geo-model and geotechnical parameters at Sjölunda

In the PM Geo (Salomonsson 2017a), the investigated stratigraphy at Sjölunda is given. By simplifying the given model into purely horizontal layers, a conceptual geo-model is given as described by Figure 7.2, where the groundwater level is situated at $z = -1,5$ m.
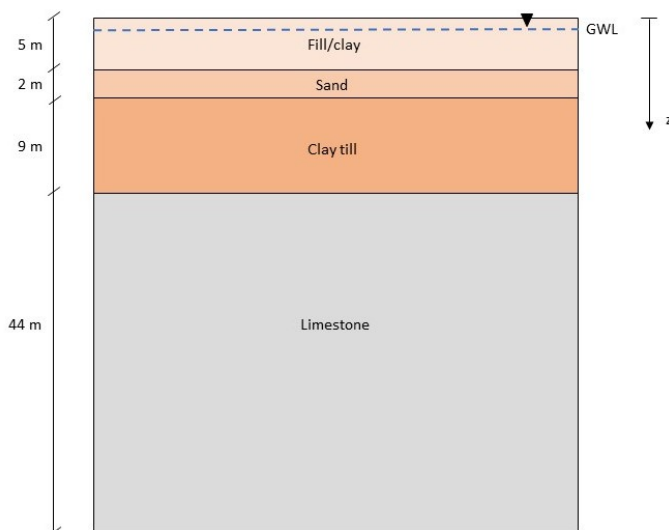
Figure 7.2: Simplified stratigraphy at Sjölunda to be used in design example.

The geotechnical parameters for the different materials are evaluated from PM Geo (Salomonsson 2017a) and MUR - Markteknisk undersökningsrapport (Salomonsson 2017b). Table 7.1 below presents the geotechnical parameters which will be used in the calculations. The retaining structure is permanent and is therefore designed for long-term loading which implies that drained conditions should be applied. The analysis consequently uses drained parameters as the scope is to receive the long-term results.

Table 7.1: Parameters to be used in design example.

Material	γ/γ_s [kN/m³]	E' [MPa]	ν' [-]	c' [kPa]	ϕ' [°]	ψ [°]	OCR [-]
Fill/clay	20/20	10	0.3	0	30	0	1.0
Sand	18/20	10	0.3	0	33	0	1.0
Clay till	22/22	50	0.3	20	34	0	3.0
Limestone	24/24	5000	0.3	100	45	0	3.5

7.2 Geometry and material parameters for retaining structure

The dimensions and material parameters for the retaining structure are based on the rules and recommendations given by different regulations regarding this type of structures. The purpose with this thesis is to simulate the real behaviour of the structure, mean values of the material properties are therefore used to best represent the material in reality. SBUF have compiled guidelines regarding diaphragm walls. The minimum requirement of reinforcement for permanent diaphragm walls in the vertical direction is $\phi16$ s150 and for the horizontal stirrups $\phi10$ s150. The concrete cover should not be less then 75 mm (Alén et al. 2006).

Based on the guidelines mentioned above, a cross-section for the diaphragm wall is determined. Having a wall thickness of 800 mm entails increasing the diameter of the horizontal stirrups from $\phi10$ to $\phi16$, in order to fulfill the requirement of minimum amount of reinforcement. The cross-section of the wall is illustrated in Figure 7.3.
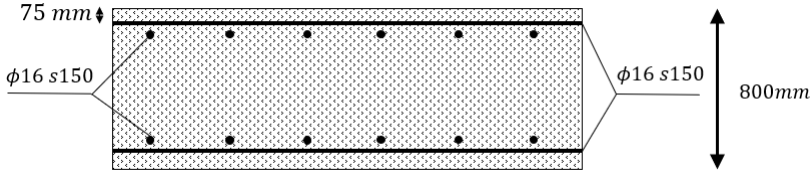
Figure 7.3: Cross-section of the diaphragm walls

The material parameters for the diaphragm wall is given in Table 7.2.

Table 7.2: Geometry and material parameters for the diaphragm walls.

Material	Quality	E_{cm} [GPa]	E_s [GPa]	ν [-]	f_{cm} [MPa]	f_{yk} [MPa]
Concrete	C35	34	-	0.2	43	-
Reinforcement	B500B-T	-	200	0.3	-	500

The retaining wall is a permanent structure and the behaviour of the structure after long time is of interest. The Young's modulus E_{cm} is reduced over time to an effective Young's modulus $E_{c,ef}$ due to creep and shrinkage of the concrete. The creep coefficient $\phi(\infty, t_0)$ is assumed to

be 2.0 which gives the effective Young's modulus

$$E_{c,ef} = \frac{E_{cm}}{1 + \phi(\infty, t_0)} = \frac{34}{1 + 2} = 11.33 \text{ GPa} \qquad (7.1)$$

The stiffness is also reduced due to the appearance of cracks in the concrete after long time. It is desirable for the diaphragm walls to be almost impermeable to water which means that restricted development of cracks is allowed. The concrete is therefore assumed to remain relatively uncracked and the reduction factor ζ is set to 0.8. The final stiffness after long time is

$$E_{c,\infty} = E_{c,ef}\zeta = 11.33 \cdot 0.8 = 9.1 \text{ GPa} \qquad (7.2)$$

8 Groundwater control

Constructing subsurface structures requires analyses regarding the structure's impact on the groundwater situation. This chapter seeks to study the groundwater situation in the design example presented in Chapter 7. The applicable conclusions will later be implemented in the further analyses of the shaft.

As shown in Figure 7.2, the groundwater level is located close to the ground surface. Meaning a major part of the vertical shaft will be located under the groundwater level and the interaction between the groundwater and the retaining structure is therefore of interest to analyse. The purpose with the analysis is to evaluate the risk for different groundwater related problems and to identify the minimum required foundation depth of the retaining structure to prevent the groundwater related issues from occurring. The analysis is only performed regarding a circularly shaped shaft, but the results are assumed to be adjustable and implementable on the elliptical shape as well.

The following issues are to be evaluated:

- Zone of influence when pumping out groundwater from the excavation. Lowering the groundwater surface with 0.3 m is regarded as uninfluenced.

- Determining an appropriate foundation depth of the retaining structure. The seepage into the shaft is desired to not exceed 0.5 l/s.

- Sensitivity analysis regarding the impact of hydraulic parameters.

Normally, the risk of hydraulic ground failure and bottom uplift also needs to be checked. As there is limestone in the excavation bottom in this design example, the risk of these failure modes to develop is regarded to be very low, and is hence not analysed. Limestone being a cohesive material drastically reduces the risk of hydraulic failure. Upheaval of the excavation bottom could happen in theory if the limestone functions as a impermeable layer in the bottom of the excavation. However, in this design example the limestone is believed to be sufficiently permeable to mitigate the risk of upheaval, and the upward pressure can presumably be managed through the dewatering system.

8.1 Method

The interaction between the groundwater and the structure is analysed with an FE-software. In this thesis, a software from GeoStudio is used to perform a SEEP/W steady state analysis. The symmetry of the circular shaft is used to create an axisymmetric 2D-model of the shaft in the FE-software. A plausibility assessment of the numerical results obtained from the FE-calculations is made through a simple water balance equation.

Two different FE-models are analysed. One where the groundwater level is defined with an initial level and then calculated by an equilibrium analysis of the seepage and recharge of groundwater. This model is referred to as Model 1 and represents the conditions during the winter season. In the other model, the groundwater level is set to a fixed level. This model is referred to as Model 2 and represents the conditions during the summer season. The influence of the input parameters is analysed by performing calculations with parameters representing the worst case and with parameters representing the best case. The results are then compared. The influence of the foundation depth is analysed by performing a parametric study with foundation depths.

8.2 Parameters

In this analysis, the parameters presented in Table 7.1 and Table 7.2 are used to create the calculation models. Parameters regarding the hydraulic conductivity, K, are introduced in Table 8.1. The hydraulic conductivities are retrieved from PM Geo (Salomonsson 2017a) and are assumed to be orientation independent.

Table 8.1: Interval of hydraulic conductivities in soil material.

Material	K [m/s]
Fill/clay	10^{-4} - 10^{-6}
Sand	10^{-4} - 10^{-6}
Clay till	10^{-7} - 10^{-8}
Limestone	10^{-5} - 10^{-6}
Diaphragm walls	10^{-8} - 10^{-15}

8.3 Numerical FE-analysis

Models are created in the FE-software to represent the stratigraphy shown in Figure 7.2, the parameters for the soil and structure are defined according to Table 7.1 and 7.2. First, an analysis is performed for the soil profile without the shaft included, the model includes a ground surface area represented by a circle with a radius of 1000 m. The result from this analysis is used as the initial condition for the further analyses. Two models are then created as described in Section 8.1 from the initial conditions. For Model 1, the groundwater level is not defined as permanent, instead a recharge is applied at the ground surface of 100 mm/year. For Model 2, the groundwater level is set as fixed at 1.5 m below ground surface at a distance of 1000 m from the shaft. The two models are shown in Figure 8.1.
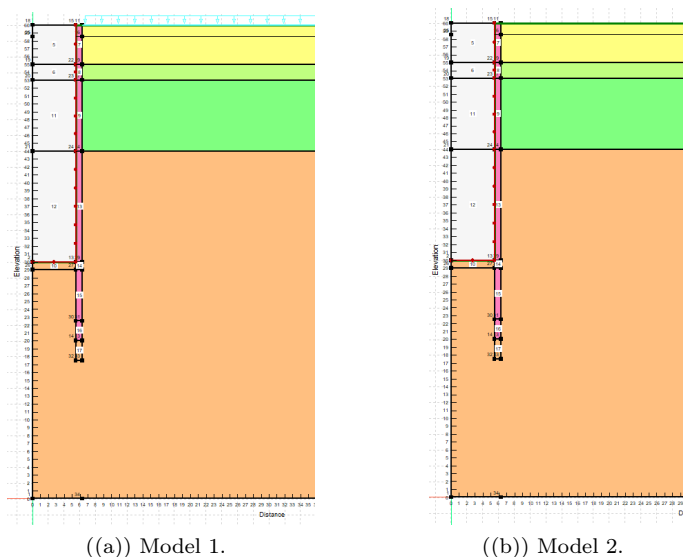

((a)) Model 1. ((b)) Model 2.

Figure 8.1: The models created in the FE-software.

Calculations are performed for the worst and best case of hydraulic conductivity parameters. The best case is when the hydraulic conductivity parameters are set to the lowest value presented in Table 8.1, the worst case is the when the highest values are applied. Table 8.2 shows the values used for the two cases.

Table 8.2: Hydraulic conductivity's for worst and best case.

Material	Worst K [m/s]	Best K [m/s]
Fill/clay	10^{-4}	10^{-6}
Sand	10^{-4}	10^{-6}
Clay till	10^{-7}	10^{-8}
Limestone	10^{-5}	10^{-6}
Diaphragm walls	10^{-8}	10^{-15}

A parametric study is executed regarding the foundation depth of the retaining wall by performing calculations for the foundation depths of 7.5 m, 10 m and 12.5 m below excavation bottom. From the numerical calculations, the resulting total seepage into the shaft is extracted for every combination of worst and best case regarding the hydraulic conductivity parameters and foundation depth of the retaining structure. The results are presented in Table 8.3.

Table 8.3: Total seepage into the shaft.

Foundation depth [m]	Model 1 Worst [l/s]	Best [l/s]	Model 2 Worst [l/s]	Best [l/s]
7.5	2.72	0.26	2.50	0.22
10	2.27	0.20	2.11	0.18
12.5	2.02	0.17	1.84	0.16

For Model 1, the recharge causes the groundwater level to reach the ground surface. The conditions for Model 1 are therefore favorable compared to Model 2 when analysing the zone of influence, which implies that only Model 2 is used when analysing the zone of influence. The resulting groundwater drawdown obtained in Model 2 is shown in Figure 8.2. The different lines symbolises the worst and best cases of hydraulic conductivities in combination with the different foundation depths of 7.5 m, 10 m and 12.5 m.
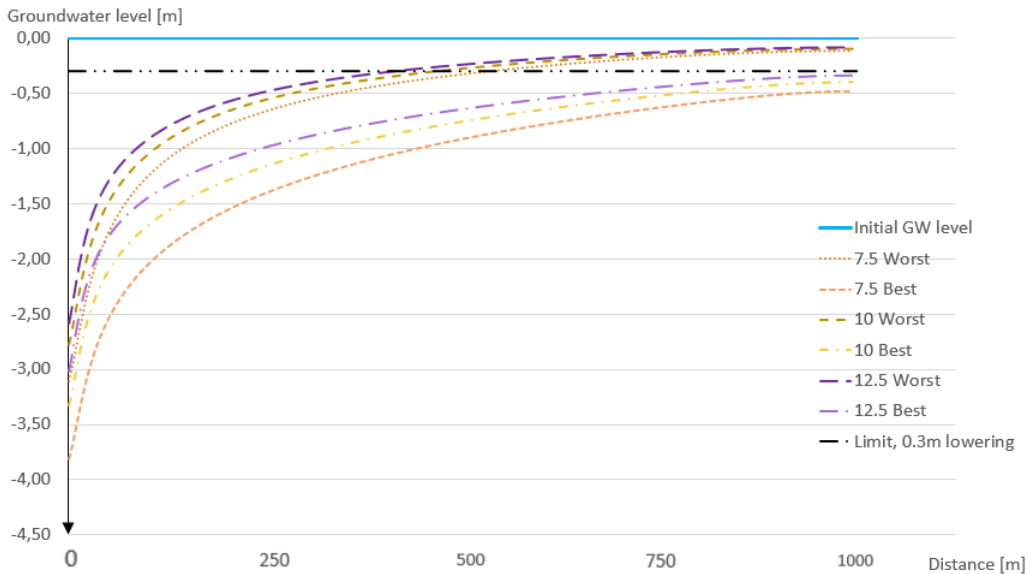
Figure 8.2: Zone of influence for different cases.

As shown in Figure 8.2, the groundwater level is lowered by 0.3 m within a radius of 400-500 m when the worst values of the hydraulic conductivities are applied. The foundation depth of the retaining wall does not appear to have any significant impact of the influenced radius. For the case when the best values of the hydraulic conductivities are applied, the radius of influence seems to be larger than 1000 m.

8.4   Water balance - Radius of influence

The water balance described in Equation (5.3) is also used to provide a rough estimate of the radius of influence. The seepage into the shaft obtained from the numerical FE-calculations are required to be in equilibrium with the recharge of groundwater. By assuming different recharges at the ground surface, it enables for evaluations of the radius required for the specified recharge and seepage to reach equilibrium. The radius of influence corresponding from the lowest and largest seepage obtained from the numerical FE-calculations is presented in Table 8.4 with recharges ranging from 20-200 mm/year.

Table 8.4: Radius of influence.

Recharge [mm/year]	Seepage [l/s]	Radius of influence [m]	Seepage [l/s]	Radius of influence [m]
20	2.72	1169	0.16	283
50	2.72	739	0.16	179
100	2.72	523	0.16	127
200	2.72	370	0.16	90

56

8.5 Conclusion and discussion

The sensitivity analysis regarding the impact of the hydraulic conductivity parameters shows that the corresponding seepage into the shaft ranges from 0.16-2.72 l/s. This means that there is a risk that the limiting inflow of 0.5 l/s is exceeded. The parametric study shows that the influence of the foundation depth on the seepage decreases as the foundation depth increase. To reduce the seepage by increasing the foundation depth, it must be weighed against the increased costs that comes with it. The effect of increasing the foundation depth from 10 m to 12.5 m is considered to not have a sufficient impact to be entitled. The foundation depth of 10 m is therefore used in further analyses.

As shown in Figure 8.2, it seems that the radius of influence is greater when the best values of the hydraulic conductivities are applied compared to when the worst values are applied. Logically, the worst values, giving higher conductivity, should be entailing higher seepage and thereby giving a larger zone of influence. When looking at Table 8.3, the higher conductivities are indeed providing larger seepage volumes. The water balance in Table 8.4 also states that a higher seepage should give a larger zone of influence. Based on these arguments, it is assumed that the results showing a larger zone of influence with the lower conductivities probably is an error. One theory is that the error originates in the clay till layer, which functions as a groundwater separating layer. Both the overlying sand and the underlying limestone has higher conductivities than the clay till, in the best case as well as in the worst case. This makes it hard to accurately define the groundwater flow and is therefore believed to be the cause of the nonconforming results.

When using the worst case hydraulic conductivities, corresponding with the highest seepage, a radius of influence of around 500 m is obtained. This also seems as a reasonable value when looking at the results from the water balance. As this result builds on the highest seepage, the conclusion is that this should correspond to the largest radius of influence possible for this shaft.

9 Soil-structure interaction

In this chapter, the design example described in Chapter 7 continues with analyses of the soil-structure interaction and the resulting forces in the retaining wall. The emphasis is related to how the shaft's geometry affects the interaction of earth pressure and structural forces.

9.1 Method

To evaluate the soil-structure interaction for circular and elliptical shafts, the FE-software PLAXIS is used. The evaluation starts from a circularly shaped shaft. The circular shaft can be analysed in both PLAXIS 2D with an axisymmetric model and in PLAXIS 3D. In addition to this, a simplified structure is analysed in the structural FE-software Robot 3D. The simplified approach uses the earth pressures obtained in PLAXIS and gives the forces, such as hoop forces and moments, in the structure. If this method proves to be successful, it can be used to study the elliptical geometry in a simplified manner.

The earth pressures obtained from PLAXIS are verified with hand calculations where the lateral earth pressure can be calculated according to Coulomb's and Rankine's earth pressure theories. The circular shape also allows for hand calculation of hoop stresses in the structure according to the cylinder stress theory presented in chapter 4.4.1, meaning the hoop stresses in the FE-models can also be verified with analytical results. A comparison and discussion of the results is presented in Section 9.3.5. The scope is to verify the PLAXIS 3D model to be able to use it for the elliptical geometry, and to assess if the simplified method in Robot could be useful.

Having a verified model in PLAXIS 3D allows for studying an elliptically shaped shaft. This is done by using the same model as for the circular case and gradually elongating the shaft's geometry into a more elliptical shape. By conducting a parameter study on different elliptical geometries, conclusions on how the geometry affects the soil pressure and structural forces can be drawn. Through these conclusions a proposal will be produced, stating an optimised elliptical geometry for a shaft, given the geological conditions in the specific area.

The design example uses diaphragm walls as retaining structure. As mentioned in Section 4.4.1 and depicted in Figure 4.7, diaphragm walls will not create a perfect circle, or ellipse. This is however simplified in the FE-models, where the walls are created as more or less perfectly circular/elliptical plates.

9.2 Parameters and load model

The model in PLAXIS uses the Mohr-Coulomb soil model explained in Section 6.1. Used geotechnical parameters are presented in Table 7.1 and additional information on the model is given in Table 9.1. The used material properties for the wall are presented in Table 7.2 and Equation (7.2).

In PLAXIS, the at-rest earth pressure coefficient, K_0, can be specified manually or generated automatically. If automatically generated, K_0 is calculated according to Equation (3.5), which is valid for normally consolidated soils. In Table 7.1, the evaluated OCR is stated for each material layer. Both the clay till and the limestone are over-consolidated, which means K_0 is instead evaluated according to Equation (3.6) as described in Section 3.1.3, and thereby K_0 is specified manually in PLAXIS for these materials. Table 9.1 below, presents the used values of K_0 and R_{inter} in the PLAXIS models. Where R_{inter} specifies the interface strength, as described in Section 6.2.1.

Table 9.1: Additional parameters used as input in PLAXIS.

| Material | Soil model | Drainage type | K_0 | R_{inter} |
	[-]	[-]	[-]	[-]
Fill/clay	Mohr-Coulomb	Drained	0.5	0.7
Sand	Mohr-Coulomb	Drained	0.46	0.7
Clay till	Mohr-Coulomb	Drained	0.81	0.7
Limestone	Mohr-Coulomb	Drained	0.71	0.7

Parameters such as shear modulus G and oedometer modulus E_{oed}, are evaluated automatically in the software from the the parameters stated in Table 7.1. The following relations are used to determine these parameters in PLAXIS (Plaxis n.d.[a]):

$$G = \frac{E'}{2(1 + \nu')} \tag{9.1}$$

$$E_{oed} = \frac{E'(1 - \nu')}{(1 + \nu')(1 - 2\nu')} \tag{9.2}$$

The diaphragm walls are defined in Section 7.2. In the soil-structure interaction analysis, the retaining structure extends 10 m below excavation bottom to a total depth of 40 m. The concrete is modelled as an elastic material. By modelling it as fully elastic, no plastic limits are defined, giving the full magnitude of forces affecting the walls. These forces are later compared with the capacity of the wall, which is estimated by hand calculations, to determine if the structure is failing.

Only geotechnical loads are considered, which results in a symmetrical loading of the retaining structure and gives a general understanding of how the shape of the shaft affects the capacity. Surcharge from e.g. machines and other equipment will not be considered as it would cause an asymmetrical load situation. This would make the analysis of the shape more difficult and is therefore not considered in this case. It is however known that the asymmetrical case could very well be the worst load situation and needs to be considered in a final design. Providing a final design of the structure is however not the scope of this project.

9.3 Analysis of circular shafts and verification of model

In Section 9.3.1 - 9.3.4 below, the circular shaft will be analysed through different methods. The results are then compared in Section 9.3.5. The scope is to be able to verify the models and then proceed with analysing an elliptical shaft.

9.3.1 Analysis of the soil-structure interaction in PLAXIS 2D

The 2D-analysis is made through an axisymmetric model, creating a circular shaft with the diameter of 11 m. The used parameters for the soil materials and concrete walls are defined in Table 7.1, 7.2 and 9.1. PLAXIS uses 'Staged construction' which means that several stages of the shaft construction and the corresponding stress states can be analysed. However, in this project the scope of the modelling is to analyse the 'end-product' of the shaft, which means that only the results from the final stage of construction will be considered.

The construction of the shaft is divided into five different phases in PLAXIS. In the initial phase, the initial conditions of the soil is generated giving the initial stress state in the soil. In the next phase the wall is activated, and in the following phases excavation starts by deactivating soil layers inside the shaft. At each excavation phase, also the groundwater level is lowered to be located at the depth of excavation. In the fifth phase, the excavation reaches the desired depth of 30 m. Figure 9.1 below shows the excavated shaft and the water levels of each phase.
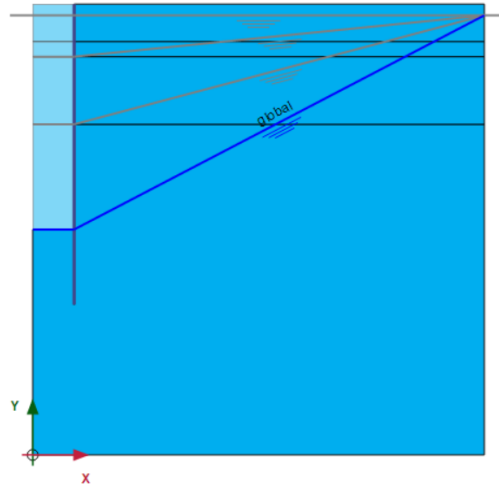
Figure 9.1: Excavation phases and corresponding groundwater levels. The light blue colour indicates excavated regions.

The mesh is generated by using the standard element distribution option 'fine' in PLAXIS. However, the plate elements and the soil elements inside the shaft are modified by adjusting the coarseness factor to 0.1 in order to obtain a more precise mesh. When all calculation phases are finished, the deformed mesh can be studied. Figure 9.2 shows both the deformed and undeformed mesh, where the deformed mesh represents the mesh after the last calculation phase is finished. Note that the deformed mesh in the figure below is exaggerated $5 \cdot 10^3$ times. The maximal obtained total deformation in the retaining wall is obtained as $|u| = 1.2$ mm and occurs at a depth of $z = -13.75$ m, approximately in the border between the clay till and the limestone.

((a)) Undeformed mesh.

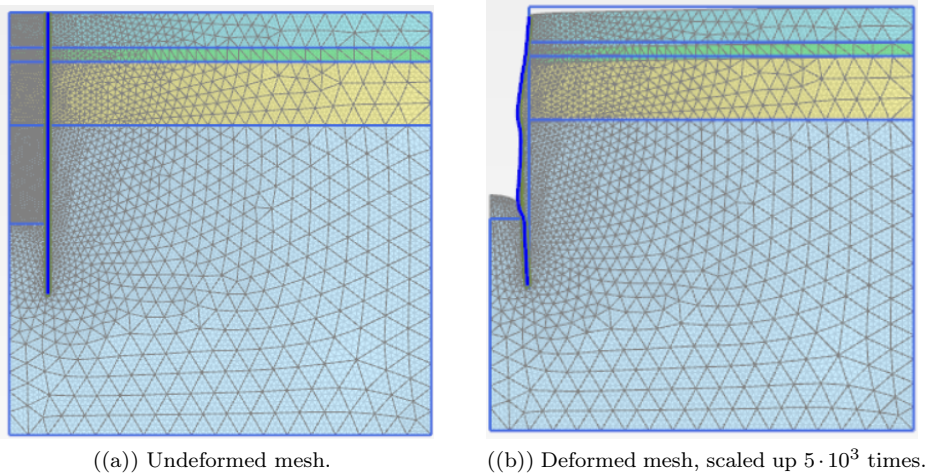((b)) Deformed mesh, scaled up $5 \cdot 10^3$ times.

Figure 9.2: Undeformed and deformed mesh.

Correct modeling of the groundwater-lowering inside the shaft is crucial. As a verification of reasonable results the pore water pressure in each calculation phase is plotted in Figure 9.3. The figures show how the groundwater head is lowered inside the shaft but remains unaffected outside the shaft. This provides the worst load case for the structure.
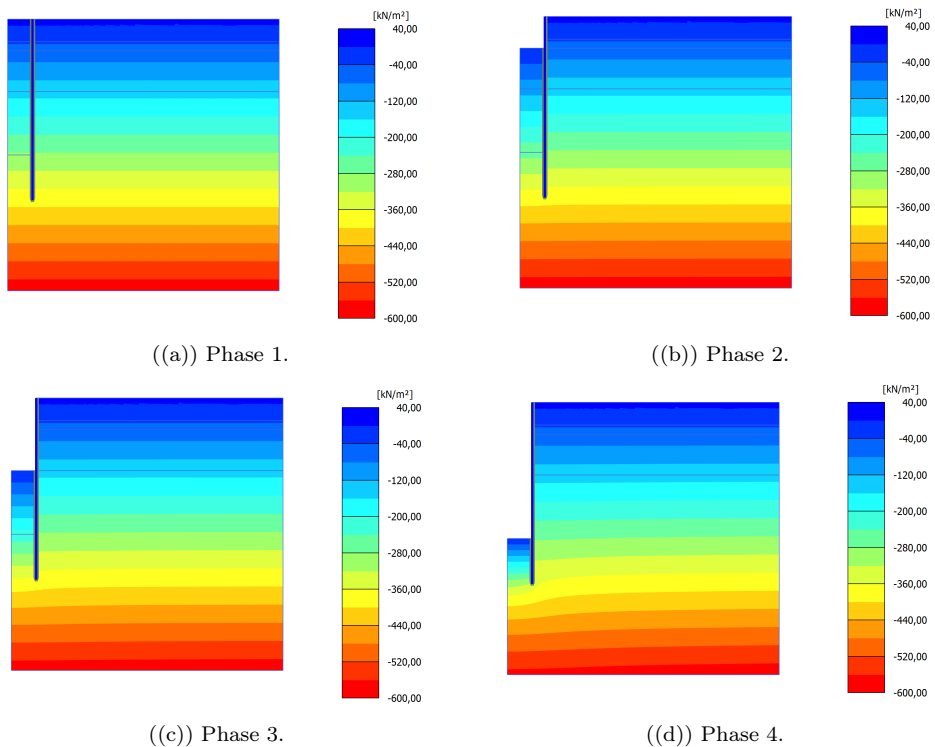

((a)) Phase 1.

((b)) Phase 2.

((c)) Phase 3.

((d)) Phase 4.

Figure 9.3: Pore water presure in different excavation phases.

To be able to effectively compare the results from 2D-modelling, 3D-modelling and analytical calculations, the lateral earth pressure against the retaining structure and the hoop forces in the structure are compared. In PLAXIS 2D, the lateral earth pressure is studied by creating a vertical cross-section just beside the retaining wall in the output program. The lateral earth pressure normal to the cross-section is obtained and plotted against the depth. The hoop forces acting in the structure can be directly obtained in the axisymmetric model and are also plotted with depth. The plots are presented in Figure 9.4, where the lateral pressure and hoop forces are plotted to the excavation depth. The pressure below excavation bottom is not taken up by the structure and is therefore not plotted.
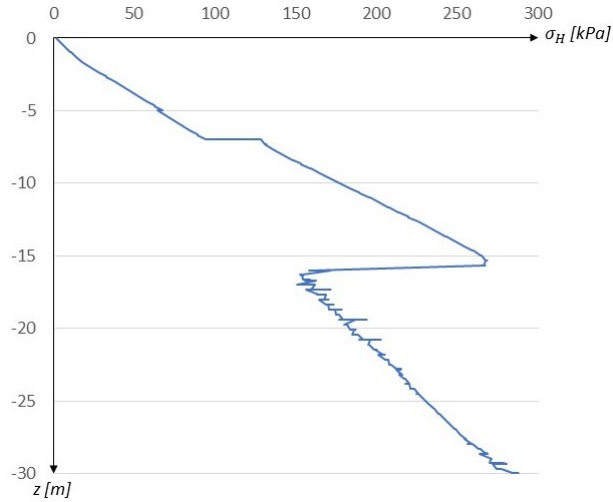
((a)) Variation of lateral pressure with depth on retaining wall.
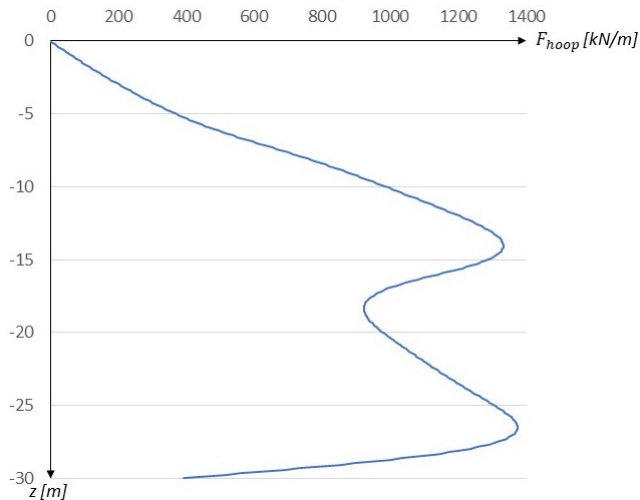
((b)) Variation of hoop forces with depth in retaining wall.

Figure 9.4: Lateral pressure and hoop forces from PLAXIS 2D.

As can be seen in Figure 9.4(a) above, the lateral pressure against the retaining wall decreases significantly at $z \approx -16$ m, which coincides with the depth of the limestone. This reduction

in pressure is also visible in Figure 9.4(b), where the hoop forces start to decline when the limestone approaches. Figure 9.4(b) also has a smoother distribution of hoop forces over depth than is shown in Figure 9.4(a). This can be explained from plate action in the wall. The wall distributes the pressure from the soil, giving a smoother curve for the hoop forces and also gives a slight 'delay' in conformity between the two graphs.

9.3.2 Analysis of the soil-structure interaction in PLAXIS 3D

The model in PLAXIS 3D is created through the same procedure as in the 2D-model, forming a shaft with a diameter of 11 m. Six different calculation phases are defined and the groundwater level has the same gradual lowering inside the shaft. The methodology for groundwater lowering differs in PLAXIS 3D however. By defining the soil clusters inside the shaft as either *dry, head, interpolate* or *global*, the gradual lowering can be modelled correctly in PLAXIS 3D. The *global* mode means that the pore water pressure is calculated from the global level defined in the geo-model, see Figure 7.2. *Dry* simply means the pore pressure is removed and *interpolate* means the pressure is linearly interpolated from the overlying cluster. *Head* means the pore water pressure is generated by defining the head at the top of the specific cluster (Plaxis n.d.[b]). Table 9.2 below defines the soil clusters and which groundwater mode they are associated with in each calculation phase in PLAXIS 3D. Note that the clusters are only defined with depth but are actually also limited in width as the groundwater lowering is only present inside the shaft. All remaining clusters, meaning the soil outside the shaft and below excavation bottom, is given the *global* mode.

Table 9.2: Excavation clusters with associated groundwater modes in each calculation phase in PLAXIS 3D.

Soil cluster	Phase 1	Phase 2	Phase 3	Phase 4	Phase 5
Fill z = 0 to -5 m	Global	Dry	Dry	Dry	Dry
Sand z = -5 to -7 m	Global	Head	Dry	Dry	Dry
Clay till z = -7 to -16 m	Global	Interpolate	Head	Dry	Dry
Limestone z = -16 to -30 m	Global	Interpolate	Interpolate	Head	Dry

The mesh is generated by the standard element distribution option 'fine'. The plate elements and soil elements inside the excavation are however given a finer distribution by assigning a coarseness factor of 0.1. Figure 9.5 below shows a 3D view of the undeformed and deformed mesh, where the deformations in Figure 9.5(b) are exaggerated $5 \cdot 10^3$ times.

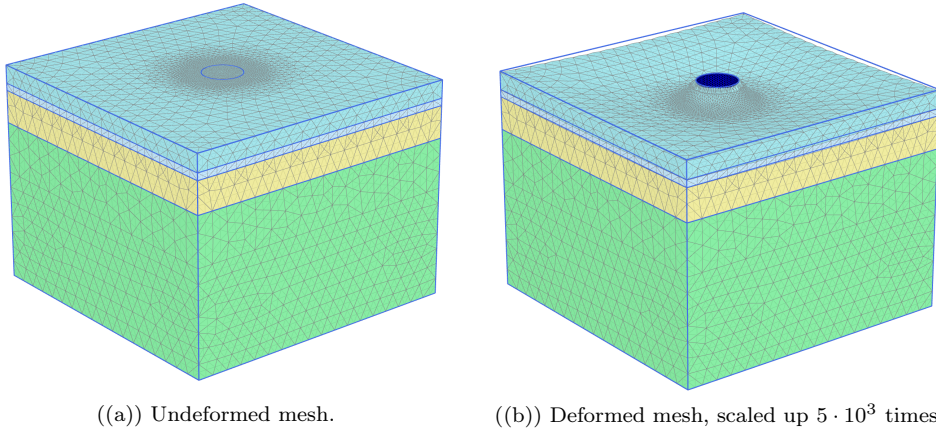((a)) Undeformed mesh. ((b)) Deformed mesh, scaled up $5 \cdot 10^3$ times.

Figure 9.5: Undeformed and deformed mesh.

The obtained deformations in the retaining structure are shown in Figure 9.6. It is shown that the largest deformations occur in the areas with the highest radial pressure and the deformations are significantly lower in the top of the shaft as well as in the structure below excavation bottom.
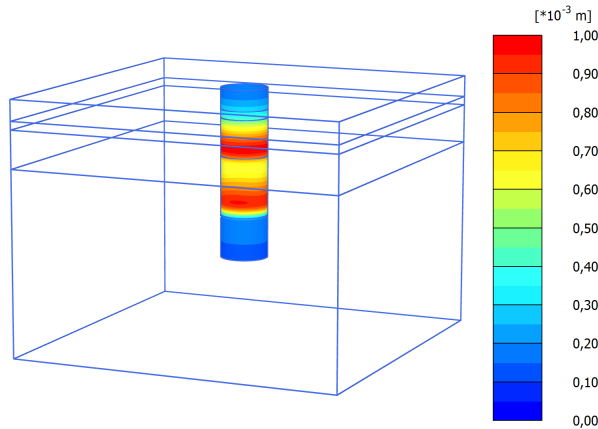

Figure 9.6: 3D-view of total deformation, $|u|$, in retaining structure.

The deformations are overall small in the retaining structure, which is expected with a circular shaft, meaning the arching effect is largely present. The biggest total deformation $|u|$, which is the total accumulated displacements comprising the individual components in u_x, u_y and u_z, in the retaining wall is obtained as $|u|_{max} = 0.98$ mm and occurs at a depth of $z = -14$ m. The radial displacements in the wall are also plotted with depth and presented in Figure 9.7.
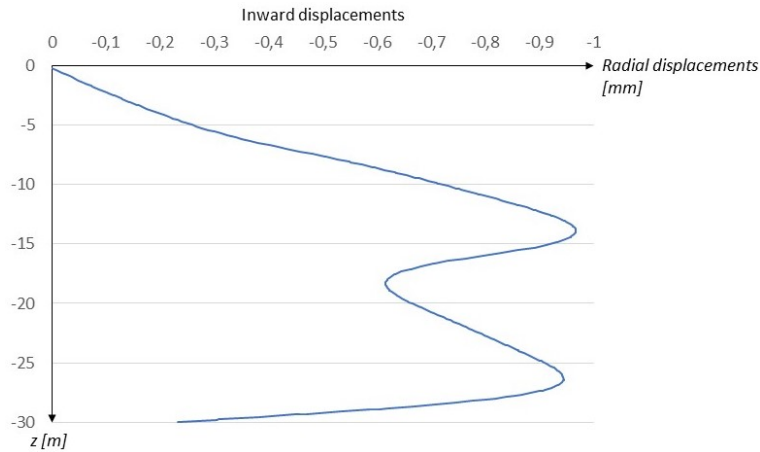
Figure 9.7: Radial displacements, u_x, in retaining wall plotted with depth. Negative values indicates inward displacements.

The results from the final phase of calculation makes it possible to plot the radial pressure from soil and water against the shaft. In 3D, the data is obtained by first creating a plane section that tangents the retaining wall on one side. By creating a line section within the plane section, the lateral earth and water pressure against the wall can be obtained and plotted with depth. The hoop forces in the structure can be obtained directly from PLAXIS. Both the radial pressure and hoop forces are plotted with depth in Figure 9.8.
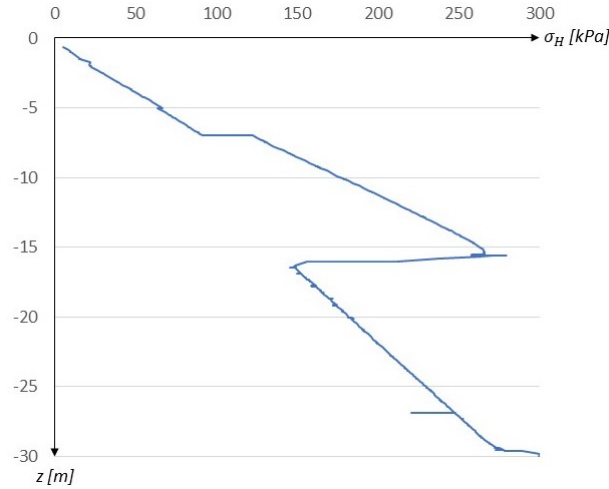
((a)) Variation of lateral pressure with depth on retaining wall.
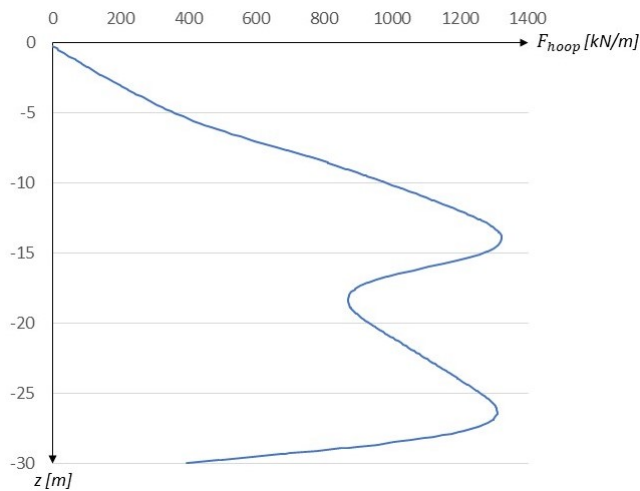
((b)) Variation of hoop forces with depth in retaining wall.

Figure 9.8: Lateral pressure and hoop forces from PLAXIS 3D.

Figure 9.8(a) follow the same principle as the curve from the 2D-model, where the radial pressure decreases in the limestone. This in turn gives the shape of the curve in Figure 9.8(b), where the hoop forces have a smoother distribution over depth and have it's biggest values just before the maximum pressure occurs. It can also be seen that at a depth of $z = -30$ m, the radial pressure rises drastically but the hoop forces decrease. This is explained from the fact that below $z = -30$ m there is limestone on both sides of the retaining wall, which means the pressure is then taken up by the soil itself and not giving rise to hoop forces in the wall.

9.3.3 Simplified analysis of structure in Robot 3D

A simplified model is created with Robot by creating a circle with the radius 5.5 m consisting of 0.8 m thick shell elements which are extruded 1 m. The material is defined as concrete C35/45 with the parameters given in Table 7.2 and Equation (7.2) with no reinforcement. The reinfor-

cing of the concrete is considered to not affect the corresponding hoop stresses for the circular shaft. A mesh is created with a coarseness factor of 0.1. The boundaries on the upper and lower edge of the structure is prohibited to deform in the vertical direction along the z-axis. An arbitrary node is fixed in all directions except from movement along the z-axis to prevent rigid body motion of the structure.

Radial uniform loads ranging from 37-264 kPa are applied as an hydrostatic load around the whole structure. The load symbolises the average lateral earth pressure at different levels from the ground surface obtained from PLAXIS 3D. Figure 9.9 shows the configuration of the model in Robot.
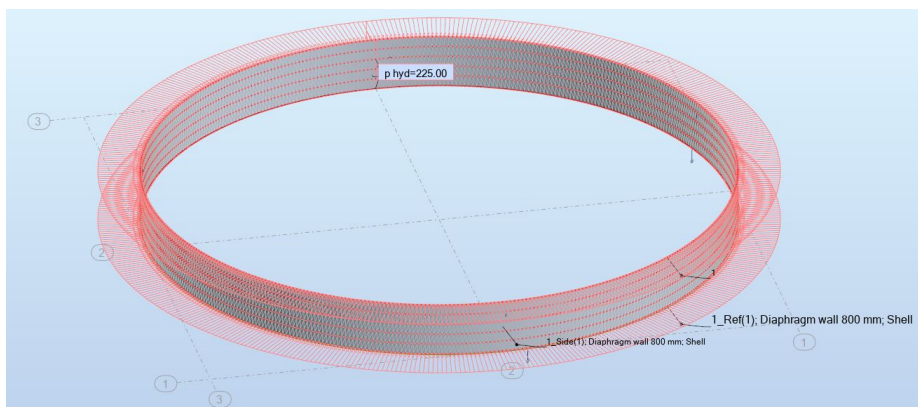

Figure 9.9: Model in Robot

The resulting hoop forces in the structure corresponding from the applied loads are obtained and shown in Table 9.3.

Table 9.3: Lateral earth pressure and corresponding hoop forces.

Level [m]	Lateral earth pressure [kPa]	Hoop force [kN]
-3	37	204
-6	73	402
-9	158	869
-12	213	1172
-15	264	1453
-18	164	903
-21	191	1051
-24	220	1210
-27	248	1364

The hoop force is constant in every section of the structure and no bending moments are present.

9.3.4 Analytical analysis

The analytical approach is based on Rankine's equations, presented in Section 3.3. The circular shape of the shaft entails small deformations and therefore it is assumed that the earth pressure should remain in the at-rest state. But the direction of the deformations of the soil in relation to the retaining structure that will occur indicates that an active pressure possibly could develop, if the structure deforms inwards enough. The active lateral earth pressure is consequently also calculated. As there is no possibility for a passive pressure to develop, the at-rest pressure is considered the upper limit and the active pressure considered the lower limit of the actual lateral earth pressure on the structure.

The lateral earth pressure at-rest σ_H on the retaining wall is obtained with Equation (3.3), discussed in Section 3.1.3, by multiplying the effective vertical stress σ'_V with the at-rest earth pressure coefficient K_0 and adding the pore water pressure u_W.

$$\sigma_H = K_0 \sigma'_V + u_W \tag{9.3}$$

K_0 is calculated with Equation (3.5) if the soil is normally consolidated, otherwise with Equation (3.6) if the soil is overconsolidated. σ'_V is calculated by first calculating the vertical stress σ_V with Equation (2.21) and then subtracting the pore pressure u_W calculated with Equation (2.24).

By using the geotechnical data presented in Table 7.1 together with the soil profile presented in Figure 7.2, the variation of the lateral earth pressure at-rest along the depth of the wall is obtained and presented in Table 9.4.

Table 9.4: Lateral at-rest pressure.

Level [m]	Material	γ/γ_s [kN/m^3]	σ_V [kPa]	p_W [kPa]	σ'_V [kPa]	σ_H [kPa]
-5	Fill/clay	20/20	100	35	65	68
-5	Sand	18/20	100	35	65	65
-7	Sand	20/20	140	55	85	94
-7	Clay till	22/22	140	55	85	94
-16	Clay till	22/22	352	145	207	314
-16	Limestone	24/24	352	145	207	290
-30	Limestone	24/24	720	285	435	590

The active lateral earth pressure is calculated by using Equation (3.33), according to Rankine's earth pressure theory including Bell's modification, presented in Section 3.3.1. The lateral earth pressure is presented in Table 9.5.

Table 9.5: Active lateral pressure.

Level [m]	Material	K_a [-]	σ_H [kPa]
-5	Fill/clay	0.33	57
-5	Sand	0.29	54
-7	Sand	0.29	58
-7	Clay till	0.28	58
-16	Clay till	0.28	97
-16	Limestone	0.17	98
-30	Limestone	0.17	277

The corresponding hoop stresses are calculated according to the theory presented in Section 4.4.1. The requirement for thick walls, the thickness of the retaining wall being more than 1/10 of the shafts radius, is for this example fulfilled. The hoop stress can therefore not be assumed to be uniform throughout the thickness of the wall and the maximum value of the hoop stress appears on the inner surface of the wall. According to the equation for the hoop stresses, the distribution of the stresses is almost linear over the thickness of the wall. This means that the average hoop stress could be assumed to appear in the middle of the wall thickness. Figure 9.10 shows the geometry of the circular retaining structure where r_i=5.5 m, r_o=6.3 m and t_{dw}=0.8 m.
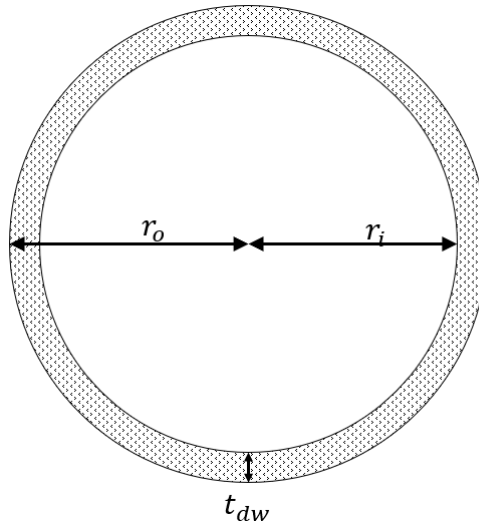

Figure 9.10: Geometry of the circular retaining structure.

From the geometry parameters, the average hoop stresses are calculated with Equation (4.4) from Section 4.4.1, this is a linear function of the lateral pressure. The representative hoop forces are obtained by multiplying the average hoop stress with the thickness of the wall. The resulting average hoop stresses and the corresponding hoop forces are presented in Table 9.6.

Table 9.6: Average hoop stresses and representative hoop force

Level [m]	Material	At-rest		Active	
		σ_{hoop}[kPa]	F_{hoop} [kN]	σ_{hoop}[kPa]	F_{hoop} [kN]
-5	Fill/clay	530	424	445	356
-5	Sand	507	406	426	340
-7	Sand	736	589	458	367
-7	Clay till	976	781	453	363
-16	Clay till	2465	1972	764	611
-16	Limestone	2278	1822	768	614
-30	Limestone	4632	3706	2175	1740

The hoop forces in the retaining structure corresponding to the at-rest pressure are considered the upper limit and forces from the active pressure are considered the lower limit of the actual hoop forces.

The pressure and corresponding hoop forces from both the the at-rest and active state are plotted with depth in Figure 9.11 below.
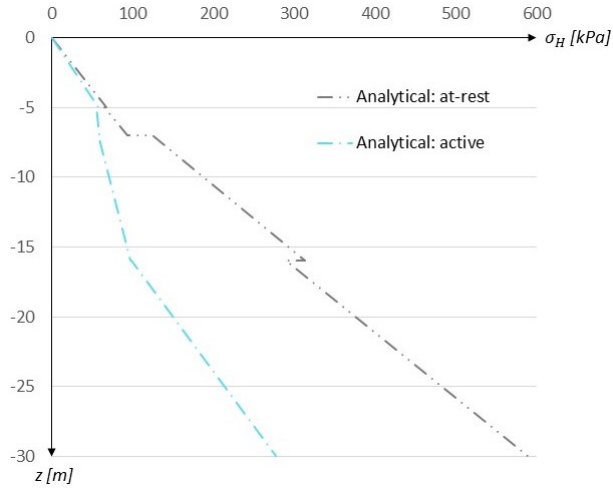
((a)) Variation of lateral earth pressure, in both at-rest and active pressure state.
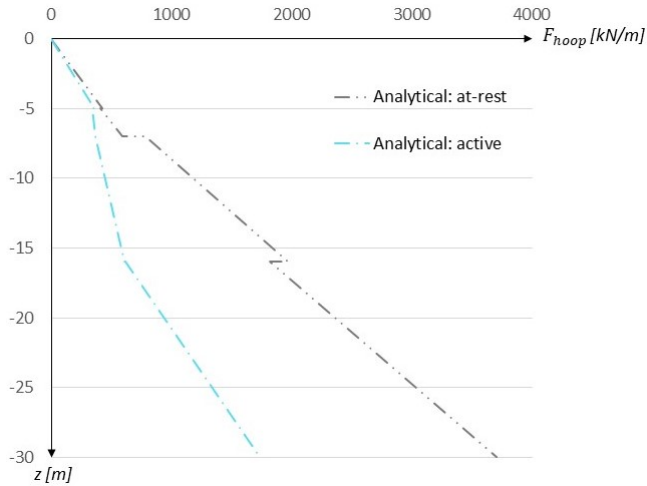

((b)) Corresponding variation of hoop forces in retaining wall.

Figure 9.11: Lateral earth pressures and corresponding hoop forces from analytical method.

9.3.5   Comparison of results and discussion

To verify the model in PLAXIS 3D and thereafter continue to study the elliptical shaft, the results for the circular shaft from PLAXIS 2D, PLAXIS 3D and the analytical method are compared. The obtained lateral pressure acting on the wall from each method has been plotted in previous chapters. In the analytical approach, the at-rest pressure and active pressure were calculated and viewed upon as upper and lower limit pressures. In Figure 9.12, the lateral pressures on the retaining wall from all models are plotted and compared to each other.
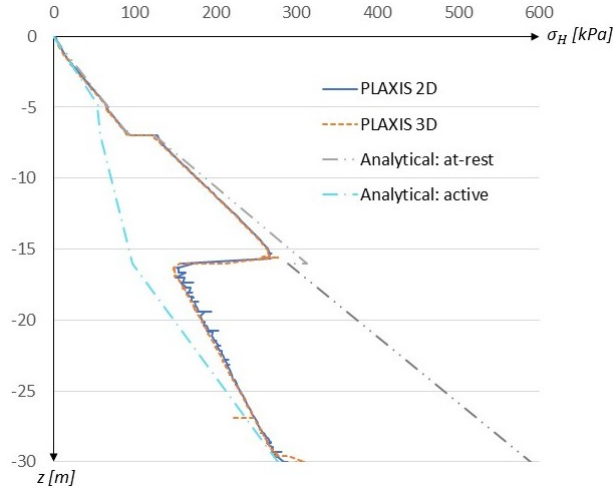
((a)) Variation of lateral earth pressure with depth on retaining wall.
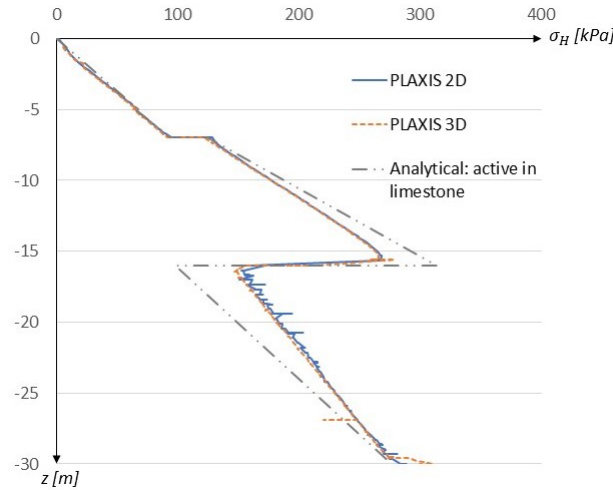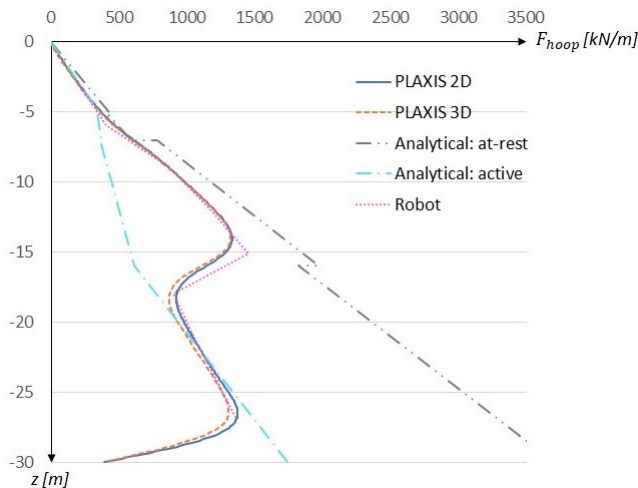

((b)) Variation of lateral earth pressure with depth on retaining wall, assuming active pressure in the limestone in the analytical method.

Figure 9.12: Lateral pressure on retaining wall obtained from PLAXIS 2D, PLAXIS 3D and analytical method.

When studying the above graphs, it can be seen that the results from PLAXIS 2D and 3D are rather similar and that the obtained pressures are given to be within the limits represented by the analytical pressures in Figure 9.12(a). The results from PLAXIS also show that there is a clear drop in pressure when reaching the limestone, at $z = -16$ m. Before this drop the pressure is closer to the upper limit pressure (at-rest) and after the drop is is closer the lower limit (active). From this, it seems as though the lateral earth pressure becomes active in the limestone. This assumption is plotted in Figure 9.12(b), which shows that the results from all three approaches becomes rather conforming when having at-rest pressure above the limestone and active pressure in the limestone. As the hoop forces arise from the lateral pressure, the same pattern can be

seen when plotting the obtained hoop force from each method, see Figure 9.13. Here, also the obtained hoop forces from Robot are presented, which shows that the simplified approach with Robot gives a good estimation of the hoop forces in the circular structure.

((a)) Variation of hoop forces with depth in retaining wall.
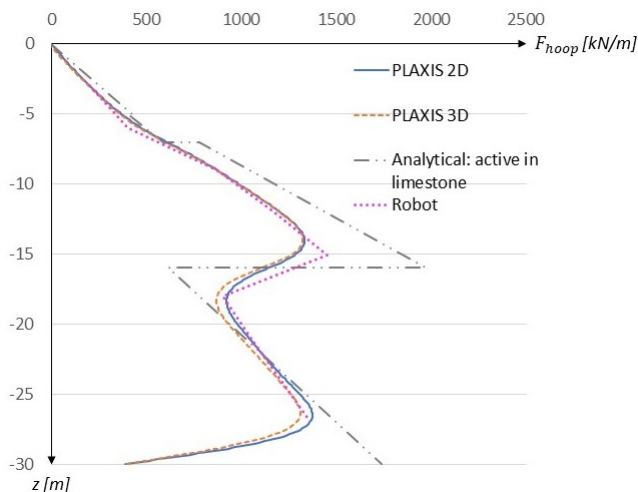
((b)) Variation of hoop forces with depth in retaining wall, assuming active pressure in the limestone in the analytical method.

Figure 9.13: Hoop forces in retaining wall obtained from PLAXIS 2D, PLAXIS 3D, Robot and analytical method.

By assuming active pressure in the limestone, it can be seen that the analytical results are rather similar to the FE-results. These results are unexpected for such a stiff structure with only small obtained displacements. The maximal displacement in the wall from both the 2D- and 3D-analysis is obtained as approximately 1 mm. With this magnitude of displacements, active pressure is normally not achieved. In a dense sand, for example, Craig and Knappett (2012) states that experimental results show that movements of about 0.25 % of the embedded wall

depth is required to mobilise active pressure. This would indicate that active pressure is not present in this case. However, the characteristics of limestone differs a lot from that of sand. The limestone in this design example is given a Young's modulus of $E' = 5000$ MPa, which is rather high. Referring to Hooke's law (Equation (6.1)), a high modulus of elasticity could give large stress changes even though the deformations are small. Rajagopal (n.d.) states that several factors, such as c' and ϕ', influence the mobilisation of active pressure on a retaining wall. But he also shows that a very high Young's modulus can give large stress changes even with small deformations. He proves this by comparing two different soils with $E = 25$ MPa and $E = 50$ MPa respectively, where the both soils develop the same deformation. The result shows that the soil with higher modulus of elasticity undergoes larger stress changes for the same amount of deformation.

By altering the modulus of elasticity in the limestone and comparing the results from PLAXIS 2D, the lateral pressure on the wall can be compared with the pressure from the analytical approach assuming at-rest pressure. The results are plotted in Figure 9.14.
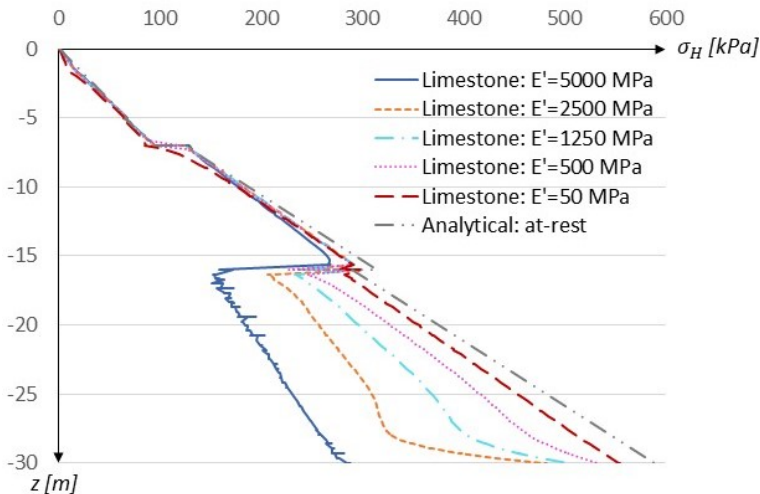

Figure 9.14: Lateral pressure on retaining wall obtained from PLAXIS 2D with different modulus of elasticity in limestone compared to lateral pressure according to analytical approach assuming at-rest pressure.

Figure 9.14 shows that Young's modulus has a large impact on the lateral earth pressure in the limestone. It can be seen that when the modulus is lowered, the result from PLAXIS approaches the analytical result. From this it can be verified that the rapid decrease in lateral earth pressure in the limestone obtained in PLAXIS is related to Young's modulus and that active pressure is probably obtained even though the displacements are small. The active pressure is believed to mobilise because of the very high modulus of elasticity present in the limestone. Apart from the modulus of elasticity, the cohesion (c') is rather high in the limestone when compared to the other materials in the geo-model. When conducting the same analysis for the cohesion as was made for the modulus of elasticity presented in Figure 9.14, the results are less striking. Meaning, the cohesion does not seem to have any vital impact on the lateral pressure in PLAXIS. It is therefore concluded that the most important material factor in this design example is the modulus of elasticity.

It can also be proven that the decrease in lateral earth pressure in the limestone is directly related to the deformation of the retaining wall. By plotting the horizontal pressure in the soil 15 m away from the wall, it can be seen that the pressure does not decrease in same way as right next to the wall. In Figure 9.15, the lateral pressure acting on the wall from PLAXIS and the analytical result assuming at-rest pressure is plotted together with the horizontal pressure 15 m away from the wall.
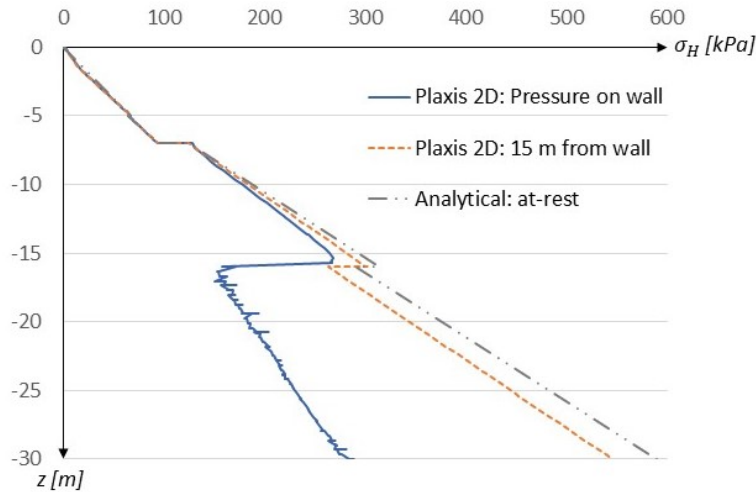

Figure 9.15: Lateral earth pressure on retaining wall from PLAXIS 2D and analytical results assuming at-rest pressure together with the horizontal pressure from PLAXIS 15 m away.

The graph in Figure 9.15 backs up the theory of active pressure in the limestone as the pressure drop seems to be directly related to the wall displacements. Based on the above arguments and results, the PLAXIS model is considered to be verified. Meaning, the PLAXIS 3D model can be used to study elliptical shafts. It can also be concluded that the forces in the circular structure can be studied by using the simplified approach adopted in Robot.

9.4   Analysis of elliptical shafts

The elliptically shaped shaft is now to be studied. The model in PLAXIS 3D is considered to be verified and the geometry will gradually be modified into a more elliptic shape. The simplified method in Robot also proved to give conforming results for the circular geometry, meaning this method will also be implemented for the elliptical structure.

The elliptical geometry is based on the relation A/B as depicted below. Pressures and forces will later be extracted and referred to as acting on 'long side' and 'short side', see Figure 9.16.
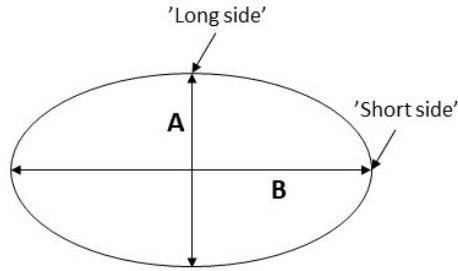
Figure 9.16: Geometry of ellipse.

By studying different geometries it is possible to analyse how the shape affects the forces in the retaining structure. The aim of this analysis is to find some general recommendation, given the geological conditions in the design example, of the optimal ratio A/B. Before performing advanced analyses with PLAXIS 3D, a simplified analysis of an elliptical shape is performed in Robot. The results obtained from Robot are thereafter compared to the results from the advanced analysis in PLAXIS, in order to determine the utility of the simplified method.

The optimal ratio A/B is found by comparing the reaction forces and bending moments with the capacity of the retaining structure. Normal compression forces in combination with bending moments requires evaluation of the second-order effects in the structure. The second-order effects are dependent on the buckling length which is difficult to evaluate for elliptically shaped shafts. The interaction with the soil could also counteract the second order effects. The second-order effects can not be calculated with PLAXIS. The structural analysis software Robot provides the opportunity to perform second-order analyses. However, the second-order effects will not be analysed in this thesis.

9.4.1 Simplified analysis of structure in Robot 3D

The simplified model of the elliptically shaped structure is created with polygon curves in Robot. The polygon curves are segments of circles with different radii, which combines into forming an elliptical shape. Consequently, the model is not a perfect ellipse but is considered sufficiently precise. The polygon curves are created by specifying the coordinates in the x- and y-plane for three points of each polygon curve. The coordinates of the points are selected to fulfill the equation of an ellipse

$$1 = \frac{x^2}{(A/2)^2} + \frac{y^2}{(B/2)^2} \tag{9.4}$$

where A and B are the ellipse two diameters depicted in Figure 9.16.

The polygon curves are extruded to create a 1 m high beam and assigned the material concrete C35 with the parameters given in Table 7.2 and Equation (7.2) and the thickness 0.8 m. No reinforcement is applied. The same boundary conditions are applied for the elliptic structure as for the circular. For the case of simplicity, only one elliptic shape is studied with the simplified analysis in Robot. The ellipse is defined with $A = 7$ m and $B = 11$ m, this shape is later referred to as Ellipse 2. Loads are applied as hydrostatic loads around the whole structure representing the average lateral earth pressure at different depths. The same loads as in the circular Robot-model are applied in this model, giving loads in the span of 37-264 kPa.
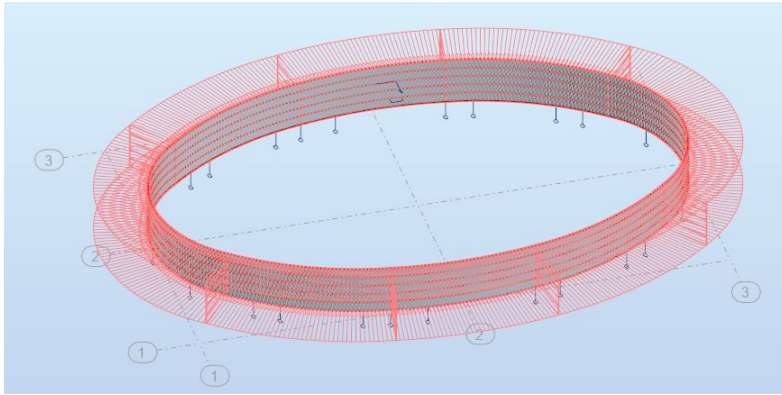
Figure 9.17: Elliptical model in Robot.

The obtained hoop forces corresponding from the applied loads at different depths are extracted and plotted in Figure 9.18. As the elliptical shape entails a non-uniform curvature, the hoop forces will not be the same in every cross-section of the structure. The forces are therefore extracted in two different sections, here called 'long side' and 'short side', see Figure 9.16.
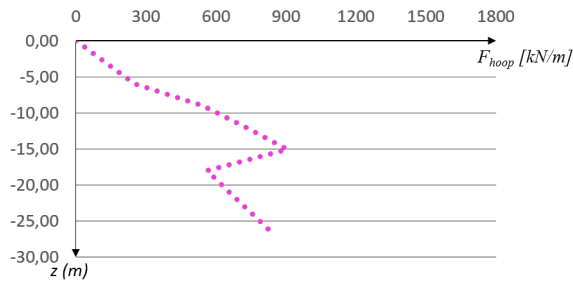

((a)) Hoop forces on long side.
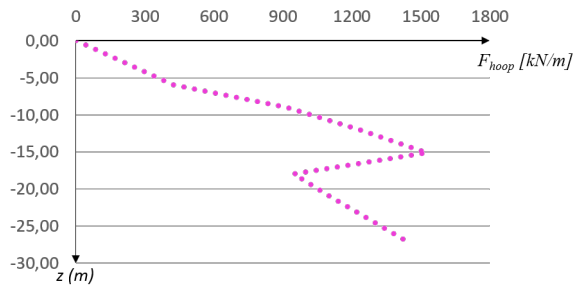
((b)) Hoop forces on short side.

Figure 9.18: Hoop forces in retaining wall obtained from Robot.

The obtained bending moments are also extracted and plotted. This simplified structure only captures the horizontal bending moment M_{22} (bending around a vertical axis). However, in reality there will also be a vertical bending moment in the structure.
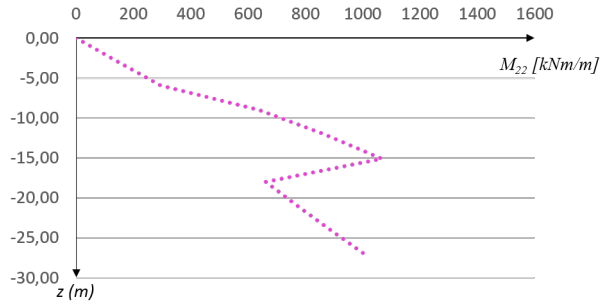
((a)) Bending moment on long side.
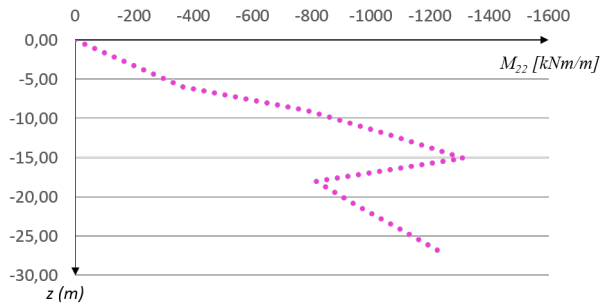
((b)) Bending moment on short side.

Figure 9.19: Bending moments in retaining wall obtained from Robot.

9.4.2 Parametric study on shaft dimensions in PLAXIS 3D

The parametric study of the ratio A/B in PLAXIS starts out with three different geometries, which are presented in Table 9.7 below. Note that the geometry used in Robot corresponds to Ellipse 2. Elliptical geometries in PLAXIS are created by polycurve segments. The easiest way of drawing these ellipses were therefore to use Autocad. In Autocad there is a standard function for creating a perfect ellipse, by using this function and thereafter imitate the shape through polycurve segments, it is possible to extract the segmental data and use as input in PLAXIS. Each segment is defined with *Radius* and *Segment angle*.

Table 9.7: Elliptical geometries.

Geometry	A [m]	B [m]	Ratio
Ellipse 1	9	11	0.82
Ellipse 2	7	11	0.64
Ellipse 3	5	11	0.45

The elliptical shape entails a more complex composition of forces in the retaining structure. Referring to Figure 4.8 in Section 4.5, it is expected to obtain an inward movement of the wall along the long axis of the ellipse and an outward movement along the short axis. Because of these expected deformations, the lateral earth pressure acting on the long side of the shaft and the lateral earth pressure acting on the short side of the shaft, will not be the same. This can be seen in Figure 9.20, where the lateral earth pressure onto the two different sides of the retaining wall is plotted with depth for Ellipse 1.
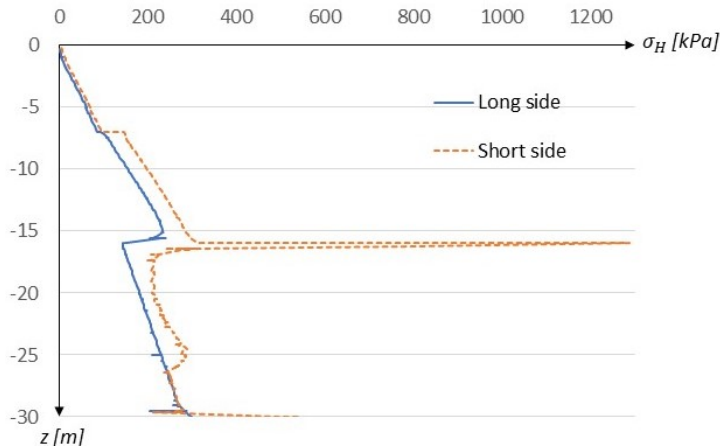
Figure 9.20: Earth pressure on retaining wall for Ellipse 1.

It can be seen that the pressure is generally higher against the short side of the shaft. This can be explained from the directions of the displacements. On the long side, the inward movement causes the pressure to decrease and the graph also follows the familiar pattern from the circular shaft, where the limestone seems to give active pressure. On the short side, there is instead an outward movement of the wall and the pressure increases in the limestone. The large increase of pressure in the limestone can probably be explained from its high stiffness, causing pressure to build up between the wall and the limestone. The spike in pressure, obtained right at the border of the limestone, shows how the stiff limestone 'pushes back' the outward deformations. This 'pushing back'-effect is clearly visible when plotting the displacements with depth. In Figure 9.21, the displacements on both the long and the short side of Ellipse 1 are plotted with depth. Positive displacements indicates outward movement of the wall and negative displacements indicates inward movement.
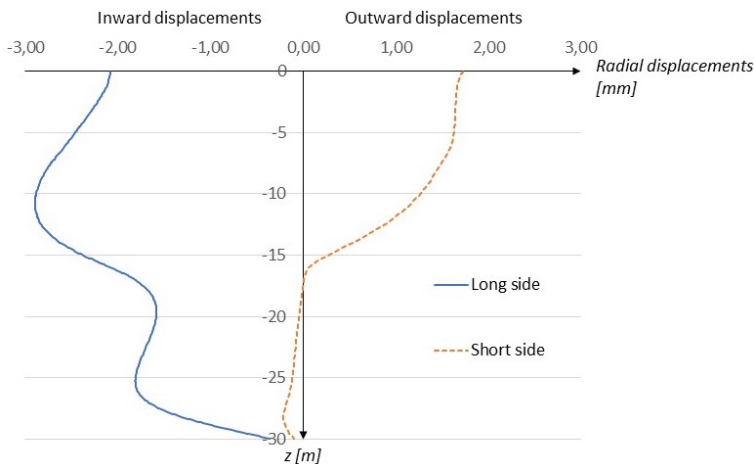

Figure 9.21: Wall displacements of Ellipse 1. Negative values indicates inward displacements and positive values indicate outward displacements.

Examining the displacements on the short side of the shaft in Figure 9.21, is can be seen that the

displacements are bigger before reaching the limestone. Meaning, the stiff limestone pushes back the deformations, causing higher pressure on the wall and thereby creating a spike in Figure 9.20. Below the spike in Figure 9.20, the pressure remains rather high. This is interpreted as the wall still wanting to deform outwards, but is held back by the limestone and thereby creating high pressures. The limestone being able to hold back the outward movement is visible also in Figure 9.21, where the wall actually seems to be moving slightly inwards also on the short side in the limestone. On the long side, the wall deforms inwards as expected. It can also be observed that the displacements (Figure 9.21) follows the shape of the pressure-curve in Figure 9.20, giving lower displacements in the limestone where the pressure is lower.

The radial displacements on both the long and the short side of each elliptic geometry are plotted in Figure 9.22 and 9.23. The displacements are in general higher on the long side. Outward displacements relates to passive pressure in the soil, meaning very high pressures are required to give outward deformation. The inward displacements on the long side are instead related to active pressure in the soil, which can be achieved with lower pressure.
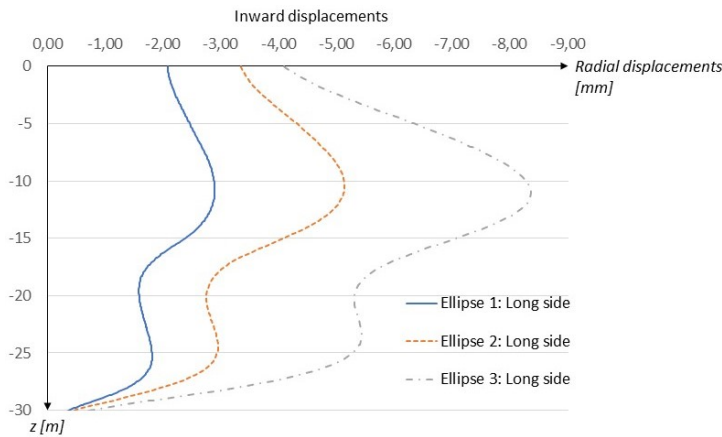

Figure 9.22: Wall displacements on long side. Notice the negative values indicating inward displacement.
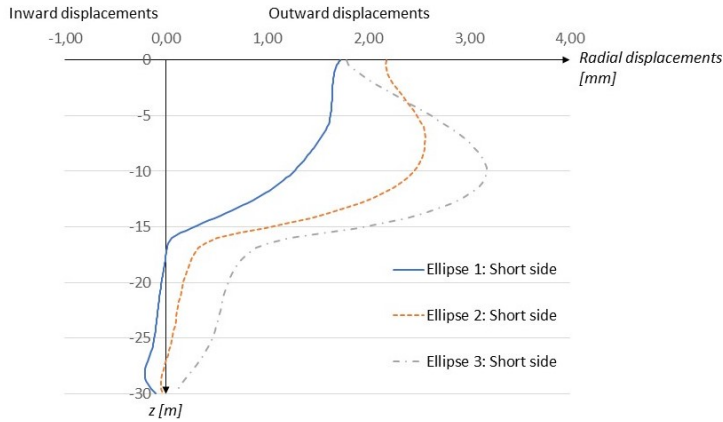
Figure 9.23: Wall displacements on short side. Notice the positive values indicating outward displacement.

In Figure 9.24, the lateral earth pressure on the long side of the shaft is compared between the different geometries presented in Table 9.7. The lateral earth pressure on the long side of each geometry looks to be rather similar. It would be expected to see a decrease in pressure when lowering the diameter A, and thereby lowering the ratio A/B, as the inward displacements should become higher. When examining Figure 9.24 in more detail, it can be seen that the pressure above the limestone (above $z = -16$ m) is in fact decreasing for each step of lowered diameter A. This is consistent with the theory and also follows the displacement-plot in Figure 9.21.
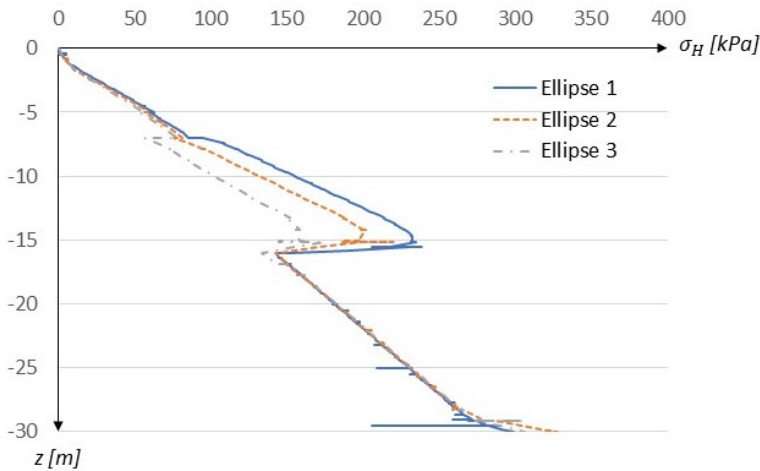
Figure 9.24: Lateral pressure on long side of Ellipse 1, Ellipse 2 and Ellipse 3.

The earth pressure acting on the short side of the shaft is plotted in Figure 9.25. The spike in pressure is clearly visible and seems to get higher when the diameter A is lowered. This trend is expected as the more elongated the shaft gets, the more it will try to deform. The more it tries to deform, the higher pressure the limestone needs to hold back, which creates a higher spike.
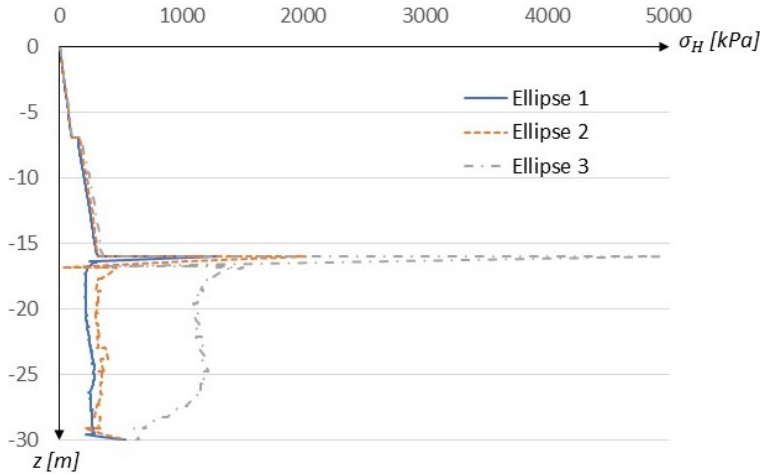
Figure 9.25: Lateral earth pressure on short side of Ellipse 1, Ellipse 2 and Ellipse 3.

The earth pressure before the spike looks to be similar for all three shapes. However, by zooming in on the area above the spike in Figure 9.25, it can be seen that there is some difference between the obtained pressures, see Figure 9.26. The trend follows the expected result of a more elongated geometry experiencing higher pressure on the short side.
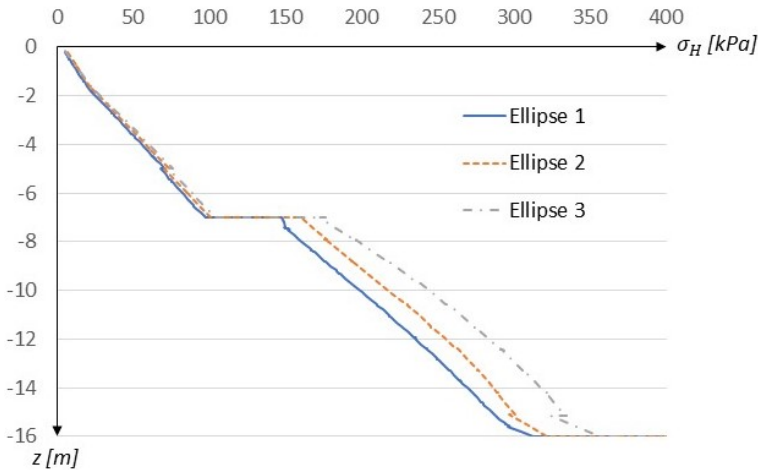

Figure 9.26: Zoomed in lateral earth pressure on short side of Ellipse 1, Ellipse 2 and Ellipse 3.

The obtained hoop forces from each geometry are plotted with depth in Figure 9.27. The hoop forces remain being rather high in the structure. On the long side above the limestone, the hoop forces are lower in the more elongated geometries. This is expected as a more elongated shape gives less curvature on the long side. When looking at Figure 9.27(a), the hoop forces below $z = -16$ m (in the limestone layer) are instead higher the more elongated the shape gets. This behaviour is unexpected but could possibly be explained by looking at Figure 9.21, where the inward displacements on the long side decrease in the limestone. Lower displacements make it more difficult for the bending moment to build up in the wall, and therefore a higher amount of the lateral pressure acting onto the wall gives rise to hoop forces. This explanation is more

understandable when also examining the moment-plots, see Figure 9.29-9.30. The hoop forces on the short side are plotted in Figure 9.27(b). At $z = -16$ m, the pressure spike, seen in Figure 9.25, results in a spike of hoop forces in the structure as well. The results are in general rather consistent with the pressures obtained in Figure 9.25.
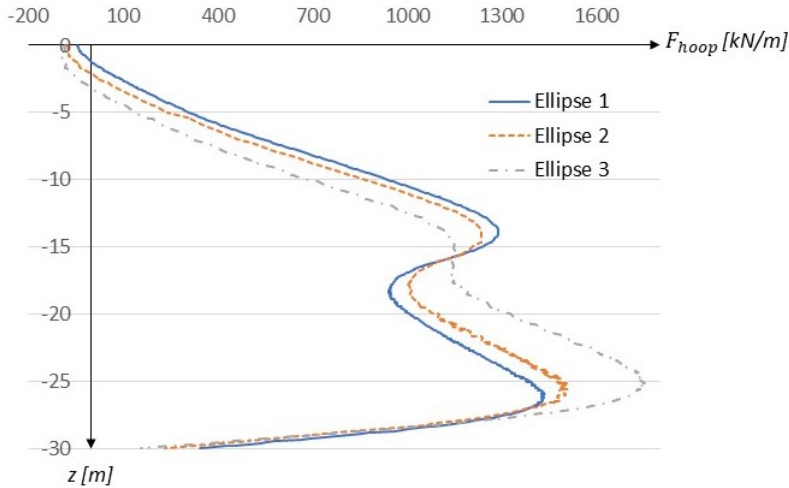
((a)) Hoop forces on long side.
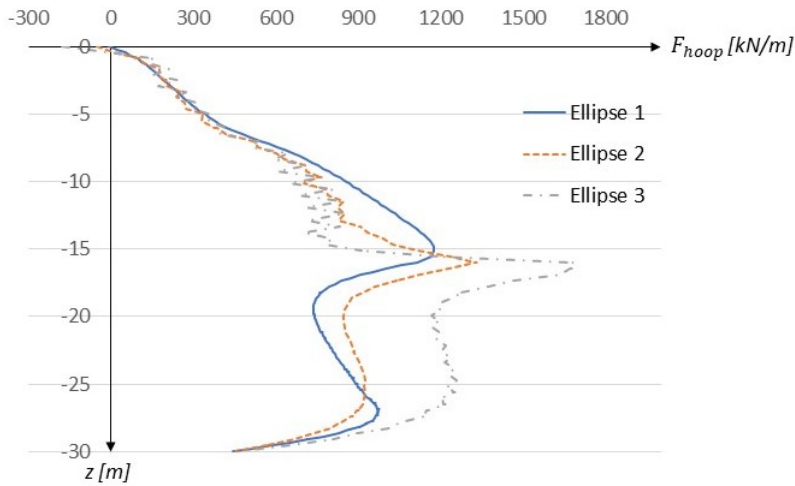
((b)) Hoop forces on short side.

Figure 9.27: Variation of hoop forces with depth on long and short side.

It should also be noticed that tension forces appears at the top of the structure, seen as negative hoop forces in Figure 9.27. This is interpreted as a 3D-effect in the wall elements, where the top regions of the wall experience minimal soil pressure, and the lower regions experience high soil pressure.

The retaining structure needs to withstand several types of forces. Concrete is good at taking up pressure, but rather weak when experiencing tension forces. Reinforcement cages in the wall

panels will strengthen the wall and increase it's tension capacity. The elliptical shape gives rise to bending moments, which cause tension in the cross-section. Due to the 3D environment, moments will appear in the wall as bending moments in two directions together with torsional moment. PLAXIS 3D defines the directions of the moments in plates as depicted in Figure 9.28 below, where $M_{12} = M_{torsion}$.
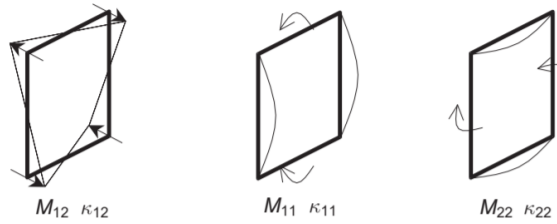
Figure 9.28: Definition of moments in PLAXIS 3D (Plaxis n.d.[b]).

According to theory, presented in Section 4.5.1, the horizontal moment (M_{22}) should the dominant moment in the structure. The horizontal and vertical moment, on both the long and the short side, are plotted with depth for each geometry in Figure 9.29 and 9.30.
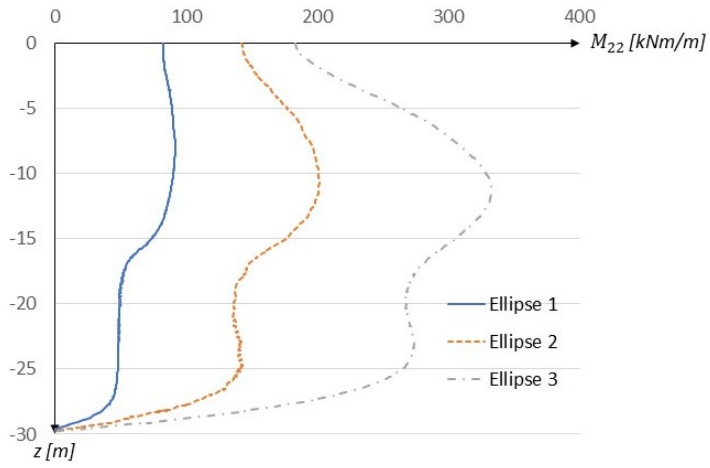
((a)) Horizontal moment on long side.
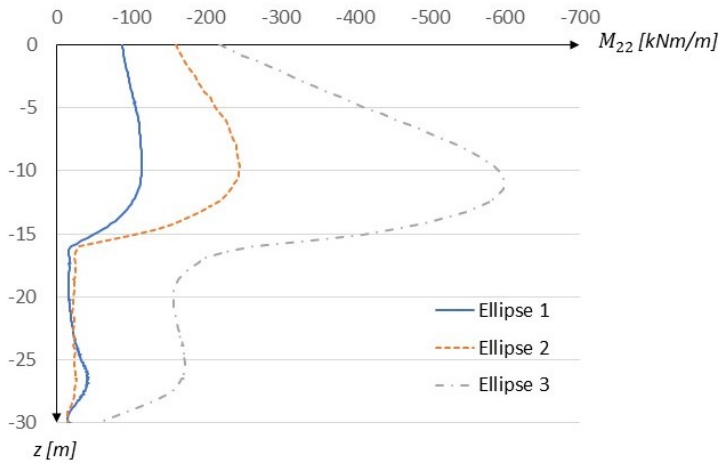
((b)) Horizontal moment on short side.

Figure 9.29: Variation of horizontal moment with depth on long and short side.
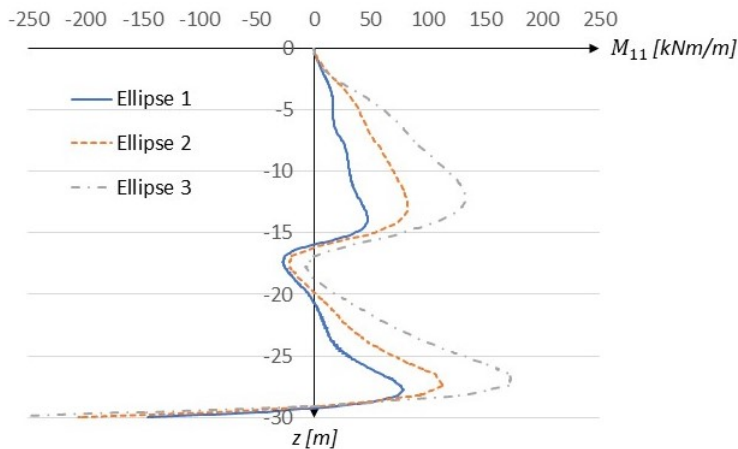
((a)) Vertical moment on long side.
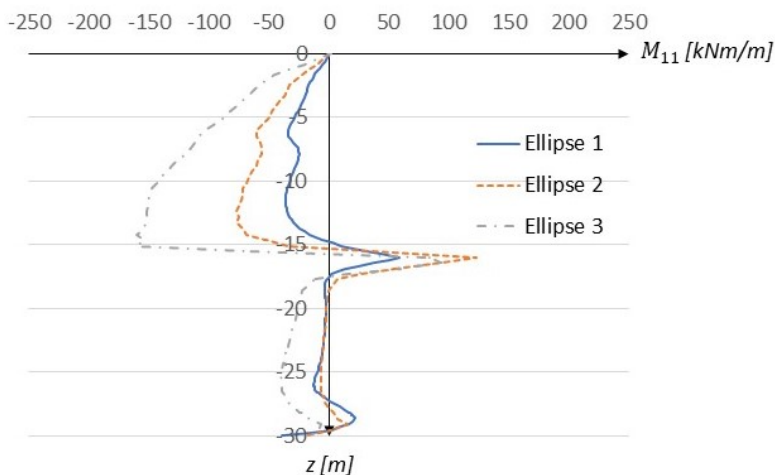
((b)) Vertical moment on short side.

Figure 9.30: Variation of vertical moment with depth on long and short side.

The obtained bending moment in the structure follow the theoretical results of Faustin et al. (2018), with the horizontal moment being the dominating moment. As expected, the moment increases when elongating the geometry. It can also be seen that the difference is bigger between Ellipse 2 and 3 than it is between Ellipse 1 and 2. This could possibly indicate that the elongation limit lies somewhere between the geometry of Ellipse 2 and 3. This assumption must be analysed more closely, but is backed-up by Ribeiro e Sousa et al. (2012) who mention that the practical ratio-limit between the minor and major axis of an elliptical shaft is somewhere around 0.5. Ellipse 3 having a relation of $A/B = 0.45$, could thereby be too elongated.

The torsional moment, M_{12}, is also obtained for each elliptic geometry. This load effect is however in general significantly lower than M_{11} and M_{22} and is therefore not plotted. Instead, the maximal and minimal obtained M_{12} in each ellipse is presented in Table 9.8.

Table 9.8: Maximum and minimum torsional moment, M_{12}, in each elliptical geometry.

Geometry	$M_{12,max}$ [kNm/m]	$M_{12,min}$ [kNm/m]
Ellipse 1	31.9	-31.9
Ellipse 2	70.1	-69.3
Ellipse 3	123.5	-119.9

9.4.3 Comparison of results and discussion

The models of the elliptical shapes in PLAXIS 3D are based on the verified model of the circular shape, the elliptical models are therefore considered reliable. The results from the simplified model in Robot are compared with the results obtained from the analysis in PLAXIS 3D to verify its accuracy. The variation of the hoop forces along the depth in the structure are compared in Figure 9.31 and the horizontal bending moments are compared in Figure 9.32.
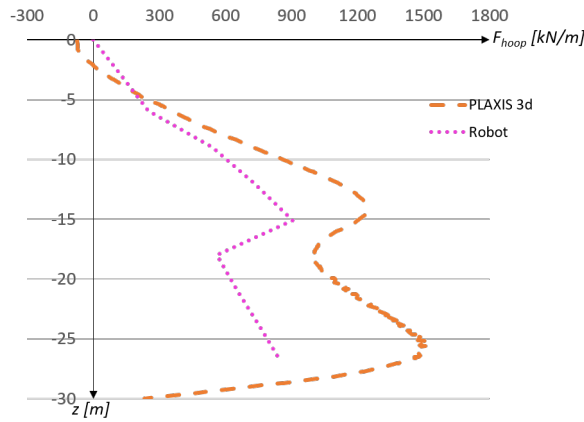
((a)) Hoop forces on long side.
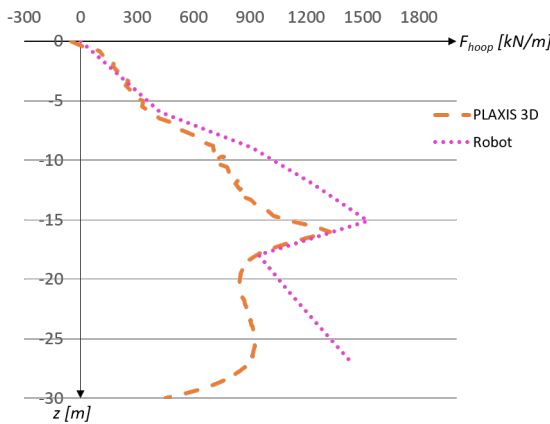
((b)) Hoop forces on short side.

Figure 9.31: Comparison of hoop forces in Ellipse 2, obtained from Robot and PLAXIS 3D.
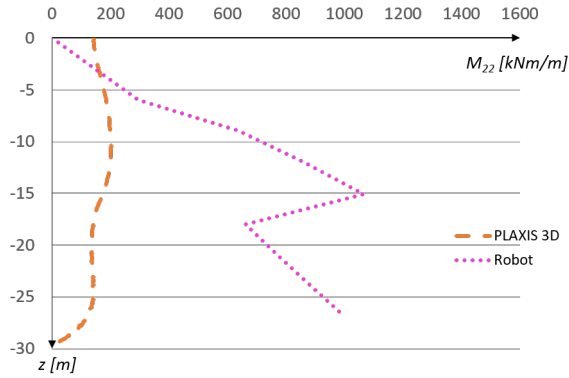
((a)) Horizontal bending moments on long side.
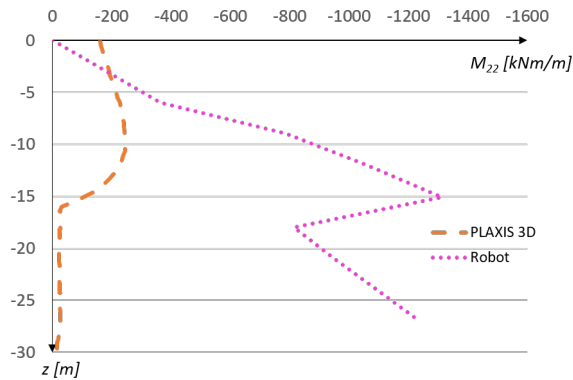
((b)) Horizontal bending moments on short side.

Figure 9.32: Comparison of horizontal bending moments in Ellipse 2, obtained from Robot and PLAXIS 3D.

The hoop forces from the two analyses are considered somewhat similar. However, the bending moments differ significantly. As pointed out in Section 9.4.2, the lateral pressure acting on the elliptical shapes change when the structure deforms. The lateral pressure acting on the deformed elliptic structure is not evenly distributed. The major difference of the two analyses is that the simplified model in Robot is unable to take into account how the lateral pressure varies with how the ellipse deforms, which is done in PLAXIS. This is probably the greatest reason for why the results in Robot differ from the results in PLAXIS 3D. The simplified analysis is also not able to include the contribution of load spreading over the height of the wall. This could also be a factor affecting the deviation of the results in Robot.

The conclusion of the comparison is that the simplified analysis in Robot exaggerates the bending moment in the retaining structure. Results more similar to PLAXIS 3D can presumably be achieved with Robot, but that would require a more detailed model. A detailed model contradicts the purpose with a simplified analysis and has therefore not been further investigated.

9.5 Optimal elliptical geometry

The structurally most optimal geometry for a shaft is the circular shape. However, constructing a shaft with an elliptical plan shape comes with other advantages. In order to define an optimised elliptical shape, one needs to define what 'optimised' is. In this case, the optimal shape is defined as the elliptical shape giving rise to structural load effects reaching the capacity of the retaining structure.

9.5.1 Capacity of retaining structure

The retaining structure consists of reinforced concrete diaphragm walls. Concrete is strong in carrying compression and the reinforcement has a high tensile capacity. The maximum capacity of the diaphragm wall is reached when either of the two materials capacity is fully utilised.

The lateral earth pressure from the soil causes bending moments and normal forces (hoop forces) in the retaining structure. The bending moment will inflict the structure with both tensile and compression stresses, and the normal force will cause compression stresses. The capacity of the structure to resist the combination of these two load effects is therefore of interest to evaluate in order to predict if the structure will fail or not. The normal force is beneficial to a certain degree because it counteracts the tensile stresses inflicted by the bending moment, and can thus prevent tensile failure. But the normal force together with the bending moment also increases the total compression stresses and thereby increases the risk of compression failure. This is explained with Figure 9.33, showing separately the simplified stress distribution over the reinforced concrete cross-section from the bending moment and the normal force and then the combination.

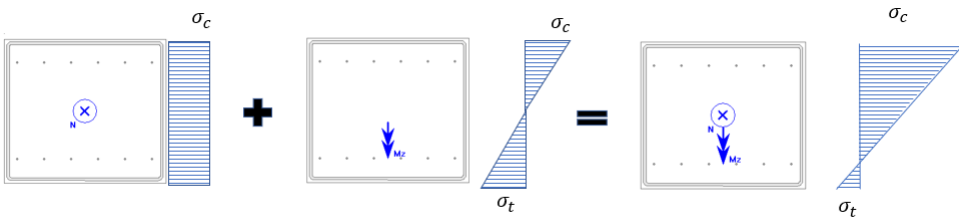Figure 9.33: Stress distribution over the cross-section

A simplified method of calculating the capacity of the diaphragm wall is used. The capacity for the diaphragm wall can be estimated by calculating the capacity for two fictitious beams. One beam represents a cutout of the diaphragm wall in the horizontal direction and the other a cutout in the vertical direction, illustrated in Figure 9.34.
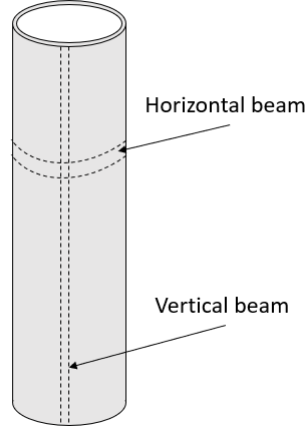
Figure 9.34: Cutout of fictitious beams.

The cross-section of the two fictitious beams are shown in Figure 9.35 which are based on the geometry of the diaphragm walls shown in Figure 7.3. The material parameters for the two fictitious beams are shown in Table 7.2. Normally, the horizontal reinforcement is not continuous over the panels in a diaphragm wall. In this example however, it is assumed, as a simplification, that the reinforcement is continuous in both directions. The cross-sections of the fictitious beams are depicted in Figure 9.35.

((a)) Cross-section of fictitious vertical beam.

((b)) Cross-section of fictitious horizontal beam.
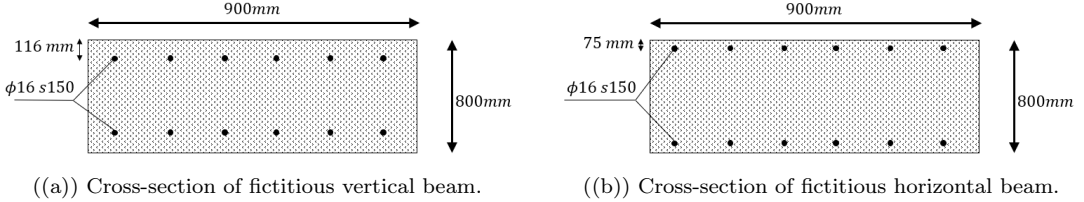
Figure 9.35: Cross-section of fictitious beams.

The bending moment capacity including the effect of the normal force is calculated for a doubly reinforced concrete beam according to Eurocode SS-EN 1992-1-1.

$$\text{Equilibrium of forces: } F_s = F_c + F'_s - F_N = A_s\sigma_s = f_{cm}0.8xb + A'_s\sigma'_s - F_N \tag{9.5}$$

$$\text{Moment equilibrium around } A_s\colon M_R = f_{cm}0.8xb(d - 0.4x) + A'_s\sigma'_s(d - d') \tag{9.6}$$

The location of the neutral layer x can be extracted from the equilibrium of forces for any normal force by assuming that the reinforcement at the upper edge or lower edge yields. The location of x is dependent on the magnitude of the normal force and the value of x will affect the moment capacity. The capacity for pure normal force N_R is

$$N_R = f_{cm}A_c \tag{9.7}$$

The capacity for the diaphragm wall to resist the vertical bending moment, M_{11}, is estimated by calculating the bending moment capacity of the fictitious vertical beam. There is no normal force

in the vertical direction and the self-weight of the wall is neglected. Based on Figure 9.35(a) and the material parameters given in Table 7.2, the capacity for vertical bending moment is calculated with Equation (9.5) and (9.6) to

$$M_{R,V} = 552 \quad \text{kNm/m} \tag{9.8}$$

The capacity for the diaphragm wall to resist the combination of normal force, F_{hoop}, and horizontal bending moment, M_{22}, can be obtained by plotting normal force and corresponding bending moment capacities for the fictitious horizontal beam shown in 9.35(b). This type of diagram is called an interaction diagram. The interaction diagram for the fictitious horizontal beam is plotted with a computer software and is presented in Figure 9.36.
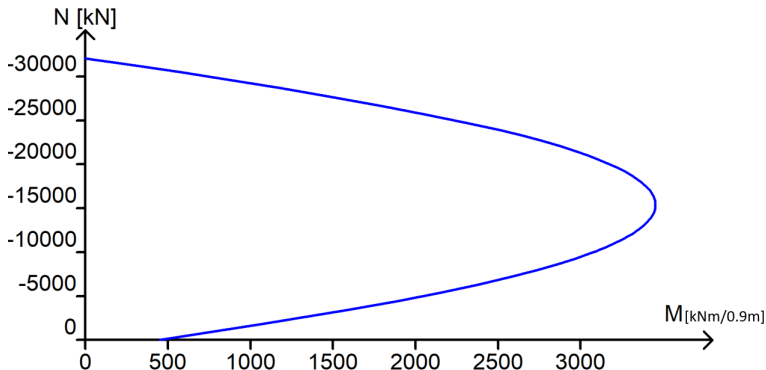
Figure 9.36: Interaction diagram for fictitious horizontal beam.

The capacity for pure bending moment is shown in the diagram where $N = 0$. In the same way, the capacity for pure normal force is shown where $M = 0$.

9.5.2 Geometry corresponding with capacity and conclusions

The highest obtained load effects from PLAXIS, in each elliptical geometry in the parameter study, are presented in Table 9.9. As the wall cross-section is symmetrically doubly reinforced in both directions, it will not matter if the moments are negative or positive. Every load effect is therefore presented as positive in this section. When determining the total acting moment in plates, the corresponding torsional moment M_{12} is added to M_{11} and M_{22} respectively.

Table 9.9: Maximal load effects in each elliptical geometry from parametric study. For $M_{22,max}$ the corresponding F_{hoop} is presented and for $F_{hoop,max}$ the corresponding M_{22} is presented. Also the corresponding M_{12} for all load effects is presented.

Load effect	Ellipse 1	Ellipse 2	Ellipse 3
$M_{11,max}$ [kNm/m]	161.2	231.8	340.0
M_{12} [kNm/m]	1.8	1.0	28.2
$M_{22,max}$ [kNm/m]	114.7	245.4	602.7
M_{12} [kNm/m]	0.1	0.9	1.0
F_{hoop} [kN/m]	796.9	870.6	685.9
$F_{hoop,max}$ [kN/m]	1438.8	1590.8	1945.0
M_{22} [kNm/m]	47.4	158.3	275.2
M_{12} [kNm/m]	0.2	67.4	48.6

By comparing the combination of maximal vertical bending moment M_{11} and corresponding torsional moment M_{12} from Table 9.9 with the bending moment capacity for vertical bending moment given in Equation (9.8), it turns out that the capacity in the vertical direction is sufficient for all three geometries. The maximal horizontal moments M_{22} together with the corresponding torsional moment M_{12} and hoop force F_{hoop} for each geometry is plotted in the interaction diagram shown in Figure 9.37.
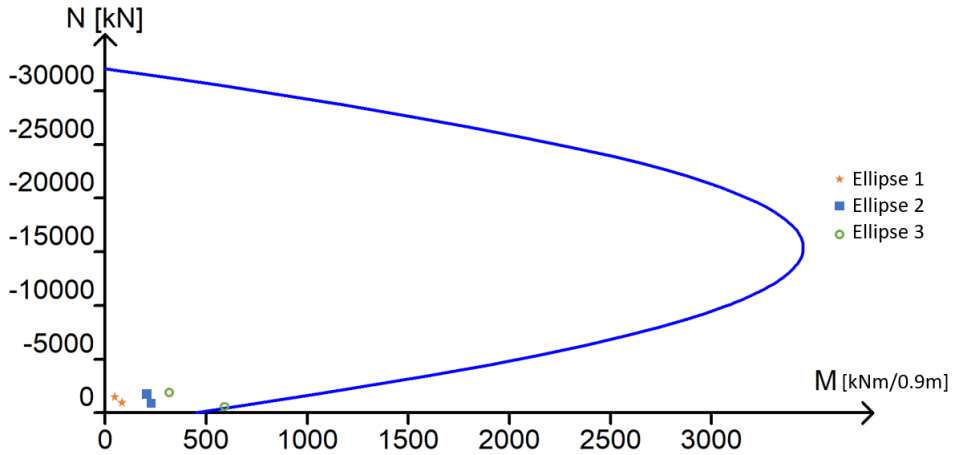
Figure 9.37: Interaction diagram for fictitious horizontal beam. The maximum combinations of load effects in each geometry is also inserted in the diagram.

As can be seen, all load combinations are located in the lower left corner in the interaction diagram. The interaction diagram shows that the wall can carry very high normal forces, and with sufficiently high normal forces also the horizontal bending moment capacity is really high. When inserting the load combination with $M_{22,max}$ for Ellipse 3, the point actually intersects the line of the diagram. This means that this combination is right on the limit of the capacity.

From these results, it is concluded that Ellipse 3 represents the most optimised geometry of an elliptical shaft, given the prescribed conditions such as geology and excavation size. The geometry represents an axial relation of $A/B = 0.45$, which lies in the margin of the expected result according to Ribeiro e Sousa et al. (2012). However, as the load combination is located on the interaction line, it would be reasonable to increase diameter A at least a little, in order to achieve a larger safety margin. It should also be noticed that this estimation of the wall capacity is highly preliminary. Conducting a more detailed analysis of the structure would provide a more accurate estimation of the optimal geometry, and doing so could possibly show that the geometry can be even more elongated as well as it could show that the geometry should be less elongated.

10 Discussion and conclusions

In this chapter, the results obtained from the analyses regarding the design example and their reliability are discussed. Conclusions are presented based on the discussion.

10.1 Groundwater analysis

The interaction between the groundwater and the structure has been analysed based on different scenarios, the best scenario and worst scenario regarding the hydraulic conductivities. Two models with different boundary conditions have been created representing the winter season and the summer season. The results show that the seepage into the shaft is almost the same when comparing the two models, see Table 8.3. The analyses of the two models show that when ascribing a recharge, the groundwater surface levels with the ground surface, as a result of the recharge being larger than the discharge. In the other model, the groundwater surface is obtained as shown in Figure 8.2. As described in Chapter 5, the rate of the groundwater flow is governed by the hydraulic head, which is the only deviating factor between the two models. This is probably the reason for why the groundwater seepage into the shaft is a little larger for the shaft with the groundwater level in line with the ground surface.

The effect of increasing the foundation depth of the retaining structure had the expected effect of increasing the flow path of the water, which in turn lowers the flow rate into the shaft. This is consistent with the theory presented in Chapter 5. Since there is an uncertainty about the hydraulic conductivities, the minimum required foundation depth of the retaining structure, that fulfills the specified demands mentioned in Chapter 5, is complicated to identify. Instead, the efficiency of increasing the foundation depth in order to lower the seepage could be evaluated and used as a factor indicating the optimal depth. From Table 8.3 it can be concluded that the seepage is lowered with 16 % when the foundation depth is increased from 7.5 m to 10 m. When increasing the foundation depth from 10 m to 12.5 m, the seepage is lowered with only 11 %. The effect of increasing the foundation depth must thereby be weighed against the effect on the seepage and the increasing construction costs.

10.2 Soil-structure interaction

In this thesis, the soil-structure interaction has been analysed with the FE-software PLAXIS. A simplified analysis has also been performed in order to only analyse the reaction of the structure when uniform hydrostatic loads are applied. When comparing the results from the two analyses it is noted that the results from the soil-structure interaction analysis is favourable for the structure. Taking the interaction between the structure and the soil into account when designing the shaft reduces the bending moments significantly which has proven to be crucial for the design.

The soil-structure interaction for a circular shaft has been verified against analytical calculations in the design example. The verified model have thereafter been used to obtain the optimised elongated shape of the shaft. With this in mind, it can be stated that the FE-model has been verified and should thereby be able to give reasonable results regarding the elliptical shaft. The results from the soil-structure interaction analysis show that the pressure on the elliptical structure is not uniformly distributed. The pressure is higher on the short sides of the ellipse in comparison to the pressure on the long sides. This could be explained with the soil's ability to develop active and passive pressure. The deformation of the ellipse in relation to the soil gives rise to the development of active pressure at the long side and passive pressure on the short

sides of the ellipse. As described in Section 4.5.1, the development of active and passive pressure stabilises the structure. This stabilising effect is probably one of the reasons why the bending moments are lower in the soil-structure interaction analysis than in the simplified structure analysis in Robot. Why the bending moments are remarkably lower for the soil-structure analysis could also be explained with the concept of an arch. The behaviour of the ellipse is similar to the behaviour of an arch, as described in Section 4.5.1. An arch has the capacity to reduce the bending moment caused by the loading due to the horizontal reaction forces at the supports creating counteracting bending moments. The ability of the soil to develop passive pressure increases the resistance of the soil that acts as the horizontal reaction forces creating the counteracting bending moments. A conclusion is that the results obtained from the soil-structure interaction analysis agree with what is written in the literature. The analysis is therefore assumed to be capable of sufficiently simulating the real behaviour of the interaction between the soil and the structure. The analysis is consequently considered a good method for identifying the optimal elongated shape of the shaft, which is the purpose with this thesis. The reliability of the analysis could be completely assured by comparing the results with experimental measurements of the specific design example. This has not been done since no experimental measurements have been performed.

When designing a structure it is important to identify the worst loading conditions of the structure. There is always a risk when simulating the real behavior of missing out the worst case scenario. There are regulations from different national and European institutes regarding the design method for this type of structures. The purpose with the regulations is to achieve a safety margin against failure in the final design. These regulations have not been looked into and followed in this thesis. However, the rules according to the regulations could maybe be implemented in the soil-structure interaction analysis and the analysis could thereby be used to obtain the final design of the structure. The material parameters and the results from the soil-structure interaction could be changed to design values by multiplying with partial and safety factors to obtain safety margins. The optimal elongated shape would consequently be less elongated. Despite the use of design values, the analysis must be weighed against the fact that there could be a worse scenario. In theory, the worst scenario would be when the at-rest pressure is present in the soil and the soil-structure interaction is neglected. The software, PLAXIS, used to perform the soil-structure interaction analysis does not provide the possibility to manually change the loading conditions and apply the worst case conditions for the structure. The software is not able to evaluate the second-order effects which could be crucial for a structure subjected to normal compression and bending moments. With this in mind, this specific software may not be the best to estimate the final design of the structure from a pure design perspective.

The results from the simplified analysis in Robot are compared to the soil-structure interaction analysis to verify its utility. The simplified structure analysis does not include the interaction between the structure and the soil. This means that the applied load remains unchanged and thereby resulting in high bending moments in the structure. This analysis is therefore considered to not be able to simulate the real behaviour of the structure and thereby lacks the possibility to identify the optimal elongated shape. The analysis could however still be used for design purposes. It could be used to analyse the reaction of the structure and to identify the optimal elongated shape for the worst case scenario, meaning the soil does not help to stabilise the structure. Robot also provides the possibility to calculate the second-order effects which could be crucial for the final design.

The optimal elongated shape of the shaft differs if the shape is optimised from a pure design

perspective compared to if the shape is optimised from analysing the real soil-structure interaction. With this thesis, the optimal elongated shape of the shaft have been sought for when the real soil-structure interaction is analysed.

10.2.1 Material model

Mohr-Coulomb's material model was chosen for the analysis of the soil-structure interaction. Based on the benefits, described in Section 6.1.2, this model is deemed to be suitable to model the stresses and failure in the soil regarding the design example. The model has its limitations when simulating deformations in the soil, which probably could effect the performed analyses. The margin of error obtained by using the MC-model could be investigated by performing numerical calculations with a more sophisticated material model. However, a more sophisticated material model requires more indata to the analysis which lowers the analysis's ability to represent a soil with general characteristics. The purpose with the thesis was to evaluate the optimal elongated shape of the shaft for a soil profile with general characteristics. The MC-model is therefore believed to be a suitable choice.

10.3 Optimal geometry of structure

As mentioned before, in Section 9.5, the optimal elliptical geometry is highly dependent on how 'optimal' is defined. In this design example, it was defined as the elliptical shape giving rise to structural load effects reaching the capacity of the retaining structure. Furthermore, the optimal shape needs to utilise the arching effect, leading to reduced bending moments. From this, it was found that the optimised elliptical geometry corresponds to a ratio $A/B = 0.45$, which is rather consistent with the theory presented in Section 4.5.1. However, this conclusion should be considered with care as the design example includes several predetermined assumptions and conditions. It should therefore be emphasised that the results in this project are only valid for the defined example. That said, the results can still be more generally used when it comes to understanding the behaviour of circular and elliptical shafts.

The design example uses a predetermined cross-section for the retaining wall. Having this predetermined cross-section, automatically induces some limitations on the geometry. If using a thicker and stronger cross-section, the shape could probably become more elongated and still be able to carry the resulting load effects, which would result in a different ratio A/B. The design example also gives a condition for the shaft of having a diameter B of $B = 11$ m. If instead having a requirement on the span being larger than 11 m, it would induce higher load effects in the structure. Subsequently, this could exceed the capacity of the predetermined cross-section of the wall. It is therefore not certain that the obtained optimal ratio of $A/B = 0.45$ would be valid if having a larger excavation. In this example, it turned out that the predetermined conditions actually gave a result which is rather consistent with theory, but that doesn't mean it is possible to construct a bigger shaft with the same ratio A/B and the same wall thickness. In order to construct a larger shaft with the same ratio A/B, it could require a proportional enlargement of the wall thickness. If instead having a predetermined diameter of $B = 22$ m, a linear proportional increase of the wall thickness would result in a 1.6 m thick wall. Whether such an increase of the wall thickness is reasonable or not will however have to be determined in each specific project. It is also not clear whether the shaft size and wall thickness will have a linear proportionality, this assumption is just used to exemplify. But it should be understood that every predetermined condition in this analysis brings uncertainties of how the results should be interpreted. As mentioned in Section 4.5.1, the structure could also be reinforced with ring

beams, which will entail a more slender cross-section of the wall itself. Having a larger shaft could thereby lead to a conclusion that instead of increasing the wall thickness, it is more appropriate to use ring beams. All of these things would however need to be studied in more detail.

In the design example, the walls are modelled as perfect circles and ellipses. This simplification could also be a factor of error in the calculations. Constructing a diaphragm wall entails having a non-uniform shape. Meaning there could arise stress concentrations in the joints, which would induce moments between the wall panels. If the exact shape of the retaining wall is taken into consideration, it would give rise to a different set of load effects as well as it would require a new evaluation of the wall capacity. However, it is in this project assumed that the line of thrust, presented in Section 4.2 and 4.4.1, could be located in the middle of the wall cross-section and thereby making it reasonable to simplify the structure as perfectly circular or elliptic.

10.4 Conclusions

The above discussions have highlighted some of the conclusions which can be drawn from this study. Below, the most important conclusions are listed in order to clarify the obtained results with regards to the objectives for this thesis.

- The soil-structure interaction is beneficial regarding the elliptical shaped shaft.

- The optimal ratio A/B for the elliptical shaft is found to be 0.45 regarding the design example.

- The zone of influence concerning the groundwater during dry season is found to be within the range of 500-1000 meter depending on the hydraulic conductivity of the soil.

- The groundwater seepage into the shaft decreases as the foundation depth of the retaining structure increases. However, the percentual decrease of groundwater seepage into the shaft, also decreases as the foundation depth increases.

11 Future work

This study had a set of predefined limitations, presented in Section 1.4. It could therefore be of interest to study the different effects which has not been included in this study. As this is linked to a tunnelling project, it could be of interest to study the impact of having openings in the shaft. This would result in a different composition of stresses in the structure, and could thereby give a different result on the optimal elliptical shape.

This thesis has only focused on the long-term situation. It would thereby be of interest to study the different stages of construction. It would also be interesting to study if the behaviour of a bigger shaft follows the same trend as for this shaft.

The purpose with this thesis was to find the optimal shape of the ellipse when the real behaviour of the soil is analysed. The optimal elongated shape could be evaluated when the behaviour of the soil is analysed with design factors taken into account. The two optimal shapes could then be compared.

A more general optimal elongated shape of the shaft could be obtained by performing analyses with soil profiles with different compositions of soils with different mechanical parameters. The effect of scaling up the geometry of the shaft would also be interesting to investigate.

The material model for the soil in this thesis is Mohr-Coulomb's material model. This material model entails fast calculations as the stress-strain relation is linear elastic perfectly plastic. The accuracy of using Mohr-Coulomb's material model could be evaluated by performing analyses with more sophisticated material models including the real stress-strain behaviour of soil which is non-linear.

The soil-structure interaction in this thesis was analysed with the FE-software PLAXIS, which is not optimal when conducting a structural analysis. It would be interesting to investigate the possibility to perform an advanced structural analysis which also includes the soil-structure interaction. In that way, the second-order effects could be analysed.

Bibliography

Åhnberg, H. (2004). *Sekantpålar som stödkonstruktion - Litteraturstudie*. Report. Linköping: Statens Geotekniska Institut - SGI.

Alén, C., Lindvall, A., Johansson, M. and Norén, C. (2006). *Slitsmurar som permanenta konstruktioner*. Report 11603. Svenska Byggbranschens Utvecklingsfond - SBUF.

Augarde, C. E. (2012). 'Linear failure criteria with three principal stresses'. In: *International Journal of Rock Mechanics Mining Sciences*, pp. 204–221.

Autodesk (28th May 2020). *Robot*. Version 2019. URL: https://www.autodesk.com/products/robot-structural-analysis.

Barnes, G. (2000). *SOIL MECHANICS: Principles and Practice*. London: MACMILLAN PRESS LTD.

Bentley Systems (28th May 2020). *PLAXIS*. Version 20.1. URL: https://www.plaxis.com/.

Block, P., Delong, M. and Ochsendorf, J. (2006). 'As Hangs the Flexible Line: Equilibrium of Masonry Arches'. In: *Nexus Network Journal* 8, pp. 13–24.

Buddemeier, R. W. (2000). *Water Table Drawdown and Well Pumping*. [Online]. Kansas Geological Survey. URL: http://www.kgs.ku.edu/HighPlains/atlas/apdrdwn.htm (visited on 10/05/2020).

Bujang, B. B. K. (2009). 'A Review of Basic Soil Constitutive Models for Geotechnical Application'. In: *Electronic Journal of Geotechnical Engineering* 14.

Chehadeh, A. S. (2014). 'Analysis and design of circular shafts using finite element method'. MA thesis. American University of Sharjah: College of Engineering.

Craig, R. F. and Knappett, J. A. (2012). *Craig's Soil Mechanics*. 8. CRC Press LLC.

Faustin, N. E., Elshafie, M. Z. E. B. and Mair, R. J. (2018). 'Modelling the excavation of elliptical shafts in the geotechnical centrifuge'. In: *Physical Modelling in Geotechnics*. Ed. by A. McNamara, S. Divall, R. Goodey, L. Taylor, S. Stallebrass and J. Panchal. Vol. 2. Proceeding of the 9th international conference on physical modelling in geotechnics. University of Cambridge. CRC Press, pp. 791–796.

Fetter, C. W. (2014). *Applied Hydrogeology.* 4th ed. Harlow: Pearson Education Limited. ISBN: 978-1-292-02290-1.

Fredriksson, A., Kullingsjö, A., Ryner, A. and Stille, H. (2018). *Sponthandboken.* Report 107. Pålkommissionen.

Freeze, R. A. and Cherry, J. A. (1979). *Groundwater.* Eaglewood Cliffs, New Jersey: Prentice-Hall. ISBN: 0-13-365312-9.

GEOSLOPE (28th May 2020). *SEEP/W.* Version 2019. URL: `https://www.geoslope.com/products/seep-w`.

Groundwater Engineering (2015). *Relief wells.* [Online]. URL: `https://www.groundwatereng.com/dewatering-techniques/relief-wells` (visited on 20/02/2020).

Jeong, S. S., Kim, K. Y. and Lim, H. S. (2014). 'Three-dimensional arching effect on vertical circular shafts'. In: *Geotechnical Aspects of Underground Construction in Soft Ground.* Korean Geotechnical Society, pp. 79–85.

Jumikis, A. R. (1962). *Soil mechanics.* Princeton, N.J.

Labuz, J. F. and Zang, A. (2012). 'Mohr–Coulomb Failure Criterion'. In: *Rock Mechanics and Rock Engineering* 45, pp. 975–979.

Lagioia, R. and Panteghini, A. (2015). 'On the existence of a unique class of yield and failure criteria comprising Tresca, von Mises, Drucker–Prager, Mohr–Coulomb, Galileo–Rankine, Matsuoka–Nakai and Lade–Duncan'. In: *Proc. R. Soc.* 472.

LTA (2004). *Installation of retaining wall - Diaphragm wall.* Brochure. Singapore: Land Transport Authority.

Mayne, G. W. and Kulhawy, H. F. (1982). 'K0–OCR relationships in soil'. In: *Journal of the Geotechnical Engineering Division* 108, pp. 851–872.

Michalowski, R. L. (2005). 'Coefficient of Earth Pressure at Restl'. In: *Journal of Geotechnical and Geoenvironmental Engineering* 230, pp. 1429–1433.

Paik, K. H. and Solgado, R. (2003). 'Estimation of active earth pressure against rigid retaining walls considering arching effects'. In: *Geotechnique* 53, pp. 643–653.

Pegah, E., Lui, H. and Dastanboo, N. (2017). 'Evaluation of the lateral earth pressure coefficients at-rest in granular soil deposits using the anisotropic components of S-wave velocity'. In: *Engineering Geology* 230, pp. 55–63.

Plaxis (n.d.[a]). *PLAXIS 2D Reference Manual.* CONNECT Edition V20. Bentley Systems International Limited. Dublin.

– (n.d.[b]). *PLAXIS 3D Reference Manual.* CONNECT Edition V20. Bentley Systems International Limited. Dublin.

Puller, M. (2003). *Deep Excavations: A practical manual.* 2nd ed. London: Thomas Telford Publishing. ISBN: 0-7277-3150-5.

Puzrin, A. M. (2012). *Constitutive Modelling in Geomechanics.* Berlin: Springer.

Rajagopal, K. (n.d.). *Controlled Yielding to Reduce Lateral Earth Pressures on Rigid Wall.* [University Lecture]. Madras: Indian Institute of Technology, Department of Civil Engineering.

Rajapakse, R. (2008). *Geotechnical Engineering Calculations and Rules of Thumb.* Butterworth-Heinemann. ISBN: 978-0-7506-8764-5.

Ribeiro e Sousa, L., Vargas, E., Fernandes, M. and Azevedo, R. (2012). *Innovative Numerical Modelling in Geomechanics.* London: CRC Press. ISBN: 978-0-415-61661-4.

Salomonsson, J. (2017a). *Malmö avloppstunnel - Utredningsfas 2.* PM Geo. Ramböll.

– (2017b). *Malmö avloppstunnel - Utredningsfas 2.* Markteknisk undersökningsrapport - MUR. Ramböll.

Skanska (2017). *Piled retaining walls.* [Online]. URL: `https://www.skanska.co.uk/expertise/construction/piling-and-foundations/foundation-techniques/piled-retaining-walls/` (visited on 31/01/2020).

Svenskt Trä (2016). *Limträhandbok - Del 2 Projektering av limträkonstruktioner.* Stockholm.

Terzaghi, K. (1944). *Theoretical soil mechanics.* 8. New York: Wiley.

Tobar, T. and Meguid, M. A. (2009). 'Comparative evaluation of methods to determine the earth pressure distribution on cylindrical shafts: A review'. In: *Tunnelling and Underground Space Technology* 25, pp. 188–197.

Verruijt, A. (2018). *An Introduction to Soil Mechanics.* 30. Springer International Publishing. ISBN: 978-3-319-61184-6.

Vidil, P. (2018). *Recommended junctions between diaphragm wall panels for deep excavations.* Report. Deep foundations institute.

Woodward, J. (2005). *An Introduction to Geotechnical Processes.* 2 Park Square, Milton Park, Abingdon: Spon Press. ISBN: 0-415-28646-8.